

Experimental and Computational Studies of the Effect of Lung Surfactant Protein-B Fragment, SP-B₁₋₉, on Model Lipid Bilayers

by

© Abinu Ajithan Jyothini

A thesis submitted to the School of Graduate Studies
in partial fulfilment of the requirements for the degree of
Master of Science

Department of Physics and Physical Oceanography
Memorial University of Newfoundland

November 2021

St. John's

Newfoundland

Abstract

The effect of lung surfactant protein fragment, SP-B₁₋₉, on a model lipid bilayer was investigated. Lung surfactants are lipid-protein complex mixtures that help in reducing the effort needed for breathing by lowering the surface tension that builds up at the alveolar air-liquid interface.

Recent research using deuterium NMR to examine the impact of SP-B fragments on bilayer model membranes found that the SP-B fragment, SP-B(1-25, 63-78), had a greater effect on the lipid chain acyl chain orientational order than the fragment, SP-B (8-25, 63-78). Both of these SP-B fragments include the first and last helices of SP-B, however they vary in the presence or absence of the insertion motif SP-B₁₋₇. This indicates that the insertion motif may contribute to the ability of SP-B to promote the bilayer reorganisation required for lung surfactant function. To gain a better understanding of the insertion motif's interaction with surfactant lipids, we used deuterium NMR and GROMACS molecular dynamic simulations to examine the effect of SP-B₁₋₉ on the acyl chain order of a lipid bilayer comprised of the lipids DPPC and POPG in a 7:3 ratio.

²H NMR studies with DPPC-*d*₆₂/POPG (7:3) and SP-B₁₋₉ at peptide-to-lipid ratios of 0.066 and 0.098 revealed no detectable effects in the first moment and order parameter profiles. Even after freezing and thawing the samples, no significant impact of the peptide was detected. On the other hand, MD simulations of lipid bilayers containing DPPC/POPG(7:3) and SP-B₁₋₉ at a peptide-to-lipid ratio of 0.031 showed a reduction in the acyl chain orientational order of the lipid chain. This difference between the simulation results and the experiments could be due to the aggregation of the peptides in the experiments. MD simulations also reveal the peptide's average orientation and conformation in the lipid bilayer. It

was found that the residues at peptide positions 5, 6, and 7 (Leucine, Proline, and Tyrosine, respectively) had the potential to be part of a helical segment with an average helicity of approximately 45%. The peptide seems to slope into the bilayer, with the last few residues at the N-terminal end remaining horizontal to the bilayer plain, not going closer to the bilayer centre.

Acknowledgements

I have received generous support, guidance, and assistance in completing this thesis. First and foremost, I would like to thank my supervisor, Dr. Michael Morrow, whose incredible expertise and experience aided in the formulation of the research question and the design of the methodology. I appreciate the tremendous patience he had supervising this thesis. I'd like to express my heartfelt gratitude to my co-supervisor, Dr. Ivan Saika-Voivod, for his insightful assistance in making the computational portion of this project exceptional. Likewise, I'm also thankful to Dr. Mohammad Hassan Khatami for his excellent skills and expertise in Molecular Dynamic Simulations, which were crucial at every stage of my simulations. I acknowledge the Natural Sciences and Engineering Research Council of Canada (NSERC) support, without which this project would not have been possible. I would also like to thank Dr. Valerie Booth for her valuable suggestions throughout the project as well as for providing support in peptide purification. In addition, I'd like to thank Drs. Anand Yethiraj, Todd Andrews, Stefan Wallin, and James Munroe for teaching the graduate courses. I'd like to thank my senior colleagues for their guidance and support. I would particularly like to thank Ms. Sarika Kumari for helping with purifying my peptide. Besides, I would like to thank Mr. Venketesh Thrithamara Ranganathan for acting as an energy booster throughout my course. Finally, I would like to thank my parents and my sister for their support and encouragement in my life.

Contents

Abstract	ii
Acknowledgements	iv
List of Tables	viii
List of Figures	ix
List of Abbreviations and Symbols	xiii
1 Introduction	1
1.1 Background	1
1.2 Surfactant Proteins	4
1.2.1 Lung Surfactant Protein B (SP-B)	7
1.3 Surfactant Lipids	9
1.3.1 Lipid Bilayer	11
1.4 Surfactant Dynamics	12
1.5 Objectives	14
2 Deuterium NMR Experiments	17

2.1	Theory	17
2.2	Spectral Shapes	21
2.3	First Moments	25
2.4	Order Parameter	26
2.5	Quadrupolar Echo and Echo Decay	30
2.6	Phase Behaviour of Binary Lipids	32
2.7	Materials and Methods	36
2.8	Results	38
2.8.1	Deuterium NMR Spectra	38
2.8.2	Deuterium NMR First Moments	42
2.8.3	Order Parameter Profile	43
2.8.4	Freeze-Thaw Cycling	47
3	Computer Simulations	50
3.1	CHARMM36 Force Field	53
3.2	Methods	55
3.2.1	System Setup	55
3.2.2	Extraction of Order Parameter Profiles Using Membrainy Software	62
3.2.3	Helicity Calculation	63
3.3	Results	64
3.3.1	Energy Time Series	64
3.3.2	Order Parameter Profile	65
3.3.3	Average Helicity of the Peptide	70
3.3.4	Average Orientation of the Peptide	75

3.3.4.1	Average Density Profile	75
3.3.4.2	Average Depth of Peptide Residues	76
4	Discussion	81
5	Conclusion	87
	Bibliography	89
A	System Setup	114
A.1	Making a PDB File From the Amino Acid Sequence of the Peptide.	114
A.1.1	Building Membrane-Lipid Bilayer System Using CHARMM GUI Membrane Builder	115
A.1.2	Energy Minimization, Energy Equilibration and Production Run . .	116
A.1.3	Running in the Clustor	119
B	Trajectory Analysis	121
B.1	Energy-Time Series	121
B.2	Order Parameter Profiles	121
B.3	Helicity Calculation	122
B.4	Density Profile	126
B.5	Depth Profile	126
B.6	Shortest Distance Calculation	128

List of Tables

2.1	Table showing the peak assignments of <i>sn</i> -1 and <i>sn</i> -2 chains of lipids based on the assignment method presented in Petrache et al.	28
3.1	Table showing the components of each simulation system and the peptide-to-lipid ratio of the two-peptide and multiple peptide systems.	56

List of Figures

1.1	Schematic diagram of an alveolus showing the location of phospholipids in lung surfactants at the alveolar air-fluid interface.	3
1.2	Typical composition of proteins and lipids in lung surfactant.	5
1.3	Amino-acid sequence of SP-B	7
1.4	Molecular structure of DPPC and POPG	10
1.5	Representation of a lipid bilayer	12
1.6	Role of SP-B and SP-C in surfactant dynamics during a respiratory compression expansion cycle	13
2.1	Quadrupolar interaction perturbs the Zeeman energy levels.	18
2.2	Orientation of applied magnetic field, bilayer normal and CD bond vector. .	21
2.3	^2H NMR quadrupolar doublet of lipid acyl chain deuterated at a single carbon position	22
2.4	The Pake doublet spectral shape.	23
2.5	Characteristic spectra of perdeuterated lipids	24
2.6	^2H NMR spectrum of chain perdeuterated sample DPPC- d_{62} /POPG(7:3) and corresponding dePaked spectrum	27
2.7	Order parameter profile vs carbon position for sample DPPC- d_{62} /POPG(7:3)	29

2.8	Quadrupolar echo pulse sequence and echo formation	31
2.9	Deuterium NMR spectra of DPPC- d_{62} (top) and the corresponding first moment plot (bottom). The transition from liquid crystalline to gel phase is observed as a discontinuous transition from 38 °C to 37 °C. The uncertainties in M_1 are comparable to the size of the symbol.	34
2.10	Deuterium NMR spectra of DPPC- d_{62} /POPG(7:3) (top) and the corresponding first moment plot (bottom).	35
2.11	^2H NMR spectra of (a) DPPC- d_{62} /POPG (b) DPPC- d_{62} /POPG plus SP- B_{1-9} with a peptide lipid ratio of 0.066 and (c) DPPC- d_{62} /POPG plus SP- B_{1-9} with a peptide lipid ratio of 0.098.	39
2.12	Quadrupolar echo amplitude decay for DPPC- d_{62} /POPG(7:3) samples made using $\text{CHCl}_3/\text{CH}_3\text{OH}$ (2:1) and HFIP solvents.	41
2.13	^2H NMR first moments as a function of temperature.	42
2.14	Depaked spectra of samples	44
2.15	Order parameter profiles	46
2.16	Order parameter comparison with freeze thaw experiment	48
3.1	Simulation systems after initial equilibration prior to production runs: (A) no peptide system and (B) two peptide system with a peptide to lipid ratio of 0.0038 at $T=310$ K.	58
3.2	Multiple peptide simulation system with 36 peptides having a peptide-to-lipid ratio of 0.031 after initial equilibration and prior to the production run: (A) side view and (B) top view at $T = 310$ K.	59

3.3	Simulation systems (A) no peptide system after 1050 ns, (B) two peptide system after 1150 ns and (C) multiple peptide system after 450 ns, all at $T= 323$ K.	61
3.4	Time evolution of potential energy of the no-peptide system (left), the two peptide system (middle) and the multiple-peptide system (right) at $T = 323$ K.	65
3.5	Order parameter comparison of No peptide (olive), Two peptide (chocolate) and Multiple peptide (blue) systems.	66
3.6	Comparison of simulation S_{CD} at 323 K (50 °C) with experimental S_{CD} at 319 K (46 °C) for DPPC for (top) a lipid-only sample and for the no-peptide simulation system and (bottom) and for the sample with SP-B ₁₋₉ having a peptide-to-lipid ratio of 0.066 and for the multiple peptide system with a peptide-to-lipid ratio of 0.031.	68
3.7	Time evolution of the potential energy for the multiple peptide system at $T=310$ K.	69
3.8	Comparison of order parameter profiles of DPPC of multiple-peptide system having a peptide-to-lipid ratio of 0.031 at 310 K (37 ° C) with experimental S_{CD} at 310 K (37 ° C) of sample with SP-B ₁₋₉ having a peptide-to-lipid ratio of 0.066. Panel A and B show the order parameter profile of <i>sn</i> -1 and <i>sn</i> -2 chains respectively.	70
3.9	Helicity of each residues of each peptide in the multiple peptide system averaged over 3750 time frames.	72
3.10	Time evolution of percentage helicity of the six residues of the peptide with helicity.	73

3.11	Helicity of each residues of each peptide in the multiple peptide system averaged over 36 peptides and each time frame. The time series shown in Figure 3.10 is averaged over each residue.	74
3.12	Average density profile of C_{α} of each residues of the peptide averaged over the 36 peptides in the multiple peptide simulation.	76
3.13	Average distance of C_{α} in the upper (open red circle) and lower (closed blue circle), center of mass of side chains of C_{α} in the upper (open magenta square) and lower (closed green square) leaflet and the average position of phosphorus atoms from the bilayer center.	77
3.14	Average shortest distance of C_{α} s peptide residues from a P atom in the lipid bilayer.	79
4.1	Overlap of dePaked spectra of the samples (Green) DPPC- d_{62} /POPG, (Red) DPPC- d_{62} /POPG + SP-B ₁₋₉ (P:L 0.066) and (Black) DPPC- d_{62} /POPG + SP-B ₁₋₉ (P:L 0.098).	83

List of Abbreviations and Symbols

SP-B	Surfactant Protein B
NMR	Nuclear Magnetic Resonance
DPPC	1,2-dipalmitoyl- <i>sn</i> -glycero-3-phosphocholine
DPPC- <i>d</i> ₆₂	1,2-dipalmitoyl- <i>d</i> ₆₂ - <i>sn</i> -glycero-3-phosphocholine
POPG	1-palmitoyl-2-oleoyl- <i>sn</i> -glycero-3-phospho-(1'-rac-glycerol) (sodium salt)
RDS	Respiratory Distress Syndrome
NRDS	Neonatal Respiratory Distress Syndrome
ARDS	Acute Respiratory Distress Syndrome
SP-A	Surfactant Protein A
SP-D	Surfactant Protein D
SP-C	Surfactant Protein C
PC	Phosphatidylcholine
PI	Phosphatidylinositol
PG	Phosphatidylglycerol
SS-NMR	Solid State Nuclear Magnetic Resonance
EFG	Electric Field Gradient
PAS	Principal Axis System

FID	Free Induction Decay
DSSP	Define Secondary Structure of Protein
STRIDE	STRuctural IDentification
$\Delta\nu_Q$	Quadrupolar splitting
CD	Carbon Deuterium
S_{CD}	Order Parameter
T_{2e}	Quadrupole Echo Decay Time

Chapter 1

Introduction

1.1 Background

The respiratory system is essential for all the body's functions. Its primary function is to provide oxygen to all parts of the body. Gaseous exchange occurs in the alveolar region of the lungs, where blood and air are brought very close together over a large surface area [1]. Lungs contain approximately 300-500 million alveoli, which provide more than 80-100 square meters of area for gaseous exchange [2].

When the lungs are filled with air during inhalation, there will be an interface between the air and the alveolar fluid. When water forms an interface with air, the water molecules tend to attract each other. As a result, the water surface always tries to contract. The same thing happens at the alveolar air-liquid interface. Here the fluid layer contracts and tends to push the air out of the alveoli. The net effect is an elastic contractile force at the air-water interface called surface tension elastic force [3]. This tends to cause the alveoli to collapse. However, natural surface-active agents under physiological conditions can

reduce the surface tension to near zero, facilitating the expansion of lungs and dramatically reducing the effort of breathing muscles in respiration [4]. Low surface tension at the alveolar air-liquid interface is necessary for normal breathing.

Lung surfactants are complex mixtures of proteins and lipids found at the air-liquid interface of the alveolus [5]. Type II epithelial cells (pneumocytes) lining the inner alveolar surface synthesize and secrete lung surfactant to the water layer at the inner surface of the alveolus [5]. The phospholipids in lung surfactants are amphipathic, meaning they have both hydrophobic and hydrophilic regions. As shown in **Figure 1.1**, hydrophilic head groups tend to align in contact with the aqueous layer, whereas hydrophobic acyl chains that do not favourably interact with water are exposed to the alveolar airspace. This counteracts the surface force at the alveolar air-liquid interface and reduces the surface tension to its minimum value (nearly 0 mN/m). This reduces the pressure required to keep the airspace open in the alveoli. The pressure exerted by surface tension can be expressed as the difference between pressures inside and outside the alveolus and is given by the Laplace equation,

$$\Delta P = P_{\text{int}} - P_{\text{ext}} = \frac{2\gamma}{r} \quad (1.1)$$

where ΔP is the difference between the pressures inside, P_{int} , and outside, P_{ext} , γ is the surface tension, and r is the radius of the alveolus [6]. This relationship demonstrates the inherent instability of the alveolar surface. If the surface tension remains constant, a decrease in alveolar radius during expiration raises pressure exerted by surface tension, causing the alveolus to shrink even more. Lung surfactants modify this situation and reduce surface tension in normal alveoli.

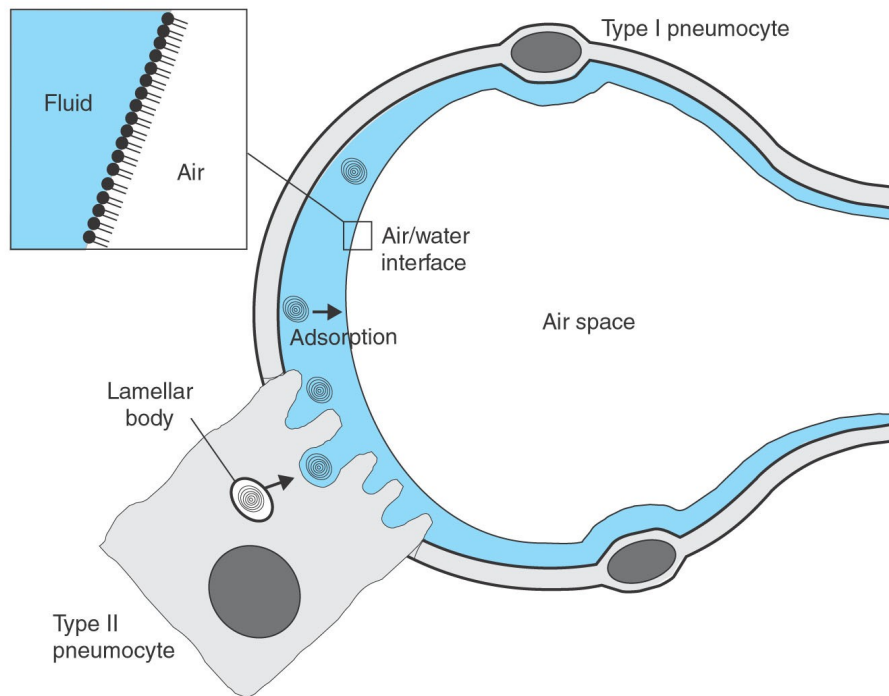


Figure 1.1 – Schematic diagram of an alveolus showing the location of phospholipids in lung surfactants at the alveolar air-fluid interface. The phospholipids align in such a way that the hydrophilic head groups are in contact with the fluid layer and the hydrophobic acyl chains are in contact with the air layer. *Reprinted from Publication Current Opinion in Structural Biology, Volume 12, Piknova, Barbora, Schram, Vincent, Hall, Stephen B, Pulmonary Surfactant: Phase Behavior and Function, Pages 487-494, Copyright (2002), with permission from Elsevier.*

An insufficient amount of lung surfactant or dysfunctional lung surfactant causes Respiratory Distress Syndrome (RDS). One example, Neonatal Respiratory Syndrome (NRDS) is primarily associated with premature babies born before the 37th week of gestation [7]. Premature babies have immature lungs that are incapable of producing enough surfactant materials. Surfactant replacement therapy has been shown to decrease the mortality rate of babies with severe NRDS [8]. The RDS that can affect adults is called Acute Respiratory Distress Syndrome (ARDS) and is caused by dysfunction of lung surfactants caused by

injury or illness [9]. Despite advances in critical care, the mortality rate in the case of severe ARDS remains very high [10]. A proper understanding of the mechanism of action of lung surfactant may contribute to the development of improved RDS treatments, possibly through the development of artificial surfactant therapies [11].

1.2 Surfactant Proteins

The surfactant layer in the lungs is composed of a mixture of phospholipids, some neutral lipids, and proteins. It consists of approximately 90% lipids and 10% proteins [12]. **Figure 1.2** illustrates the typical protein and lipid compositions of lung surfactants. Surfactant proteins are proteins that are closely associated with surfactant lipids and contribute to the establishment and maintenance of the surface active layer. So far, four surfactant proteins have been identified. They are SP-A, SP-B, SP-C and SP-D. SP-A and SP-D are large proteins with hydrophilic natures, while SP-B and SP-C are small proteins with hydrophobic natures [13].

Surfactant Protein A (SP-A) was the first surfactant protein to be discovered [14]. It has a molecular weight of 26-38 kDa in its monomeric form [15]. It is the most common surfactant protein accounting for about 5-6% of the total surfactant dry weight. SP-A belongs to the collectin family of proteins, meaning that it has Ca^{2+} -dependent lectins containing collagen-like domains in its structure [16]. SP-A is involved in surfactant function and homeostasis, including tubular myelin formation [17–19], enhancing the surfactant activity of SP-B [20,21], protecting the surfactant film from protein inhibition [22–24], and regulating the secretion and uptake of surfactant material by type II pneumocytes [25–27]. SP-A is also reported to be involved in host defense [28].

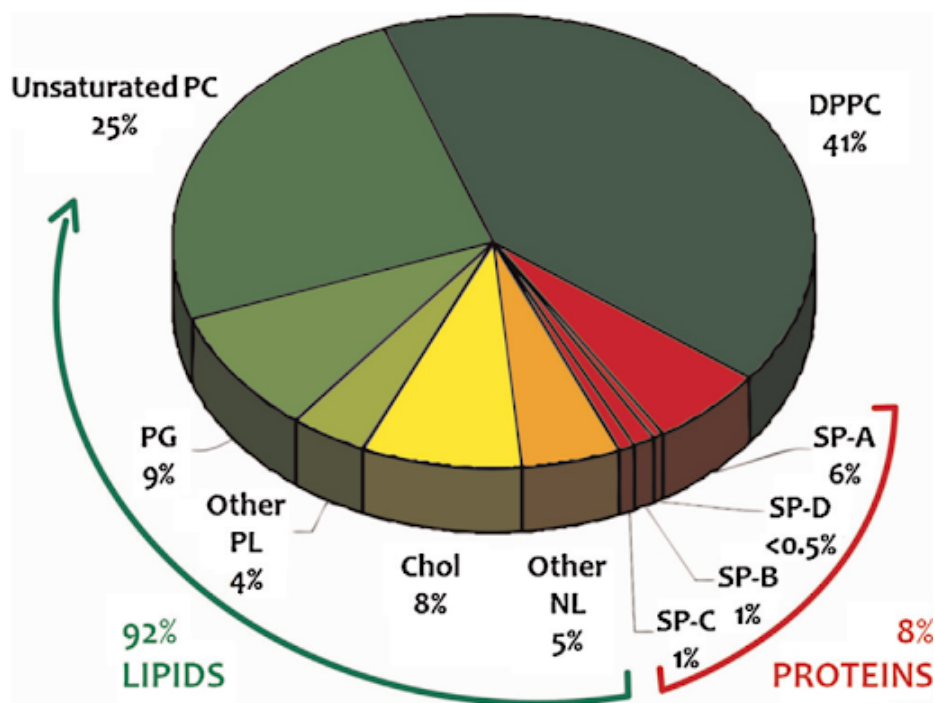


Figure 1.2 – Typical composition of protein and lipids in lung surfactant. The percentages shown here are with respect to the total mass. *Reprinted from Publication Chemistry and Physics of Lipids, Volume 185, Elisa Parra, Jesús Pérez-Gil, Composition, Structure and Mechanical Properties Define Performance of Pulmonary Surfactant Membranes and Films, Pages 153-175, Copyright (2015), with permission from Elsevier.*

Surfactant Protein D (SP-D) is also a collectin protein found in surfactants. It is involved in natural defense mechanisms in the lungs and in gut mucosa. SP-D molecules organize in trimers by the formation of triple helix collagenic segments and the coiled-coil like association of helical bundles. Two SP-D trimers combine to form one hexamer, and two of these hexamers combine to form an X-shaped dodecamer. This is the most common oligomer of SP-D found in airways [29]. SP-D is also involved in the regulation of surfactant homeostasis [16], which refers to any process responsible for maintaining a stable level of surface-active alveolar lipoprotein mixture.

SP-B is a hydrophobic protein with 79 amino-acid residues, and it forms a homodimer with a mass of ~ 17 kDa [30]. SP-B interacts with lipids due to its hydrophobic nature. Further details about SP-B are provided in the next section. Similar to SP-B, SP-C is also hydrophobic in nature. SP-C can be considered the only exclusively surfactant-associated protein as it seems to be present only in lung surfactants [31]. This 35 amino acid protein is formed from a 21 kDa pro-protein after the cleavage of the N-terminal and C-terminal precursor parts. SP-C takes on a very stable and regular α -helical conformation covering residues 10-35, which is the appropriate length for adopting a transmembrane orientation in phospholipid bilayer membranes rich in DPPC, as in lung surfactants [32]. If the length matches a bilayer, that is significant since that suggests that the helix must be predominantly in the lipid bilayer reservoir rather than the surface-active mono layer. In addition, it has two palmitoylated cysteines in the N-terminus, one on each side of the two proline residues [33]. This is one of the main factors contributing to the hydrophobicity of SP-C. Palmytoylation may be required to promote the structural transition of surfactant material from monolayer to bilayer [34] and to maintain protein association with densely packed surfactant films during exhalation [35]. Many of the functions of SP-C extend over to the functions of SP-B. SP-C is implicated in the adsorption of lipids from the bilayer reservoir to the air-liquid interface [36], respreading of the surfactant films during expansions [37], surfactant absorption by type II pneumocytes, and it also helps in stabilizing the lipid monolayer.

1.2.1 Lung Surfactant Protein B (SP-B)

The presence of SP-B in lung surfactant is necessary for transferring the surface active material from the surfactant reservoirs to the air-liquid interface for the formation of a stable surfactant layer, particularly during expiration [38]. Genetic deficiency of SP-B at birth can cause fatal respiratory failure [39,40]. It belongs to the saposin-like protein family (SAPLIP) [41]. The amino acid sequence of SP-B is shown in **Figure 1.3**.



Figure 1.3 – Amino-acid sequence of SP-B. Residues in red indicate the first nine N terminal amino acids, SP-B₁₋₉. The first seven amino acid sequence, SP-B₁₋₇, is thought to insert into the bilayer. The sulfide bridges formed by the cysteines are also shown in the figure.

SP-B is needed for the appropriate SP-C pro-protein processing [42], proper packing of surfactant membranes into lamellar bodies [43] and it is also involved in the unraveling process of the secreted surfactant materials into intermediate structures such as tubular myelins [17]. Once it reaches the interface, SP-B facilitates the adsorption of surfactant material to form interfacial films [44], reduces the surface tension value to a minimum by stabilizing the films during expiration [45], and it also promotes the respreading of the surfactant material during inspiration [46]. All these functions of SP-B depend on the

ability of SP-B to remodel membranes. SP-B is said to have lytic and fusogenic effects on phospholipid bilayers [47].

In the amino acid sequence of SP-B, 52% of amino acids are hydrophobic. It also contains one negatively charged residue and eight positively charged residues. Six out of seven cysteines in the SP-B sequence form three intramolecular disulfide bridges C8-C77, C11-C71 and C35-C46 [48] which stabilize the tertiary structure. Circular dichroism and infrared spectroscopy studies show that SP-B has a high helical content of approximately 40-50% [49–51]. Because of the highly hydrophobic nature of SP-B and the difficulty of producing recombinant SP-B, obtaining its three-dimensional structure is extremely difficult [30,52].

SP-B's interaction with lipid membranes involves electrostatic forces moderated by anionic phospholipid head groups and positively charged residues of the protein, as well as hydrophobic interaction of amphipathic SP-B helices with the acyl chains. The extent to which SP-B interacts with lipid membranes depends on the protein-lipid ratio and the method of reconstitution. One structural feature of SP-B is not found in other saposin super family proteins. The first seven N terminal tail amino acid sequence SP-B₁₋₇ often referred to as the “insertion sequence”, is thought to be inserted into the bilayer [53,53,54]. SP-B₁₋₇ (N terminal residues 1-7) likely plays a role in anchoring the protein to the lipid bilayers and monolayers in the surfactant structure. Hence, SP-B₁₋₇ is thought to be needed for the full surface tension reduction property of lung surfactants [47,55]. Proline amino acids at positions 2, 4, and 6 play an important role in the protein's ability to associate with membranes, most likely by adopting a specific conformation [54]. The ninth N terminal residue in SP-B is an aromatic residue, tryptophan. In fact, it is the only one tryptophan in the whole SP-B sequence. Aromatic side chains tend to bind to the inner regions of

the interface between the membrane acyl chain and the head groups [56]. The tryptophan at position 9 is thought to help in anchoring the SP-B on the phospholipid bilayer surface [57, 58]. In this study, we study the effect of SP-B₁₋₉ on lipid mixtures modeled on the lipid components of lung surfactant.

1.3 Surfactant Lipids

Pulmonary surfactants contain about 90% lipids, predominantly phospholipids. The zwitterionic lipid, phosphatidylcholine (PC) makes up about 60-70%, by mass, of the lipid. In mammalian lungs, anionic lipids such as phosphatidylinositol (PI) and phosphatidylglycerol (PG) account for approximately 8-15% of total surfactant mass [59]. Cholesterol accounts for up to 8 weight% or 15 mol% of the surfactant. In addition there are small amounts of fatty acids and triglycerides [13].

Dipalmitoylphosphatidylcholine (DPPC), a disaturated phospholipid, is the most abundant lipid species in lung surfactant, accounting for 41-70% of phosphatidylcholine [13]. DPPC can reduce the surface tension at the air-liquid interface on its own, but it adsorbs poorly and can collapse as it becomes rigid and brittle at low surface tension, resulting in poor surfactant film respreadability [60]. This limitation interferes with surfactant function because the monolayer must be respread and partially replaced after each breathing cycle. Unsaturated lipids such as POPG, on the other hand, can fluidize the layer sufficiently for rapid adsorption but cannot achieve low surface tension [61]. As a result, the lung surfactant typically contains a significant amount of unsaturated lipid, such as POPG, as well as saturated phospholipid, DPPC, for good spreadability and, as a result, low surface tension [54] after repeated cycling of lung volume. The molecular structures of DPPC and

POPG are shown in **Figure 1.4**.

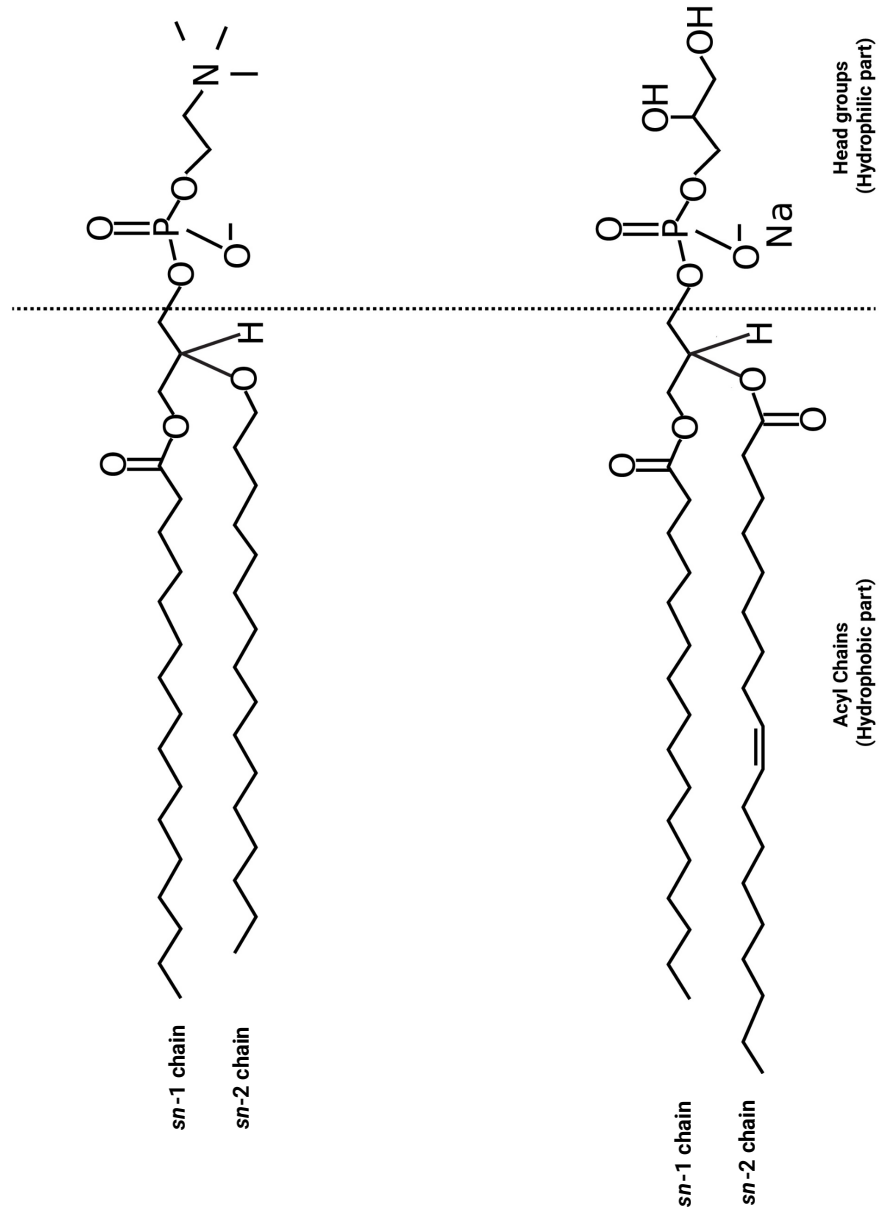


Figure 1.4 – Molecular structure of (A) 1,2-dipalmitoyl-*sn*-glycero-3-phosphocholine (DPPC) and (B) 1-palmitoyl-2-oleoyl-*sn*-glycero-3-phospho-(1'-*rac*-glycerol) (sodium salt) (POPG).

In phospholipid nomenclature, *sn* refers to “stereospecific numbering” and the *sn*-1 and *sn*-2 chains are the lipid acyl chains attached to the *sn*-1 and *sn*-2 carbons, respectively, of the lipid glycerol backbone.

1.3.1 Lipid Bilayer

Biological membranes having two layers of phospholipid molecules are called lipid bilayers. Phospholipids are amphiphilic in nature, meaning they have both hydrophobic and hydrophilic regions. The phosphate and choline moieties in the headgroup give the lipids polarity, while the acyl chains are nonpolar and hydrophobic. The lipid DPPC is zwitterionic in nature, meaning that it has charge separation but does not have a net charge. On the other hand, POPG is negatively charged, so that it is an anionic lipid. Choosing a combination of these two lipids provides a way to mimic the properties of lung surfactants. The **Figure 1.5** represents a bilayer composed of DPPC and POPG in the 7:3 ratio used for our molecular dynamic simulation studies discussed later.

Depending on the temperature, a lipid can be in a liquid crystalline phase (fluid) or gel phase (solid). The liquid crystalline phase is less ordered and hence more mobile compared to the gel phase where the bilayer is more ordered and less mobile [62]. When the temperature increases, the bilayer undergoes a transition from the gel phase to the liquid crystalline phase. The temperature at which this happens is called the chain melting temperature. This is characteristic of the lipid types in the bilayer.

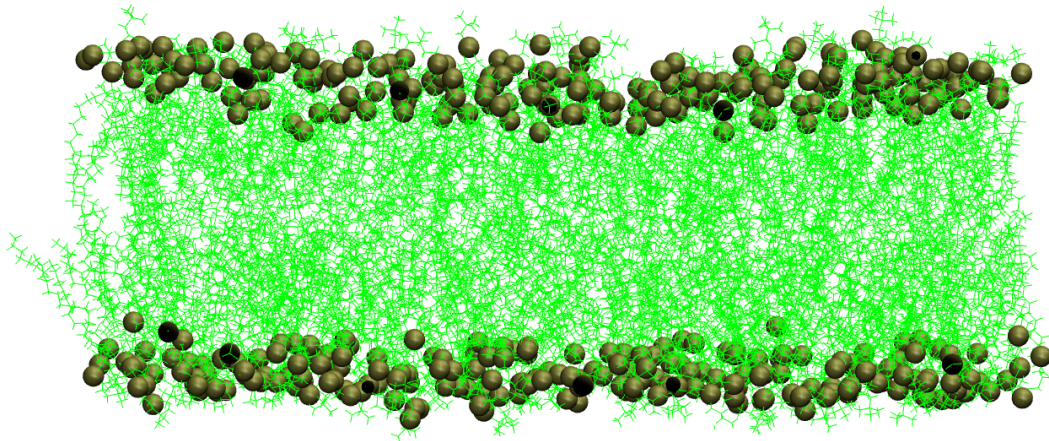


Figure 1.5 – Representation of a bilayer composed of lipids DPPC and POPG in a 7:3 ratio. The grey spheres at the top and bottom of the bilayer represents the phosphorus atoms of the lipid head groups on each layer. The green tails represent the lipid acyl chains.

1.4 Surfactant Dynamics

For maintaining a fully functional surfactant film at the alveolar air-fluid interface, the surfactant film needs to be refined continuously by efficiently removing any surfactant material that has been displaced from the surface active layer and incorporating freshly secreted surfactant materials. We still lack detailed understanding of the underlying processes involved in surfactant dynamics. Enrichment of surfactant films by DPPC is thought to be required to reduce surface tension to a minimum value during expiration. There are studies suggesting that the hydrophobic proteins SP-B and SP-C can selectively promote the insertion of DPPC into the interface [63]. During expiration, the compression of the surface film is thought to squeeze out unsaturated species from the interface, which results in the enrich-

ment of DPPC in the surfactant film [64–66]. The surfactant’s ability to form a multilayered film at the interface is also thought to be required for the surfactant to create very low surface tension [67–69]. The roles thought to be played by SP-B and SP-C in the transport of surfactants during a respiratory cycle are depicted in **Figure 1.6**. The surfactant film folds in response to lateral compression to form three-dimensional structures that can help to sustain maximal pressure. The steps illustrated are:

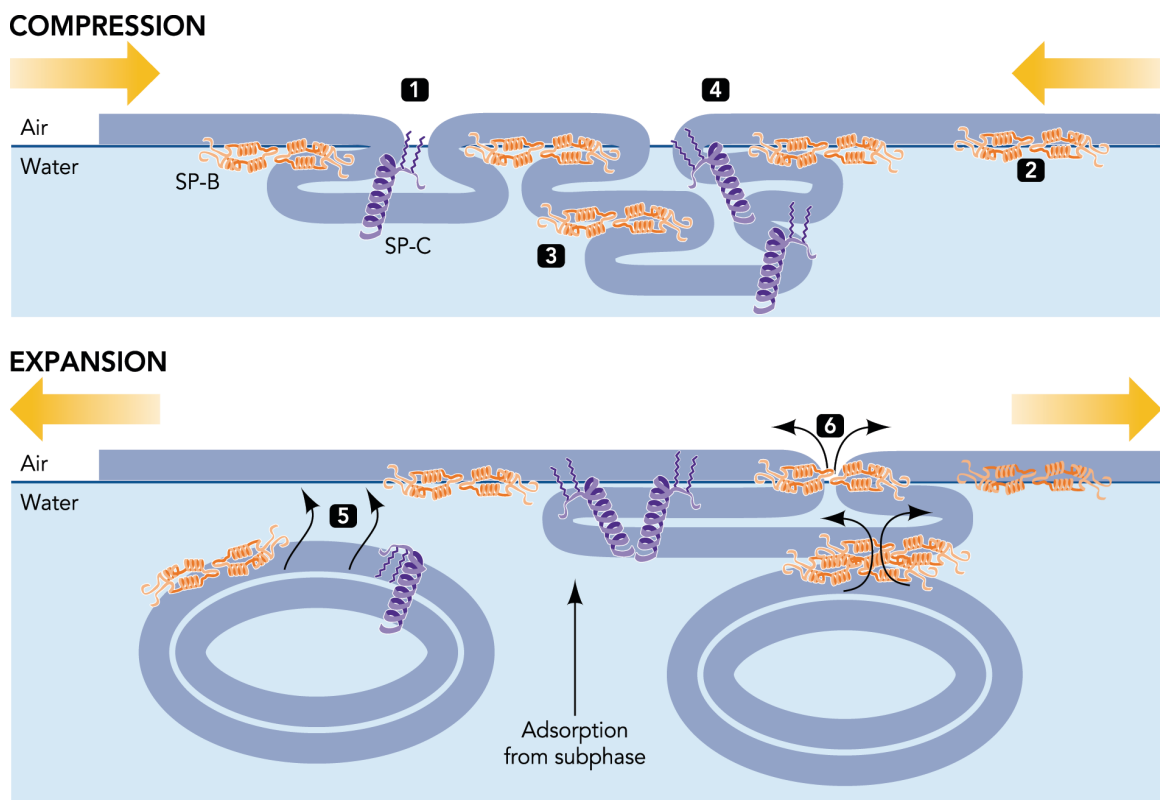


Figure 1.6 – The role played by SP-B and SP-C in the transport of surfactants during a respiratory cycle. Source: *Reprinted from Publication American Physiological Society, Volume 25, Perez-Gil, Jesús and Weaver, Timothy E, Pulmonary Surfactant Pathophysiology: Current Models and Open Questions, Pages 132-141, Copyright (2010), with permission from APS.*

1. During compression, SP-C promotes the folding of the surfactant films, removes some lipids and complex materials of lipids and proteins from the air-liquid interface [70] and makes 3D phases [4, 71, 72];
2. SP-B stabilizes the interfacial films;
3. SP-B facilitates the development of multilayered membrane structures [73] by promoting the formation of membrane-membrane contacts [47, 74, 75]. It also seems to give mechanical stability to the compressed films [76];
4. By inserting the protein's palmitoylated cysteines into the interfacial films and/or through the terminal NH₂, SP-C may promote the association of the surfactant structures that are excluded, with an interface that's compressed to the maximum. [72, 77];
5. and 6. Both SP-B and SP-C appear to initiate the insertion [78] and respreading [67] of the surface active material (phospholipids) from the surfactant reservoirs to the interface.

Surfactant function may thus require collaboration between these two hydrophobic surfactant proteins [79].

1.5 Objectives

The breathing process would be extremely difficult in the absence of a surfactant layer at the alveolar air-fluid interface due to surface tension [80]. The surfactant proteins and lipids discussed above collaborate to reduce the effort required for breathing by lowering surface tension. Two hydrophobic proteins, SP-B and SP-C are thought to facilitate the respreading

of fresh surfactant film at the interface by selectively promoting the insertion of DPPC [67]. A proper understanding of how the structural characteristics of specific surfactant proteins promote the recycling of surfactant material could facilitate the development of better synthetic materials for the treatment of respiratory disorders related to surfactant deficiency or dysfunction [81–83]. The conservation of SP-B during evolution indicates its necessity for lung surfactant function, and this was demonstrated by Melton et al. [84]. Since the insertion sequence is thought to insert into the bilayer, whether it has the ability to contribute to the functioning of SP-B would be beneficial to know for deciding whether to include the insertion sequence in the synthetic surfactants.

In a previous study of model bilayer membranes containing either the SP-B fragment SP-B (1-25, 63-78) or the fragment SP-B (8-25, 63-78), using deuterium NMR, it was found that the SP-B (1-25, 63-78) fragment had more effect on the lipid acyl chain orientational order than SP-B (8-25, 63-78) [85]. Both of these fragments contain the first and last helices of SP-B, but they differ in whether they have the insertion motif SP-B_{1–7} present or not. In a different study of SP-B_{1–25} [86] on model lipid bilayer, the peptide showed effects on lipids that are not observed for the SP-B fragments SP-B_{8–25} [87], SP-B_{59–80} [88] or SP-B_{63–78} [89]. There are other studies as well which show the functional importance of the insertion sequence [53, 54]. These studies suggest the possibility that the insertion motif might play a role in the ability of SP-B to promote the bilayer reorganization implicit in lung surfactant function.

The insertion sequence accounts for $\sim 9\%$ of the SP-B residues. In a previous ²H NMR study of natural SP-B at low concentrations in the bilayer, there was not much effect of SP-B on bilayer order or phase behavior, although there was an effect on slow motions [90]. The insertion sequence might have a stronger local effect on the bilayer that might be hard

to see in a study with full-length SP-B since the insertion sequence is a small fraction of the peptide mass present. If the peptide is inhomogeneously distributed in natural surfactant, then there could also be regions with a higher peptide-lipid ratio. In this study, we are looking at whether higher concentrations of the insertion sequence might contribute to bilayer perturbation.

In order to get a deeper understanding of the interaction of the insertion motif with the surfactant lipids, the current work examines the effect of the first nine N terminal residues of SP-B, SP-B₁₋₉, on the acyl chain order of model lipid bilayers composed of DPPC and POPG using deuterium NMR and GROMACS molecular dynamic simulations. Experimentally, we used deuterium NMR to study the effect of SP-B₁₋₉ at a relatively high peptide-lipid ratio, on DPPC chain order in DPPC-*d*₆₂/POPG (7:3) model lipid bilayers. Computationally, we used GROMACS to look at the peptide conformation, location, and its interaction with lipids at low and high peptide-to-lipid ratios. The extent to which a particular concentration of peptide perturbs the bilayer is studied by comparing systems at different peptide concentrations.

Chapter 2

Deuterium NMR Experiments

2.1 Theory

Nuclear Magnetic Resonance spectroscopy, abbreviated as NMR, is a spectroscopic technique which makes use of interactions that perturb the magnetic energies of specific nuclei to study the chemical, physical and biological aspects of matter. It is extensively used by researchers for the determination of the structure and function of macromolecules. Solid State Nuclear Magnetic Resonance or SS-NMR is used in situations where restricted molecular motion results in incomplete averaging of orientation-dependent interactions such as the quadrupole interaction. In SS-NMR, useful information about molecular dynamics is obtained from the residual perturbation left by such incomplete averaging. Wide line ^2H SS-NMR is a very useful technique for the characterization, in terms of dynamics and phase behaviour, of lipid bilayers containing ^2H labelled lipids.

Deuterium is a spin one nucleus. Nuclei with spin ≥ 1 have an electric quadrupolar moment. The deuterium nucleus has three energy levels, in an external magnetic field,

which correspond to the azimuthal quantum numbers $m = 1$, $m = 0$, and $m = -1$. Due to the non-spherical charge distribution of the nucleus with $\text{spin} \geq 1$, there is also an electrostatic interaction between the nuclear quadrupolar moment and the electric field gradient at the position of the nucleus. For a carbon-deuterium bond with a specific orientation with respect to an external magnetic field, the orientation-dependent electric quadrupolar moment perturbs the deuteron Zeeman energy levels. **Figure 2.1** depicts the deuteron Zeeman energy levels perturbed by this quadrupolar interaction.

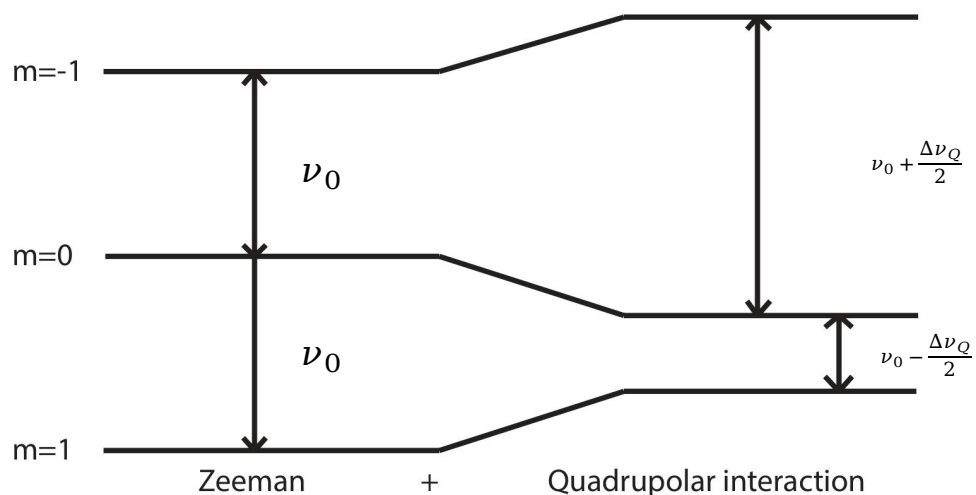


Figure 2.1 – Zeeman energy levels for a spin-1 nucleus in a magnetic field and their perturbation by the quadrupolar interaction. The magnitude of quadrupolar interaction relative to the Zeeman interaction is exaggerated. ν_0 is the Larmor frequency and $\Delta\nu_Q$ is the separation between the doublet peaks, called quadrupolar splitting.

Perturbation of Zeeman levels by the quadrupolar interaction results in a doublet spectrum in which the splitting reflects the bond orientation relative to the magnetic field di-

rection. Here the transition with frequency ν_0 splits into two transitions with frequencies $\nu_0 + \frac{\Delta\nu_Q}{2}$ and $\nu_0 - \frac{\Delta\nu_Q}{2}$ where ν_0 is the Larmor frequency and the separation between the doublet peaks ($\Delta\nu_Q$) is called the quadrupolar splitting .

For a carbon deuterium bond, the interaction of the nuclear electric quadrupolar moment, eQ , with the electric field gradient (EFG) at the nucleus can be written in Cartesian tensor notation [91]. Here e is the proton charge in the nucleus. The following treatments follow Davis 1983 [92]. Here the EFG can be diagonalized by transforming to the principal axis system (PAS), where principal axis refers to the electric field gradient tensor. Then the elements become,

$$V_{zz} = \frac{d^2V}{dz^2}, V_{yy} = \frac{d^2V}{dy^2}, V_{xx} = \frac{d^2V}{dx^2} \quad (2.1)$$

The principal axis component of EFG is $eq = V_{zz}$ and the asymmetry parameter is $\eta = V_{xx} - V_{yy}$. The EFG tensor can be transformed into the laboratory frame using Euler angles (α, β, γ) [93] which specify the orientation of the PAS of the EFG tensor with respect to the external magnetic field. Now the quadrupolar interaction Hamiltonian can be expressed as,

$$H_Q = \frac{e^2qQ}{4I(2I-1)} [3I_z^2 - I(I+1)] \left[\frac{1}{2} (3 \cos^2 \beta - 1) + \frac{1}{2} \eta \sin^2 \beta \cos 2\alpha \right]. \quad (2.2)$$

In the case of a deuteron, which has a spin-one nucleus ($I = 1$), in a carbon-deuterium bond which has an axial symmetry, $\eta = V_{xx} - V_{yy} = 0$, the above equation becomes,

$$H_Q = \frac{e^2qQ}{4} [3I_z^2 - 2] \left[\frac{1}{2} (3 \cos^2 \beta - 1) \right]. \quad (2.3)$$

The corresponding eigenvalues ($m = 0, \pm 1$) are,

$$E_m = \frac{e^2 q Q}{4} [3m^2 - 2] \left[\frac{1}{2} (3 \cos^2 \beta - 1) \right]. \quad (2.4)$$

In ^2H NMR experiments, the orientation-dependent quadrupolar interaction splits the deuteron Zeeman energy levels. The selection rule, $\Delta m = \pm 1$, then results in a doublet split by the quadrupolar splitting, $\Delta\nu_Q$, where

$$\Delta\nu_Q = \frac{3 e^2 q Q}{2 h} \left[\frac{1}{2} (3 \cos^2 \beta - 1) \right] = \frac{3 e^2 q Q}{4 h} (3 \cos^2 \beta - 1). \quad (2.5)$$

For carbon-deuterium (CD) bonds, the term $e^2 q Q/h = 167$ kHz [94]. This is called the quadrupolar coupling constant.

Equation 2.5 is for static CD bonds. In fluid phase lipid bilayers and biological membranes, the local bilayer normal is the axis of symmetry for molecular reorientation. This means that for lipid bilayers in the liquid crystalline state, the phospholipid molecules will undergo fast axially symmetric reorientation about the bilayer normal. The quadrupolar interaction for CD bonds attached to the lipids in such a bilayer is partially averaged by these motions and this reduces the quadrupolar splitting for a given CD bond. In this case it is better to transform from the PAS to a coordinate system fixed to the molecule. Doing so introduces another factor, $P_2(\cos \theta) = \frac{(3 \cos^2 \theta - 1)}{2}$ into the splitting. The angle β becomes the angle between the applied magnetic field and the axis of motional symmetry (now the bilayer normal) and θ is the angle between the CD bond and the bilayer normal. These angles are illustrated in **Figure 2.2**. The factor $P_2(\cos \theta)$ needs to be averaged if the angle θ is modulated by a molecule's conformational fluctuations on a timescale shorter than about 10^{-5} s. Now the quadrupolar splitting becomes,

$$\Delta\nu_Q = \frac{3}{4} \frac{e^2 q Q}{h} (3 \cos^2 \beta - 1) S_{CD} \quad (2.6)$$

where $S_{CD} = \langle \frac{1}{2}(3 \cos^2 \theta - 1) \rangle$ is the orientational order parameter of the chain segment containing the CD bond. The average in S_{CD} is over motions that occur on timescales shorter than the characteristic time ($\sim 10^{-5}$ s) for the experiment.

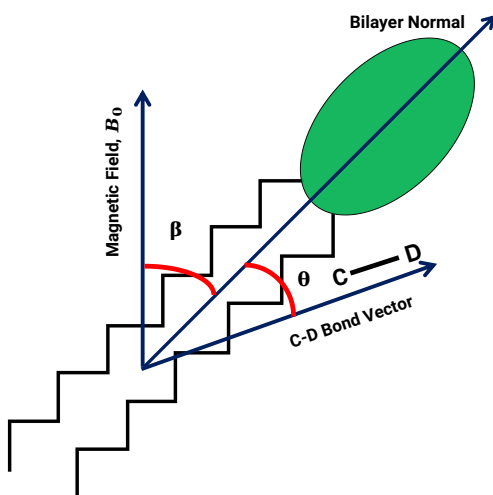


Figure 2.2 – Orientation of bilayer normal and CD bond vector with respect to the applied magnetic field. Here angle β is the angle between the applied magnetic field, B_0 and the bilayer normal. Angle θ is the angle between the CD bond vector and the bilayer normal.

2.2 Spectral Shapes

The maximum quadrupolar splitting occurs when there is no molecular reorientation with respect to the magnetic field. This is found when the CD bond is aligned parallel to the magnetic field ($\beta = 0^\circ$, in this case θ is effectively the angle between the magnetic field

and the CD bond). In the case of a fluid lipid bilayer, the quadrupolar splittings are significantly reduced due to molecular motions. The experimental value of quadrupolar splitting provides valuable information about the degree of molecular motion experienced by a given molecular segment. For oriented samples where the local bilayer normal has a single well-defined orientation with respect to the magnetic field (single value of β), we would observe a simple doublet with a quadrupolar splitting given by **Equation 2.6**. The doublet is shown in **Figure 2.3**

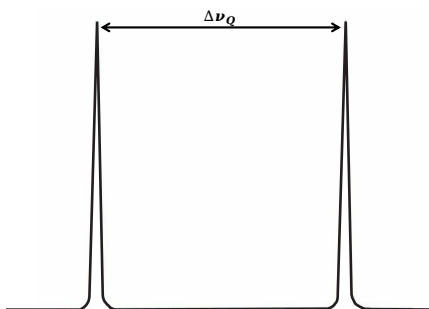


Figure 2.3 – ^2H NMR quadrupolar doublet for oriented lipid bilayers containing lipid acyl chains deuterated at a single carbon position.

For multilamellar vesicle samples, all local bilayer orientations are possible, and the distribution of β values corresponds to a spherical distribution of direction vectors. If the lipids in these vesicles are undergoing fast axially symmetric reorientation about the bilayer normal, the resulting spectrum is a weighted superposition of doublets from all orientations. This particular spectral shape is called a Pake doublet (or powder spectrum) and is shown in **Figure 2.4**. Here the quadrupolar splitting is defined as the separation between the two intense peaks corresponding to the sample regions where the bilayer normal is oriented

perpendicular ($\beta = 90^\circ$) to the magnetic field. This splitting is scaled by the orientational order parameter S_{CD} , for that specific segment.

Information about the entire lipid chain can be obtained from a single experiment by perdeuterating the lipid samples. In perdeuterated acyl chain samples, all the hydrogen atoms on the lipid acyl chains are replaced by deuterium atoms.

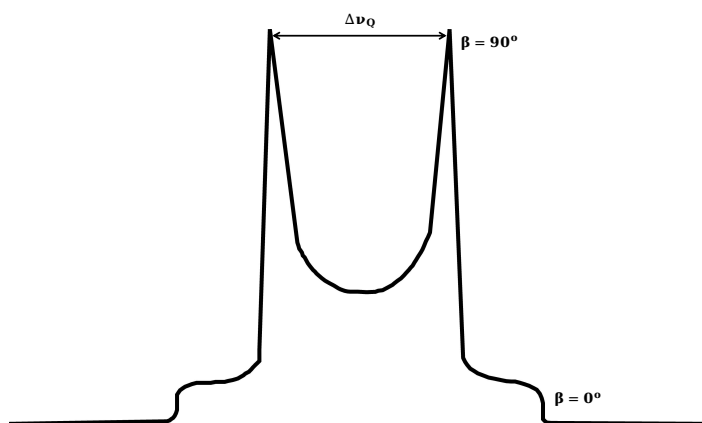


Figure 2.4 – The Pake doublet spectral shape. The spectrum is a superposition of doublets arising from all bilayer normal orientations with respect to the magnetic field.

For lipid chains that are labelled at all positions, the variation of the CD bond order with chain position results in the spectrum containing a superposition of quadrupolar splittings for all the deuterium atoms along the acyl chain as shown in **Figure 2.5**.

The quadrupolar interaction averages out more as the amplitudes of the chain motions increase, which reduces the splitting. The biggest quadrupolar splitting arises from the methylene groups (CD_2) towards the headgroup end of the acyl chain. The motional constraints of (CD_2) groups increase towards the headgroups, resulting in less motional averaging and, as a result, greater quadrupolar splitting. The methyl groups (CD_3) at the

acyl chain ends, which are the least motionally constrained and which undergo an additional fast rotation about the methyl axis, display the smallest quadrupolar splitting. The resulting spectrum reflects chain order that increases from the methyl groups (A, the two intense peaks in the middle) to the methylene groups closest to the headgroups (B, the larger quadrupolar splitting towards the edges).

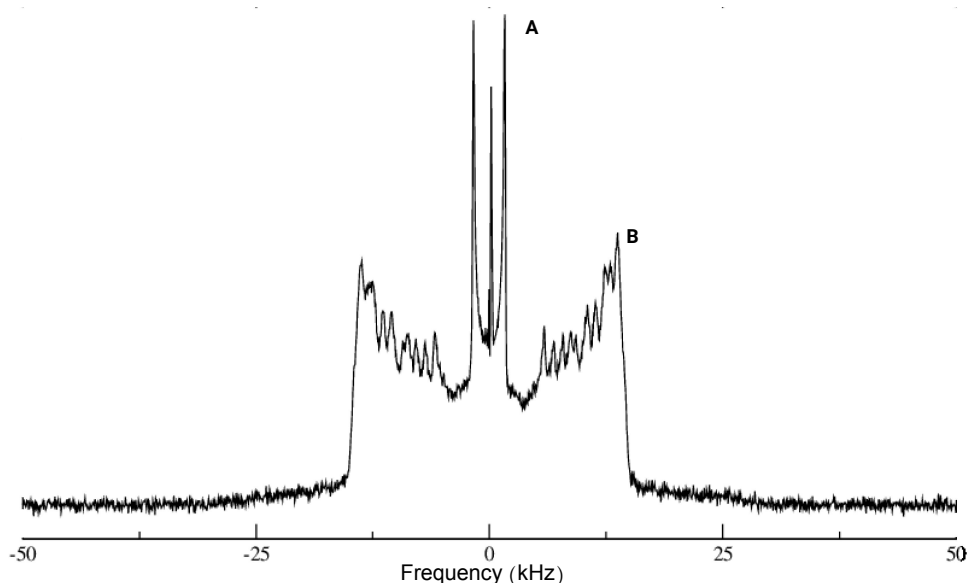


Figure 2.5 – ^2H NMR spectrum of a DPPC- d_{62} /POPG sample showing the characteristic spectrum for randomly oriented perdeuterated lipids. The spectrum is a superposition of spectral components with quadrupolar splittings from all the deuterium atoms along the acyl chain. (A) Smaller splitting arising from the methyl groups at the acyl chain end and (B) the larger quadrupolar splitting of the prominent spectral edge arising from the methylene groups near the acyl chain headgroup. The narrow single peak at the centre of the spectrum is from natural abundance deuterons in the buffer water.

2.3 First Moments

The first moment, M_1 , of the deuterium NMR spectrum lets us quantify, with a single number, the average chain orientational order for bilayers containing perdeuterated lipids [92]. M_1 can also be extended to the gel phase where we cannot resolve the individual splitting due to the overlapping of the quadrupolar splittings. Spectral moments can be useful for comparing chain orders at different temperatures and at different bilayer compositions. ^2H NMR spectral moments are calculated in terms of angular frequencies. For a ^2H NMR spectrum, the first moment is proportional to the average quadrupolar splitting. For a spectrum with line shape $S(\omega)$ (which is the spectral intensity at angular frequency ω), the n^{th} moment is given by [95],

$$M_n = \frac{\int_0^\infty \omega^n S(\omega) d(\omega)}{\int_0^\infty S(\omega) d(\omega)} \quad (2.7)$$

Here, the angular frequency ω is measured from the spectral center. The zeroth moment, M_0 is given by $\int_0^\infty S(\omega) d(\omega)$ which represents half of the area under the ^2H NMR spectrum. The first spectral moment, the average quadrupolar splitting, and the average orientational order are related by,

$$M_1 = \frac{4\pi}{3\sqrt{3}} \langle \Delta\nu_Q \rangle = \frac{\pi}{\sqrt{3}} \frac{e^2 q Q}{h} \langle S_{CD} \rangle. \quad (2.8)$$

Since the deuterium NMR first moment is directly proportional to $\langle S_{CD} \rangle$, it can provide useful information about phase transitions and orientational order.

2.4 Order Parameter

The orientational order parameter for each CD bond in each chain can be obtained from the corresponding quadrupolar splitting. The order parameter, S_{CD} , is mentioned in **Equation 2.6**. Deuterium nuclei at each carbon position of the lipid acyl chain have a distinct value of order parameter depending on the motions of the acyl chain segment. As a result, the spectrum is a superposition of spectra from all of these carbon positions, and assigning splittings from the powder spectra may be difficult. Assignment is simplified by using a technique called dePaking [96–98] to transform the powder spectrum into the spectrum that would be obtained if the sample were oriented. For this thesis, dePaking is done using a fast Fourier transform weighted to put the spectral intensity at the splittings corresponding to the 90° bilayer normal orientation [98]. An illustrative example of a dePaked ^2H NMR spectrum for a DPPC- d_{62} /POPG(7:3) sample is given in **Figure 2.6 B**.

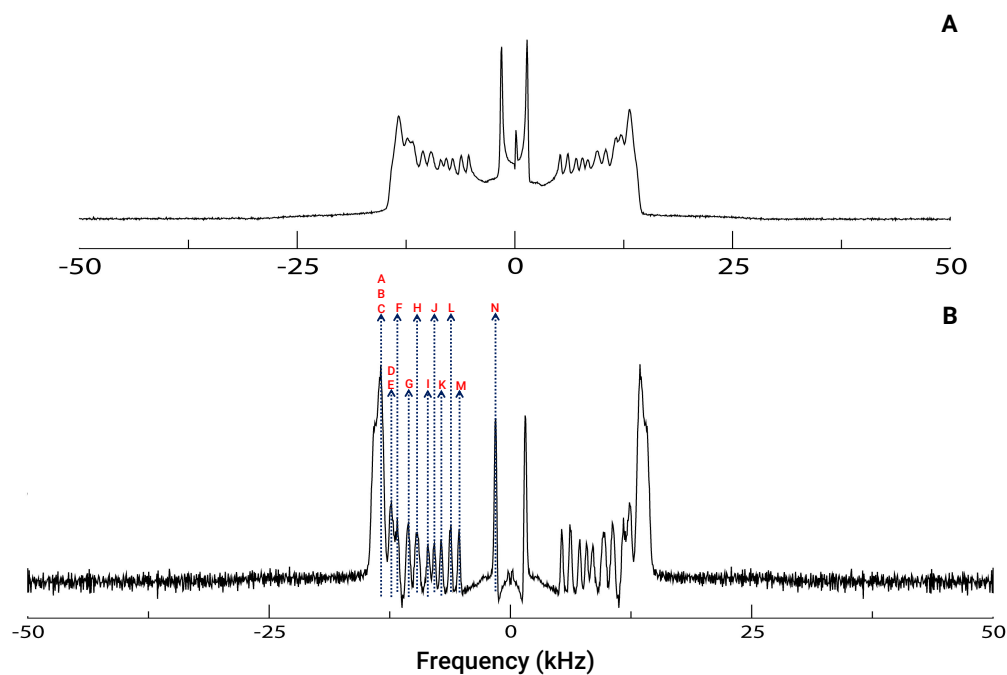


Figure 2.6 – Illustrative example of (A) ^2H NMR spectrum of chain perdeuterated DPPC- d_{62} /POPG(7:3) multilamellar vesicle at 40 °C and (B) corresponding dePaked spectrum and with spectral assignments. How these peak assignments are used for order parameter calculation is shown in **Table 2.1**.

The vertical lines with labeling correspond to each resolved peak in the dePaked spectrum. The assignment of peaks to *sn*-1 and *sn*-2 chains are given in **Table 2.1** based on the assignment methods presented in Petrache et al. [99]. The doublets associated with the unresolved peak are given the value of the splitting for the prominent peak having the greatest quadrupolar splitting. The portion of the order parameter profile coming from this spectral feature is called the plateau region [92] and is shown in **Figure 2.7**.

Table 2.1 – Table showing the peak assignments of *sn* – 1 and *sn* – 2 chains of lipids based on the assignment method presented in Petrache et al. [99]. Peak labelling is given in **Figure 2.6 B**.

Carbon Position	<i>sn</i>-1 Peak Assignment	<i>sn</i>-2 Peak Assignment
16	N	N
15	M	L
14	K	J
13	I	H
12	H	G
11	G	F
10	F	E
9	D	D
8	C	C
7	B	B
6	A	A
5	A	A
4	A	A
3	A	A
2	A	A

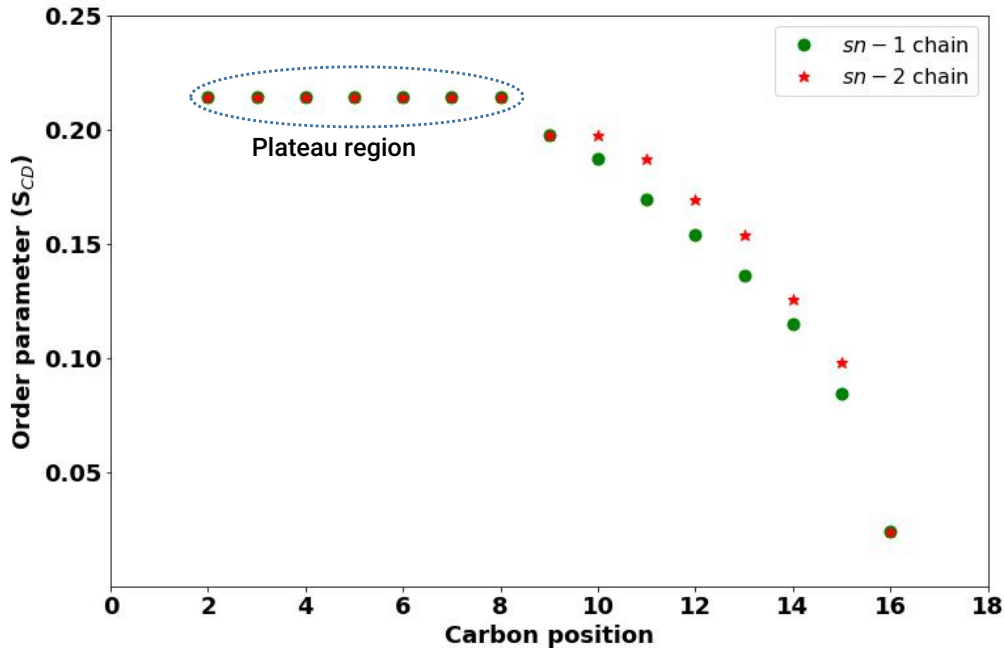


Figure 2.7 – Order parameter profile vs carbon position of *sn*-1 and *sn*-2 chains of a DPPC- d_{62} /POPG(7:3) sample at $T = 40\text{ }^{\circ}\text{C}$ showing the plateau region done according to the assignment scheme shown in **Table 2.1**.

As noted above, different regions of the lipid molecule undergo different degrees of reorientations. The degree of reorientation depends on the position of the CD bonds along the lipid acyl chain and hence the orientational order parameters vary depending on position along the chain. For lipid acyl chains, the methyl groups (CD_3) at the tail end of the chain are less motionally constrained compared to the methylene groups towards the head-group (CD_2). The more free segments are to move, the more the quadrupolar interaction is averaged, resulting in smaller quadrupolar splitting and, as a result, a smaller orientational order parameter value.

2.5 Quadrupolar Echo and Echo Decay

There is an instrumental issue with ^2H NMR experiments that needs to be addressed in order to be able to observe the spectra. A ^2H NMR spectrum spans a frequency range in the tens of kHz. In an RF (Radio Frequency) pulse, the range of frequencies contained is inversely proportional to its length. To excite spins over such frequency ranges, we need to use very short RF pulses, in the range of $\sim 5\text{-}10\ \mu\text{s}$, in order to rotate the full range of deuteron magnetization from the magnetic field direction to the plane perpendicular to that direction. Such pulses are called $\frac{\pi}{2}$ pulses. To get these very short $\frac{\pi}{2}$ pulses, the magnitude of radio frequency field (ω_1) needs to be very large, requiring the use of a pulse amplifier having an output power of $\sim 1\ \text{kW}$. The free induction decay will be short (because of the wide range of frequencies in the spectrum), of the order of $\sim 10\text{-}20\ \mu\text{s}$, and thus comparable to the recovery time of the preamplifier from the residual effects of the large RF pulse. This necessitates moving the period of signal acquisition away from the RF pulse. This can be done by using a quadrupolar echo pulse sequence [100]. It consists of two $\frac{\pi}{2}$ pulses with a phase difference of 90° and separated by a time interval, τ as shown in **Figure 2.8**.

In a static magnetic field, the magnetic moments of each nucleus in a sample interact with the magnetic field. The density of the magnetic moments in the sample is called magnetization. The average of the magnetization of all the spins in the sample is called net magnetization, M . M is aligned parallel to the magnetic field at thermal equilibrium. The net magnetization can be tipped to the transverse plane by a $\frac{\pi}{2}$ pulse. It will then precess around the applied magnetic field. The first $\frac{\pi}{2}$ pulse of the quadrupolar echo sequence tips the net magnetization of the sample from the z axis to the xy plane and generates transverse magnetization. After this first $\frac{\pi}{2}$ pulse, the spins evolve under the influence of the

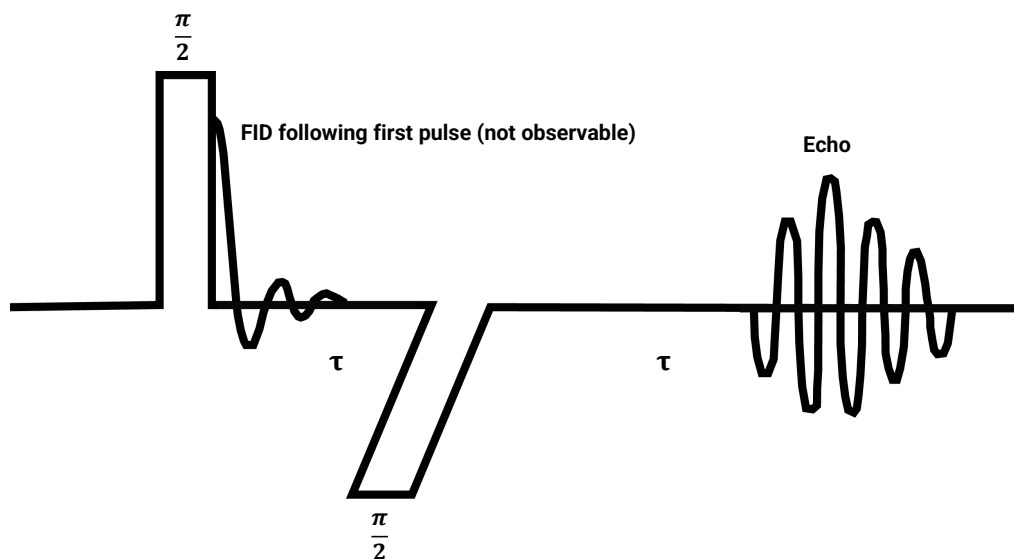


Figure 2.8 – Quadrupolar echo pulse sequence showing two $\frac{\pi}{2}$ pulses, phase-shifted by 90° , and echo formation at $t = 2\tau$.

quadrupolar Hamiltonian. Different spins evolve differently due to the range of quadrupole interaction strengths and thus get out of phase. The second $\frac{\pi}{2}$ pulse is applied in order to refocus the dephasing spins. Between these two $\frac{\pi}{2}$ pulses, after the first $\frac{\pi}{2}$ pulse, the spin system evolves freely and dephases for a time $t = \tau$. The second $\frac{\pi}{2}$ pulse inverts the phase acquired during the first period τ so that further evolution under the quadrupole interaction reverses the phase accumulation and nuclear spin refocusing takes place. Thus, the effect of a quadrupolar echo pulse sequence is an echo at time $t = 2\tau$ following the initial $\frac{\pi}{2}$ pulse. By choosing a τ value longer than the recovery time of the preamplifier, it is possible to obtain an undistorted free induction decay (FID).

Motions such as chain fluctuations, lipid acyl chain rotations, lateral diffusion of lipid molecules etc., which alter the quadrupolar interaction during the 2τ interval contribute to

echo decay. The amplitude of the echo decreases when the pulse separation τ is increased. The quadrupolar echo decay of a sample is characterised by the average echo decay rate of all the deuterons in that sample. Average echo decay rate is the weighted average of echo decay rates from all deuteron populations. For shorter pulse separation, the quadrupolar echo decay time, T_{2e} , is inversely related to the average decay rate by

$$\frac{1}{T_{2e}} = \langle R \rangle. \quad (2.9)$$

Here the average term in **Equation 2.9** is over the deuterons at different acyl chain segments. Echo decay time can be measured by collecting spectra with different pulse separations and recording the amplitudes of the echoes corresponding to each τ . Then T_{2e} can be calculated by taking the negative inverse of a plot of the initial slope of $\ln\left(\frac{A(2\tau)}{A(0)}\right)$ vs 2τ plot, where $A(2\tau)$ is the amplitude of the echo corresponding to each τ and $A(0)$ is the echo amplitude at the smallest possible pulse separation.

2.6 Phase Behaviour of Binary Lipids

In this project we use a model lipid bilayer consisting of two lipids, DPPC- d_{62} and POPG. For a membrane composed of single lipid, the phase transition from liquid crystalline phase to gel phase, is discontinuous. For binary lipid mixtures, the transition occurs over a range of temperatures for which the liquid crystalline and gel phases coexist. Spectral changes over this range can appear continuous. For comparison purposes, **Figures 2.9** and **2.10** represent the phase behaviour for a single lipid, DPPC- d_{62} , and a binary lipid combination, DPPC- d_{62} /POPG(7:3), respectively. In both figures, the top figure shows the ^2H NMR spectra and the bottom figure represents the ^2H NMR first moments.

In **Figure 2.9**, for 38 °C and above, spectra are characteristic of the chain-perdeuterated phospholipid liquid crystalline phase, while the spectra for 37 °C and below are characteristic of the gel phase. The chain melting transition temperature of DPPC is about 41 °C. Chain perdeuteration reduces the transition temperature of DPPC- d_{62} to about 37 °C [101, 102]. The discontinuous transition from one phase to another is reflected in the first moment plot. The step up at 28 °C is a pretransition [92, 102] before the main gel-liquid crystal transition. In **Figure 2.10**, the phase transition from liquid crystalline to gel phase appears continuous as it is a mixture of two lipids with very different phase transition temperatures [103]. The chain melting temperature of POPG is about -4 °C.

Below the chain melting temperature, the motions of acyl chains are more constrained, and the time scales for such motions are significantly longer. This results in bigger splittings (less motional averaging) and broader individual peaks in the spectrum (due to slower motions).

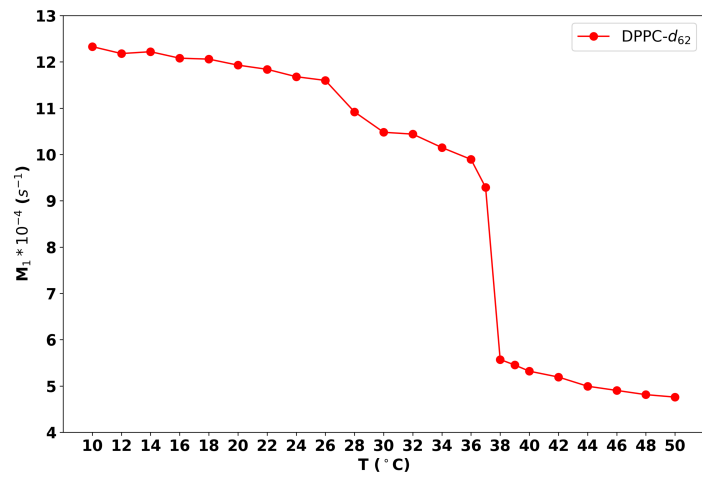
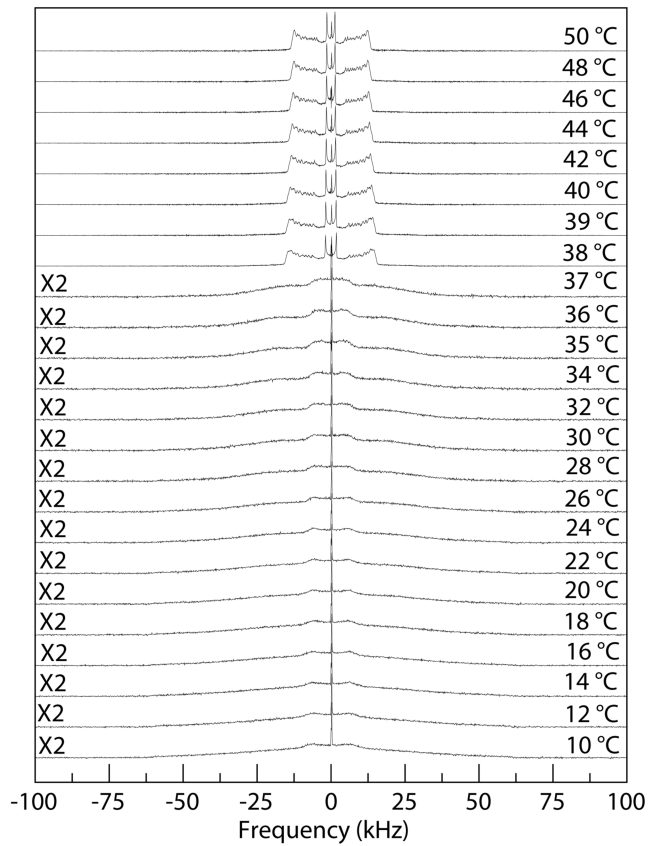


Figure 2.9 – Deuterium NMR spectra of DPPC- d_{62} (top) and the corresponding first moment plot (bottom). The transition from liquid crystalline to gel phase is observed as a discontinuous transition from 38 °C to 37 °C. The uncertainties in M_1 are comparable to the size of the symbol.

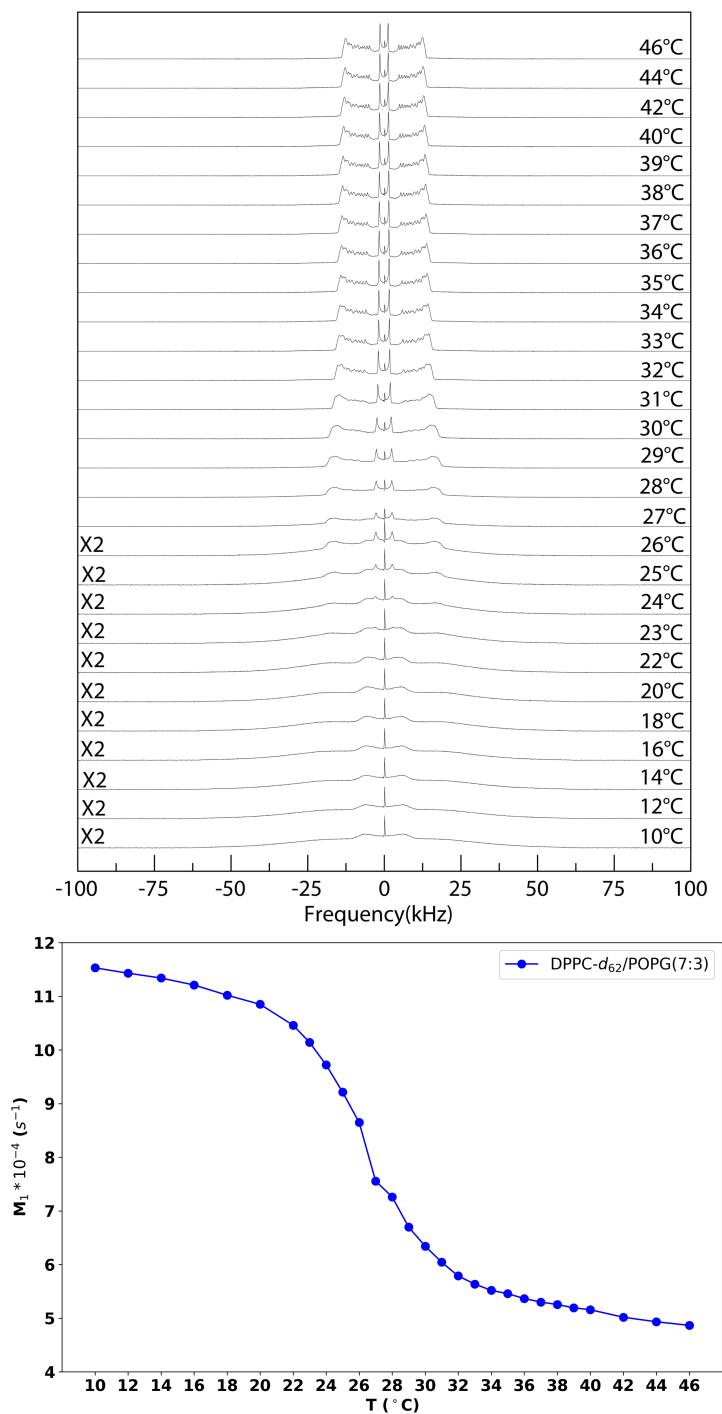


Figure 2.10 – Deuterium NMR spectra of DPPC- d_{62} /POPG(7:3) (top) and the corresponding first moment plot (bottom). The phase transition from liquid crystalline phase to gel phase is continuous. The uncertainties in M_1 are comparable to the size of the symbol.

2.7 Materials and Methods

The lipids we used in our experiments, DPPC- d_{62} and POPG, were purchased from Avanti Polar Lipids (Alabaster, USA) and were used without further purification. The peptide, SP-B₁₋₉ was purchased from Genscript Inc. (New Jersey, USA) and was desalted in Dr. Valerie Booth's lab (Biochemistry, Memorial University of Newfoundland) with the help of Mrs. Sarika Kumari (Biochemistry PhD student, Memorial University of Newfoundland). For purification, the peptide was dissolved in acetic acid solution before being transferred to a dialysis bag having a cut off of 100-500 Da. This dialysis bag was placed in a beaker containing dilute acetic acid and kept in a cold room at $-4\text{ }^{\circ}\text{C}$ with constant stirring. After 24 hours, the dilute acetic acid in the beaker was replaced by distilled water and the dialysis was continued for an additional 24 hours. The idea is to remove the salts in the peptide sample via osmosis. On the third day, the sample was transferred from the dialysis bag to a Falcon tube and freeze dried for 24 hours. The sample in powder form was obtained after this and it was weighed. This process was done two times starting with 20 mg peptide each time. The two dialysis runs yielded 19 mg and 15 mg of purified peptide, respectively.

Three multilamellar vesicle NMR samples were made: one with lipids alone and two samples with lipids and two different concentrations of peptide. Initially, $\text{CHCl}_3/\text{CH}_3\text{OH}$ (2:1) solvent was used to dissolve the lipids and peptides because this is a commonly used solvent for lipid-peptide systems. This solvent mixture, however, did not fully dissolve the peptides at higher concentrations. At higher concentrations, the peptides appeared to form undissolved film-like structures. Hence, the solvent used to mix lipids and peptides was changed to hexafluoroisopropanol (HFIP). The peptide dissolved in the HFIP completely. HFIP has been used for dissolving different SP-B fragments in previous studies [104, 105].

The lipids and protein were weighed and dissolved in HFIP in a round bottom flask (RBF). The solvent was then removed using a rotary evaporator and water bath at about 50 °C. Initial lipid samples prepared in this way showed some evidence of residual solvent in the bilayer. To obtain more complete removal of HFIP solvent, CHCl₃ was added during evaporation. For further removal of solvent, the samples were vacuum pumped using a liquid nitrogen trap overnight. Samples were then hydrated by adding about 400 to 500 μLs of 0.7 M phosphate buffer at pH 7.0 to the RBF containing the dried sample film. The flask was then rotated in a water bath at about 40-45 °C for about 45 minutes. The well-hydrated sample suspension was then transferred to a 400 μL NMR tube. In all of the experiments in this thesis, we used a DPPC-*d*₆₂/POPG ratio of 7:3 w/w and peptide-to-lipid ratios of 0, 0.066 and 0.098. While these are not physiological peptide-to-lipid ratios, they were chosen to amplify any bilayer perturbation by the peptide.

All of the ²H NMR experiments were performed on a locally assembled 9.4 T wide-line NMR spectrometer operating at a ²H NMR resonance frequency of 61 MHz using a transverse coil. A quadrupolar pulse sequence with $\frac{\pi}{2}$ pulses separated by 35 μs was used throughout the study. The NMR tube was placed inside the NMR probe, which was then placed inside the NMR machine. The temperature of the probe was maintained by a LakeShore proportional-integral-differential (PID) temperature controller (model 325, Lake Shore Cryotronics, USA). All of the experiments were carried out over a series of temperatures ranging from 46 °C to 10 °C in 2 °C steps, with the exception of the phase transition region, where the temperature was reduced in 1 °C steps. After each cooling step, the sample was allowed to equilibrate at that temperature step for about 20 minutes before the recording the spectrum.

2.8 Results

2.8.1 Deuterium NMR Spectra

Information about the phase behaviour and chain order can be obtained from the ^2H NMR spectra. We studied three samples, one with only the model lipid bilayer consisting of DPPC- d_{62} /POPG (7:3) w/w and two samples with specific concentrations of SP-B $_{1-9}$. In natural surfactants, SP-B is about 1 wt% of dry weight. Previous model systems have used about 10 wt% of SP-B, which corresponds to a mole fraction of 0.011. This is approximately ten times the mole fraction of SP-B in natural surfactants. The peptide-to-lipid ratio of SP-B $_{1-9}$ used in the multiple peptide computer simulation (discussed in the next chapter) is 0.031, which is three times the the peptide-to-lipid ratio of SP-B used in an earlier study [106] We ended up using SP-B $_{1-9}$ concentrations corresponding to two times and three times the mole fraction of multiple peptide system respectively in the two samples with peptides having peptide-to-lipid ratios of 0.066 and 0.098. The deuterium NMR spectra for these samples are shown in **Figure 2.11**.

Figure 2.11a depicts the temperature dependence of the spectra for DPPC- d_{62} /POPG (7:3) w/w reconstituted in HFIP solvent. This sample shows a continuous transition as it is a mixture of two lipids.

For a binary lipid mixture, there is a range of temperatures where liquid crystal and gel domains coexist. At the upper limit of the two phase coexistence range, most of the lipid is in liquid crystalline domains and the gel domains are enriched in the lipid with a higher melting temperature. As the temperature is lowered through the two-phase coexistence range, the fraction of the sample in gel phase domains increases and the compositions of the coexisting domains change as the gel domains become progressively enriched in

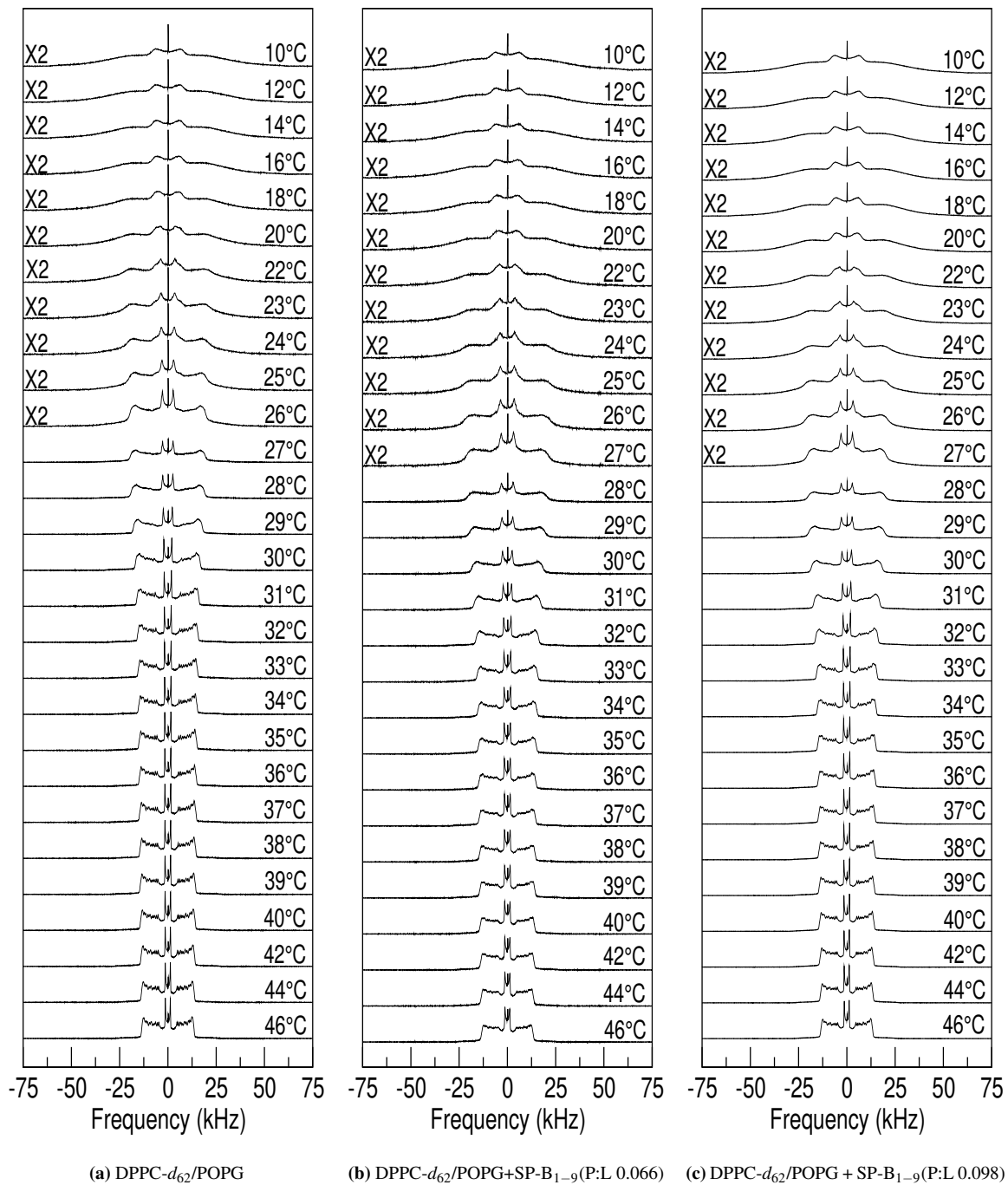


Figure 2.11 – ^2H NMR spectra of (a) DPPC- d_{62} /POPG (b) DPPC- d_{62} /POPG plus SP-B₁₋₉ with a peptide lipid ratio of 0.066 and (c) DPPC- d_{62} /POPG plus SP-B₁₋₉ with a peptide lipid ratio of 0.098.

the lower melting lipid and the liquid crystalline domains become depleted of the higher melting lipid [103]. The spectra above 27 °C are characteristic of a liquid crystalline state having axially symmetric reorientation of the acyl chains. Below 27 °C, a superposition of gel and liquid crystal phase features is observed. The sample enters completely into the gel phase below about 20 °C. Here the quadrupolar splittings are larger owing to less motional averaging and, because of the slower motions, the individual peaks in the spectra are broader. The chain melting transition temperature of DPPC is about 41 °C. As noted above chain perdeuteration reduces the transition temperature of DPPC- d_{62} , to about 37 °C. The transition in samples having a combination of DPPC- d_{62} and POPG occurs over a lower range of temperatures.

Figures 2.11b and **2.11c** show the spectra of samples with SP-B₁₋₉ at peptide-to-lipid ratios of 0.066 and 0.098, respectively. These spectra show transitions that are similar to those seen in the absence of peptide. The presence of these two SP-B₁₋₉ concentrations appears to have little effect on the spectra. A closer examination of the liquid crystalline spectra of all three samples reveal some spectral broadening. This relates to slow motion. Slow motions may depend on the size of the vesicles, which is determined by the way the sample is hydrated. As mentioned in the methods section, we initially reconstituted the samples with CHCl₃/CH₃OH (2:1). The three samples depicted in the figure are dissolved using HFIP solvent. Because HFIP was difficult to remove, it is possible that some of the spectral broadening might be due to the solvent's residual effects.

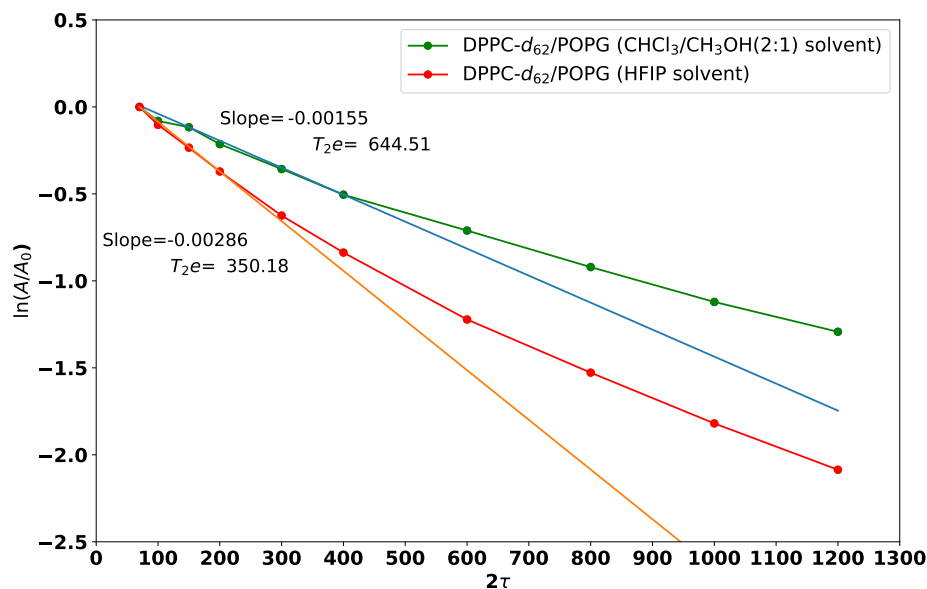


Figure 2.12 – Quadrupolar echo amplitude decay for DPPC- d_{62} /POPG(7:3) samples made using CHCl₃/CH₃OH (2:1) and HFIP solvents. The negative inverse of the initial slope gives T_{2e} . The blue and orange lines show linear fits to the initial regions of the corresponding curves.

Quadrupolar echo decay, which affects spectral broadening, is related to slow motions. In order to gain some insights into how preparation using HFIP might affect spectral broadening, echo decay times were measured for lipid-only samples prepared with and without HFIP. The effective transverse relaxation time, T_{2e} , of lipid-only samples prepared in two different solvents was calculated. **Figure 2.12** depicts the quadrupolar echo amplitude decay as a function of pulse separation, 2τ . The inverse initial slope of this plot gives T_{2e} . The smaller value of T_{2e} for the sample prepared with HFIP is consistent with some spectral broadening. We do not know why the solvent affects slow motions but one possibility might be an effect on interactions between adjacent bilayers that affect bilayer undulations.

2.8.2 Deuterium NMR First Moments

Deuterium NMR first moment (M_1) is proportional to average quadrupolar splitting. It is also proportional to the average orientational order parameter.

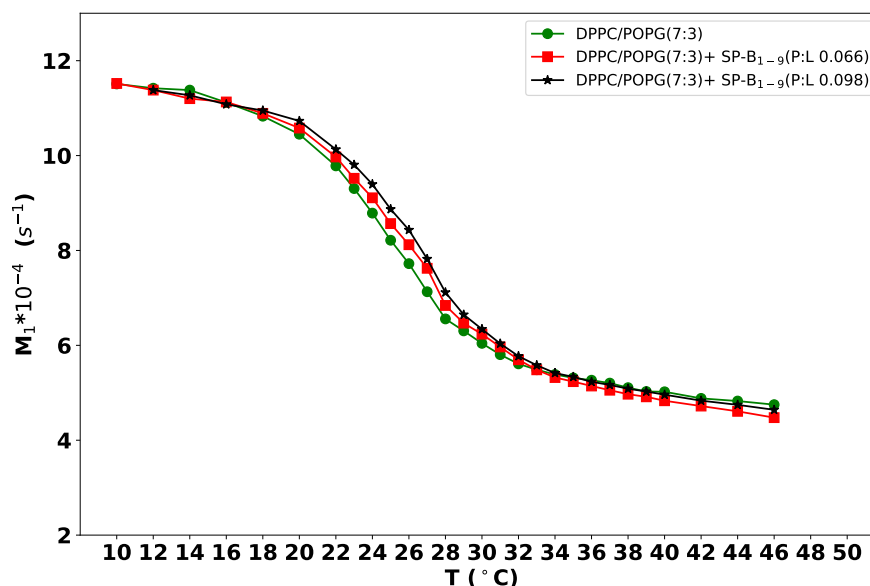


Figure 2.13 – ^2H NMR first moment as a function of temperature for (green circles) lipid only system composed of DPPC- d_{62} /POPG(7:3), (red squares) DPPC- d_{62} /POPG(7:3) with SP-B₁₋₉ (P:L 0.066), and (black stars) DPPC- d_{62} /POPG(7:3) with SP-B₁₋₉ (P:L 0.098). The uncertainties in M_1 are comparable to the size of the symbol.

First moments were calculated to study the effect of SP-B₁₋₉ on the average acyl chain orientational order of DPPC- d_{62} /POPG model lipid bilayers. The first moments (M_1) obtained for the ^2H NMR spectra of the three samples in **Figure 2.11**, plotted as a function of temperature, are shown in **Figure 2.13**.

The red curve (squares) represents a sample with SP-B₁₋₉ having a peptide-to-lipid ratio of 0.066, the black curve (stars) is the sample having 0.098 peptide-to-lipid ratio, and the green curve (circles) corresponds to the sample containing no peptide. The presence of SP-B₁₋₉ has only a small effect on the acyl chain orientational order of the bilayer in the liquid crystalline region, but this effect does not appear to depend monotonically on the peptide concentration. There is a small shift in the first moment curves at the center of the transition, but further work is needed to determine if it is due to peptide-lipid interaction or due to some other difference between the samples. For example, if the ratios of the two lipids are even slightly different between the samples, that could also shift the center of transition. The peptide shows no effect at all in the gel phase.

2.8.3 Order Parameter Profile

To investigate the effect of SP-B₁₋₉ on the lipid bilayer, we calculated the order parameters directly from the dePaked spectra. **Figure 2.14** compares the dePaked spectra of samples containing a DPPC-*d*₆₂/POPG lipid bilayer and bilayer samples containing lipid plus two concentrations of SP-B₁₋₉. The dePaked spectra of a lipid-only sample prepared with 2:1 CHCl₃/CH₃OH solvent are shown in **Figure 2.14 (A)**, while the lipid-only system prepared with HFIP solvent is shown in **Figure 2.14 (B)**. **Figures 2.14 C and D** are the samples with peptide-to-lipid ratios 0.066 and 0.098 respectively. The broadening of individual peaks in the spectrum of HFIP-treated samples might be due to the effects of residual HFIP.

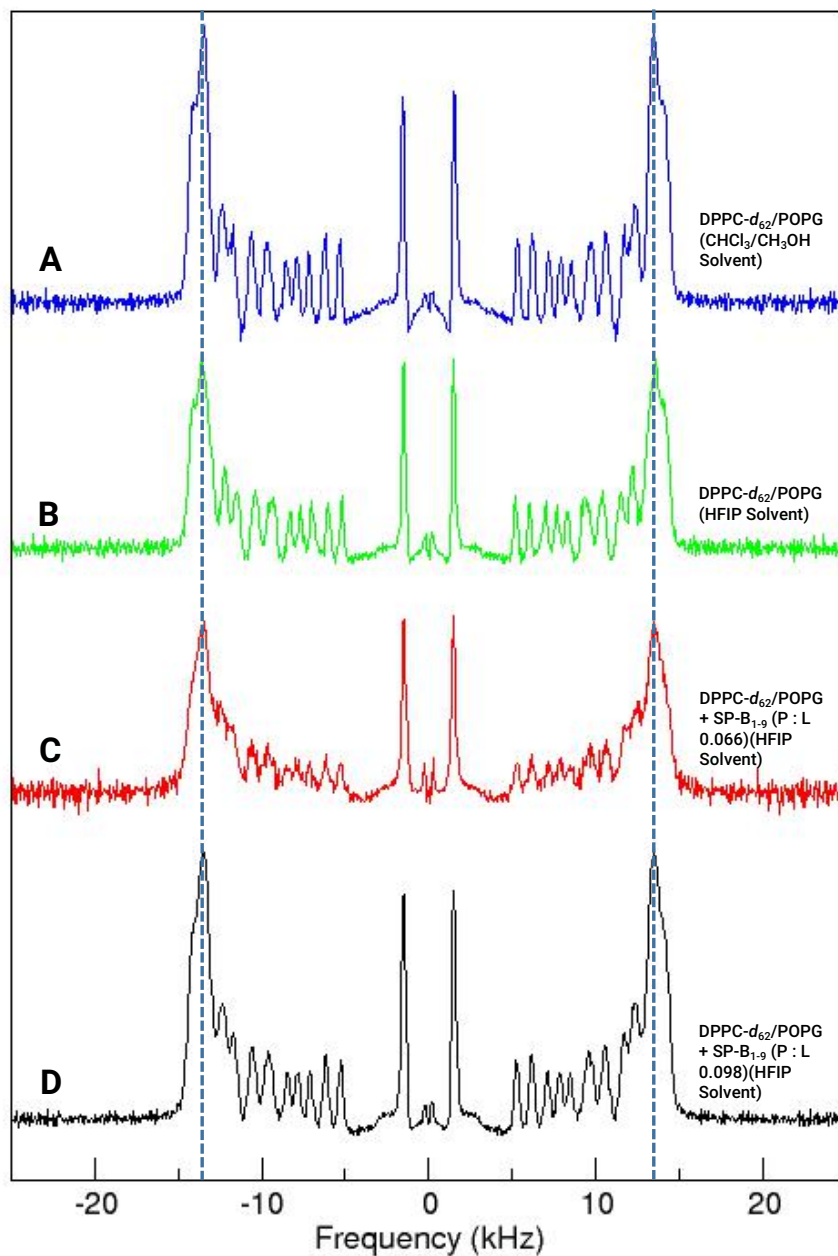


Figure 2.14 – Depaked Spectra of samples (A) DPPC- d_{62} /POPG(7:3) made using 2:1 CHCl₃/CH₃OH solvent, (B) DPPC- d_{62} /POPG(7:3), (C) DPPC- d_{62} /POPG(7:3) with SP-B₁₋₉ (P:L 0.066), and (D) DPPC- d_{62} /POPG(7:3) with SP-B₁₋₉ (P:L 0.098) at $T = 40$ °C. Samples (B), (C) and (D) are made using HFIP solvent. The dashed lines show plateau region splitting for spectrum A.

In **Figure 2.14 D**, any residual effect of HFIP seems to be smaller compared to that in the samples represented by **Figure 2.14 B** and **C**. For this sample, we performed several cycles of rotovaping with a total of about 40 ml of chloroform over the course of an hour. Then, for about an hour of rotovaping, we used a 2:1 $\text{CHCl}_3/\text{CH}_3\text{OH}$ solution, about 20 ml in total, to remove any remaining HFIP from the sample. Other than this residual effect, SP-B₁₋₉ concentrations do not have a noticeable effect on the spectra. We calculated the order parameter directly from the quadrupolar splittings to investigate the effect of SP-B₁₋₉ concentrations on the lipid bilayer. The carbon atoms are assigned to the peaks in the manner described in **Section 2.4**. This method follows the assignment scheme presented by Petrache et al. [99] and distinguishes doublets from the *sn*-1 and *sn*-2 chains. **Figure 2.15** shows the order parameter profiles of three samples made using HFIP solvent.

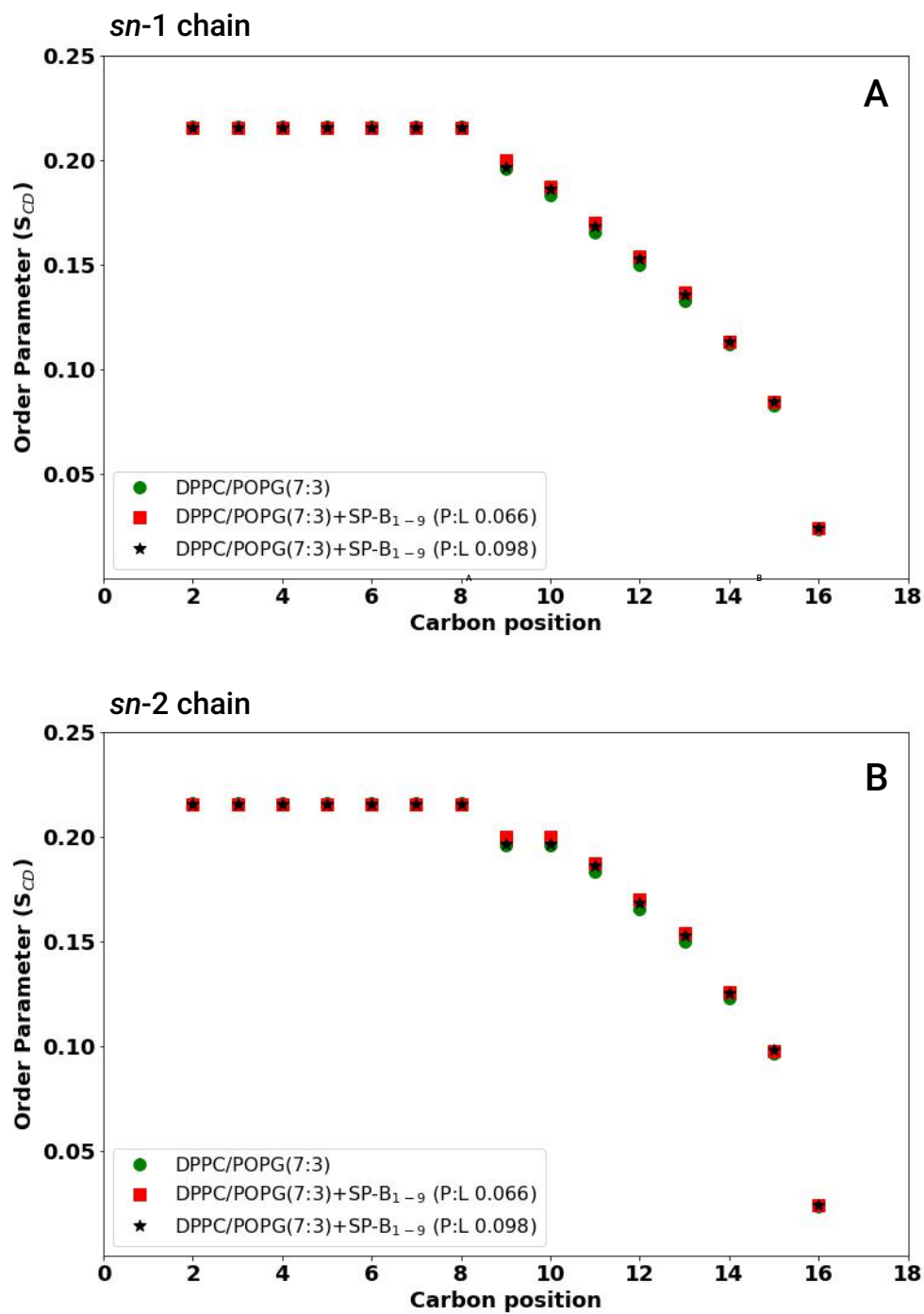


Figure 2.15 – ^2H NMR order parameter profiles of *sn*-1 (A) and *sn*-2 (B) chains of samples (Green) Lipid only system composed of DPPC- d_{62} /POPG(7:3), (Red) sample DPPC- d_{62} /POPG(7:3) with SP-B₁₋₉ (P:L 0.066) and (Black) DPPC- d_{62} /POPG(7:3) with SP-B₁₋₉ (P:L 0.098) at $T = 40^\circ\text{C}$.

These three samples have almost identical order parameter profiles, indicating that increasing the SP-B concentration has little effect on DPPC- d_{62} acyl chain order in the liquid crystalline phase of the bilayer.

2.8.4 Freeze-Thaw Cycling

One reason considered for why SP-B₁₋₉ might have little effect on lipid acyl chain order was the possibility that the peptide might be clustered in the lipid bilayer in such a way as to leave most of the lipids unperturbed. In an attempt to test for this possibility, freeze-thaw cycling was carried out on the peptide-containing samples to see if freeze-thaw might affect the dispersion of peptides in the sample in a way that might reveal some effect of the peptide on lipid acyl chain order. We began by warming the sample with peptide to lipid ratio of 0.066 in a water bath at 50 °C. The sample was then carefully immersed in liquid nitrogen until it became totally frozen, and then thawed back to its fluid condition using the water bath. This procedure was repeated about a dozen times for each sample. By doing so, we anticipated that the peptide might be distributed into the bilayer more uniformly and thereby demonstrate its effects on the bilayer. Additionally, we performed this procedure on a sample containing just lipids to determine the impact of freeze-thaw cycling on the lipid bilayer. After freeze-thaw cycling, NMR experiments were performed on both samples at 50 °C, three times, and then at 44 °C, 40 °C, and 36 °C, repeating the experiment at least twice at each temperature. To determine the impact of freeze-thaw cycling, we computed the order parameter profile for each sample and compared it to the order parameter profile acquired before. These comparisons are shown in **Figure 2.16**. The data clearly show that freeze-thaw cycling has no noticeable effect on the order parameter profiles for either the

lipid-only sample or the peptide-containing sample.

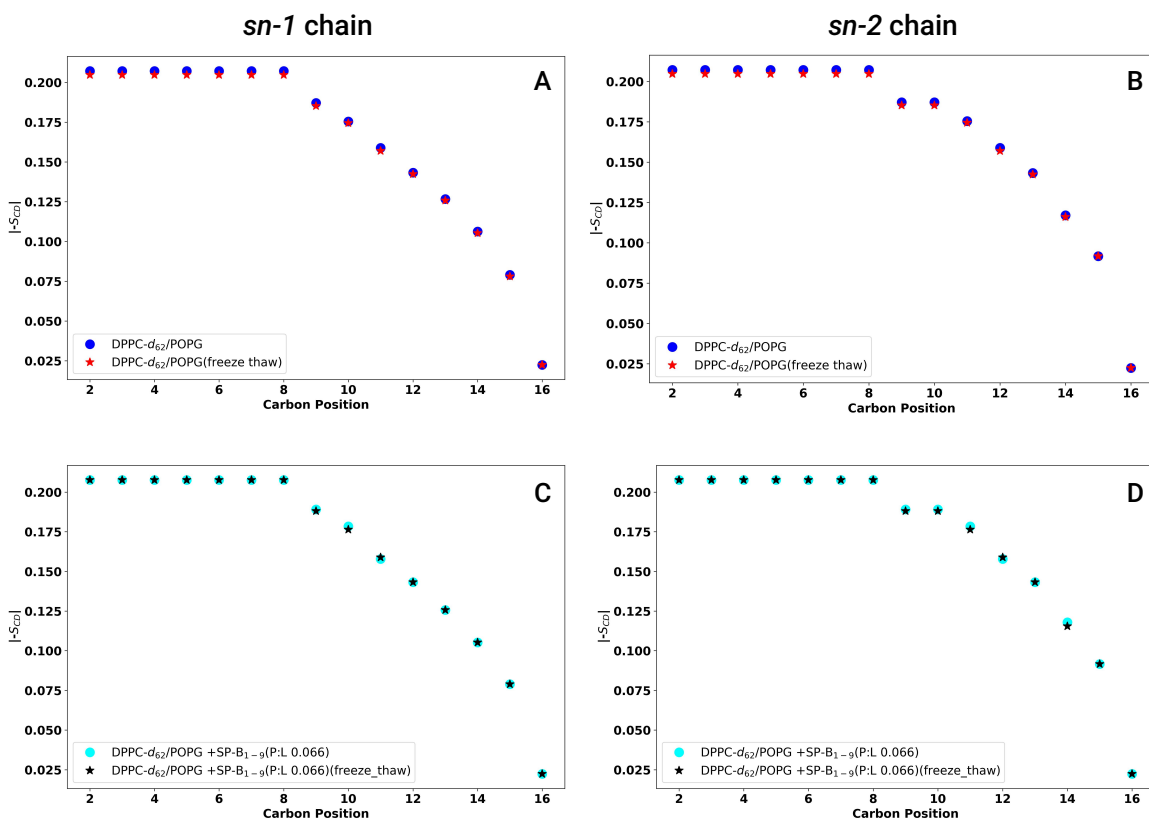


Figure 2.16 – Order parameter comparison for spectra obtained before and after freeze thaw cycling for a lipid only sample and for a sample containing SP-B₁₋₉ at a peptide-to-lipid ratio of 0.066 at $T = 44^\circ\text{C}$. Top panels show the order parameter profiles of lipid only sample, while bottom panels show the same for the sample with peptide. Panels A and C show the order parameter profiles of *sn-1* chains and panels B and D show the order parameter profiles *sn-2* chains.

The fact that the first moments and the order parameter profiles did not show any effect in the presence of higher concentrations of the peptide is remarkable. It is worth noting that one of the previous studies with full-length SP-B also did not find a considerable effect on the first moments in the presence of low concentrations of SP-B [90]. The peptide-to-

lipid ratio of the two samples (0.066 and 0.098) is very high compared to the peptide-to-lipid ratio of natural surfactants. Still, we got very close quadrupolar splitting and thereby nearly identical order parameter profiles for the sample with only lipids and the samples with two high concentrations of peptide. The lack of any effect due to high concentrations of peptide indicates either that the peptide does not have any effect on the phase behavior of lipid bilayer or that the peptide is aggregated in the ^2H NMR samples. We propose the latter over the former as the molecular dynamic simulation studies have shown effects on the lipid acyl chain order, which will be discussed in the next chapter.

Chapter 3

Computer Simulations

Molecular dynamics simulation is used for studying motion, deformation, and interaction of molecules over time. The prediction or interpretation of these changes is essential in many scientific fields. Most of the models used for studying N -body systems like biomolecules depend on assumptions that allow using Newton's equation for the motion of the atom [107]. Newton's equation of motion is given by,

$$F_i = m_i a_i. \quad (3.1)$$

Here F_i is the net force on the i^{th} particle and, m_i and a_i are the mass and acceleration of particle i , respectively. This force can be expressed as the gradient of the potential energy so that,

$$F_i = -\nabla_i V. \quad (3.2)$$

Combining equations 3.1 and 3.2, we obtain,

$$-\frac{dV}{dr_i} = m_i \frac{d^2 r_i}{dt^2}, \quad i = 1, 2, \dots, N \quad (3.3)$$

where V is the potential energy of the system, r_i is a Cartesian component of the position of the particle i , and N is the total number of particles in the system.

The acceleration of each atom in the system can be determined by knowing the force on that atom. The equations of motion can be integrated to get the trajectory of the system. The trajectory contains information about the position, velocity and acceleration of the particles in the system that varies over time. The average values of properties of the system can be calculated using these trajectories.

The potential energy of the system is a function of the atomic positions of all the atoms in the system. This function is very complicated, and hence **Equation 3.3** can not be solved analytically. Therefore, a numerical solution is needed. Several numerical algorithms were developed for the purpose of integrating the equations of motion. While selecting the algorithm for this purpose, we should consider the following criteria: (a) the algorithm should conserve energy and momentum, (b) it should be computationally efficient, and (c) it should permit a long time step for integration. One of the most commonly used ones is the Verlet algorithm [108, 109], as it conserves energy for longer times, and it produces reasonably accurate trajectories for shorter times.

Force fields are collections of potential functions and parameterized interactions that may be used for calculating forces between atoms within molecules and between molecules in a system. By using all-atom force fields, the parameters of all atom types in the system are specified. In the case of united-atom interatomic potentials, the carbon and hydrogen atoms in the methyl groups and the methylene groups are treated as a single site of interaction [110]. Choosing the best force field for our simulation depends on the properties of interest. If we are interested in the interaction of ions and ligands and in hydration free energies, OPLS [111–113] force fields are commonly used. If our interest is in secondary

structure, improved versions of AMBER [114–116] and CHARMM [117–119] are widely used. It has been shown that using the CHARMM36 force field, the latest version fine-tuned for lipids and proteins, gives a better correlation with experimental data, including ^2H NMR order parameters than the force field CHARMM22/CMAP [120] which leads to CHARMM36 being recommended for protein simulations [121]. In this study, we use the CHARMM36 all-atom force field for all our simulations.

Functional and structural investigations of biomolecules using modern simulations depend on different water models to approximate the solvent influence. In biomolecular simulations, there are two principal approaches for representing aqueous solvation: explicit and implicit solvation. In explicit solvation, the biomolecule is embedded in a box consisting of solute molecules. In implicit solvation, the solvent is considered as a structureless continuum capturing the properties of water particularly the dielectric constant [122]. Rigid fixed charged water models are considered the simplest water models and rely on non-bonded interactions. They use a simple, computationally efficient pairwise energy function proposed by Bernal and Fowler [123] in 1933. The pairwise energy function is given by

$$E = \sum_{pairs} \left(\frac{A_{LJ}}{r_{oo}^{12}} - \frac{B_{LJ}}{r_{oo}^6} + k \frac{q_i q_j}{r_{ij}} \right). \quad (3.4)$$

Here r_{oo} are oxygen-oxygen distances, A_{LJ} and B_{LJ} are Lennard-Jones parameters, k is the electrostatic constant and r_{ij} are distances between charged sites (on different molecules) with charges q_i and q_j . Models such as TIP3P [124] (Transferable Intermolecular Potential with 3 Points) are three-site models having three points of interaction which correspond to the three atoms of water. Since they are computationally efficient, they are very com-

monly used in biomolecular simulations [122]. We use the TIP3P water model for all of our simulations, as appropriate for CHARMM36 [121, 125].

Initial simulation system equilibration is usually conducted in two steps: NVT (isothermal-isochoric or canonical) ensemble and NPT (isothermal-isobaric) ensemble. In the NVT ensemble, the number of particles, volume, and temperature are kept constant, while the number of particles, pressure, and temperature are constant in NPT equilibration. NVT equilibration stabilizes the temperature of the system, while pressure and thereby density of the system are stabilized in NPT equilibration. The temperature and pressure of the simulated systems are maintained by thermostats and barostats, respectively. We employ a Nose-Hoover [126, 127] thermostat and a Parinello-Rahman [128] barostat respectively for keeping the temperature and pressure constant in our simulation production runs.

GROMACS (GRONingen MACHine for Chemical Simulations) is the most popular and one of the fastest open source molecular dynamics simulation software package available [129, 130]. It is a molecular dynamics package designed for biological systems like lipids, proteins, nucleic acids etc. We use GROMACS version 2020.2 for our simulations.

3.1 CHARMM36 Force Field

The structural and dynamic information about the lipid-lipid, lipid-protein or lipid-solvent interactions are investigated by classical molecular dynamics simulations using different models. These models are constructed around force fields, which include information on how the particles in the system interact. MD simulations based on all-atom force fields offer atomic-level information about the system's conformation and are considered complementary to experiments.

The evolution of the CHARMM additive all-atom force field (FF) [118, 131] can be traced from the early 1990s to the most current version (C36) [120]. A force field consists of two parts: potential energy function and parameter set. The potential energy function for CHARMM36 force field is given by,

$$\begin{aligned}
 E = & \sum_{bonds} K_b(b - b_0)^2 + \sum_{angles} K_\theta(\theta - \theta_0)^2 + \sum_{improper\ dihedrals} K_\phi(\phi - \phi_0)^2 + \\
 & \sum_{dihedrals} \sum_{n=1}^6 K_{\phi,n} [(1 + \cos(n\phi - \delta_n))] + \sum_{nonbonded\ pairs\ i,j} \epsilon_{ij} \left[\left(\frac{R_{min,ij}}{r_{ij}} \right)^{12} - 2 \left(\frac{R_{min,ij}}{r_{ij}} \right)^6 \right] + \\
 & \sum_{nonbonded\ pairs\ i,j} \frac{q_i q_j}{4\pi D r_{ij}} \quad (3.5)
 \end{aligned}$$

In **Equation 3.5** the parameters b , θ , ϕ and ϕ represents the bond lengths, valence angles, improper dihedral angles and dihedral angles respectively. The potential energy terms for bonds, angles and improper dihedrals are harmonic, with force constants, K_b , K_θ and K_ϕ , and with the parameters having respective equilibrium values of b_0 , θ_0 and ϕ_0 . The dihedral potential is a sum of sinusoids with force constants $K_{\phi,j}$, multiplicity n , and offset δ . The van der Waal's interactions are given by Lennard-Jones (LJ) potential. The parameter ϵ_{ij} is the minimum potential energy between two particles separated by a distance r_{ij} . The distance $R_{min,ij}$ represents the separation of atoms i and j at the minimum in the LJ potential. Finally, q_i and q_j are the partial atomic charges for the Coulombic term in the equation.

The water model is, in fact, a component of the force field, because force fields are designed to balance the solute-solute, solvent-solvent and solute-solvent interactions, commonly referred as the interaction triad [132].

3.2 Methods

3.2.1 System Setup

In order to investigate the effect of the lung surfactant peptide fragment SP-B₁₋₉ in a model lipid bilayer, we created three simulation systems consisting of model lipid bilayers containing lipids DPPC and POPG (7:3 ratio) plus no peptide, two peptides, and multiple peptides. In our simulations, DPPC is not deuterated. As noted above, chain perdeuteration lowers the transition temperature of DPPC by approximately 4 °C [101]. Refer to **Appendix A** for more details about system setup. The first step was to create the pdb file of the peptide's amino-acid sequence, FPIPLPYCW. A pdb file describes the three dimensional structure of proteins. It has information such as connectivity of atoms, the atomic coordinates and, if available, secondary structure assignment. For that, a text file was created with the peptide sequence. This text file was opened in SWISS PDB viewer [133] and saved as a pdb [134] file. Swiss PDB viewer constructed the peptide with an initial CCHHHHHHC conformation. This pdb file was then used as the peptide structure file for the simulation systems with peptide. The system with two peptides (one in each bilayer leaflet), having a peptide-to-lipid ratio of $2/518 = 0.0038$, was created first. A no-peptide system was then created by removing the peptides from the two-peptide system. The third system generated was the multiple-peptide system with 36 peptides (18 in each bilayer leaflet) giving a peptide-to-lipid ratio of $36/1160 = 0.031$. A summary of the contents of each simulation system is shown in **Table 3.1**.

Table 3.1 – Table showing the components of each simulation system and the peptide-to-lipid ratio of the two-peptide and multiple peptide systems.

Components	No Peptide	Two Peptide	Multiple Peptide
Peptide	-	2	36
DPPC	364	362	812
POPG	156	156	348
Potassium	156	156	348
Peptide:Lipid	-	0.0038	0.031

We use the CHARMM36 all-atom force field and TIP3P water model for our simulations. The N and C ends of the peptide are terminated with NH_3^+ and COO^- groups, respectively. In the simulation systems with peptides, the peptides were initially placed, with random orientations, in a staggered two-layer grid. After inserting the peptides in a cubic box, we used the CHARMM GUI [135] membrane builder to insert the lipids DPPC and POPG at a 7:3 ratio and to solvate the system with water and ions. The box dimensions of the two-peptide and no peptide systems were almost the same at the beginning, about $12 \text{ nm} \times 12 \text{ nm} \times 8 \text{ nm}$ ($x y z$), while the box dimensions of the multiple-peptide system at the beginning were about $20 \text{ nm} \times 20 \text{ nm} \times 8 \text{ nm}$. After energy minimization of the structures, short *NVT* and *NPT* simulations were carried out to allow the nominal equilibration of water and lipid molecules at $T = 310 \text{ K}$ and $P = 1 \text{ kbar}$, while the peptides were restrained in place. The box dimensions slightly changed after the *NPT* equilibration. The three simulation systems, after these initial equilibration steps are shown in **Figure 3.1** and **Figure 3.2**. The

production runs for the three systems, for which the peptides were no longer restrained, were done on the Compute Canada [136] Graham HPC cluster.

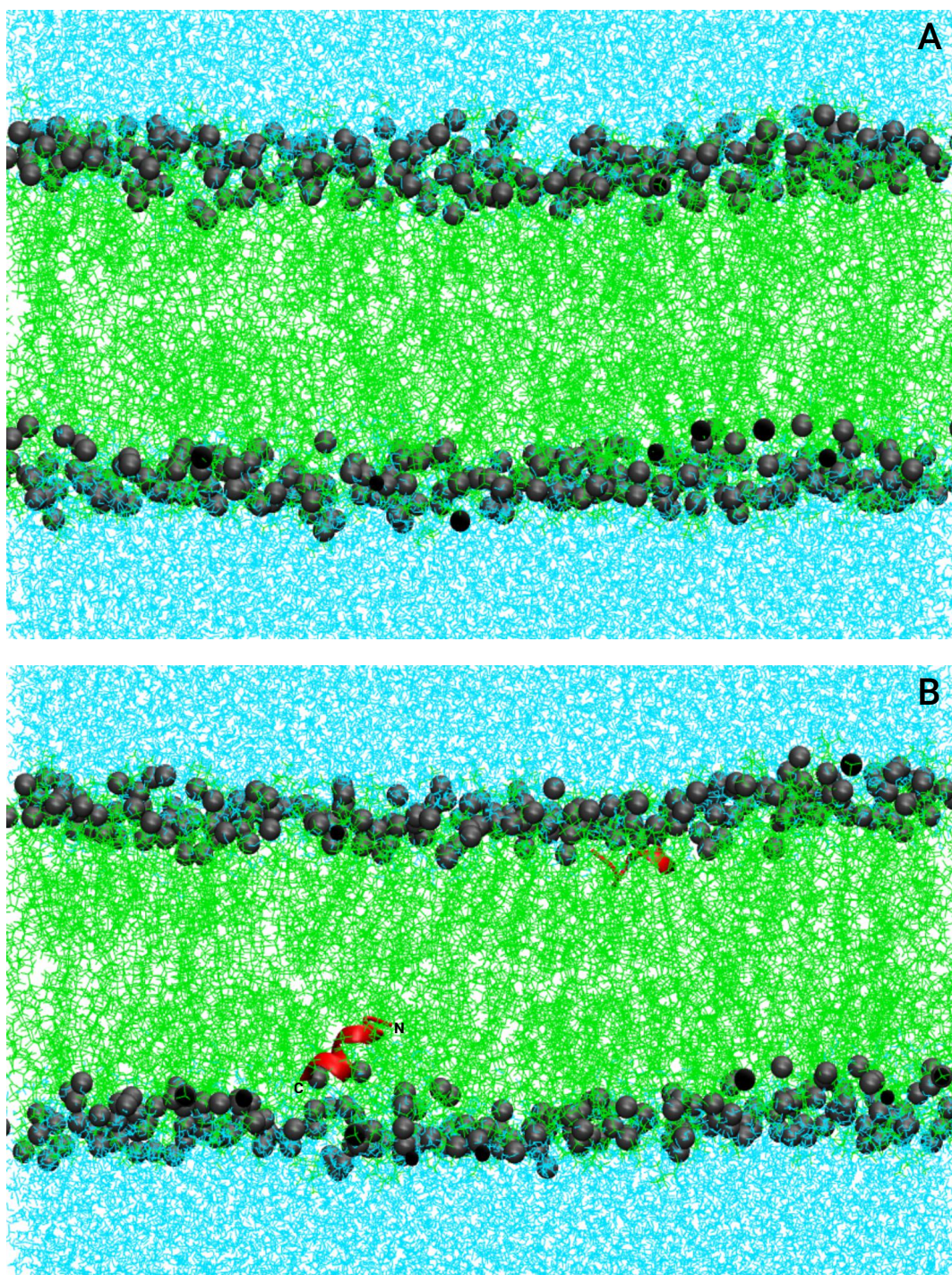


Figure 3.1 – Simulation systems after initial equilibration prior to production runs for (A) no peptide system and (B) two peptide system with a peptide-to-lipid ratio of 0.0038 at $T = 310$ K. The cyan layer indicates water molecules, grey spheres are phosphorus head groups, green indicates the lipid acyl chains and the red shows the peptide.

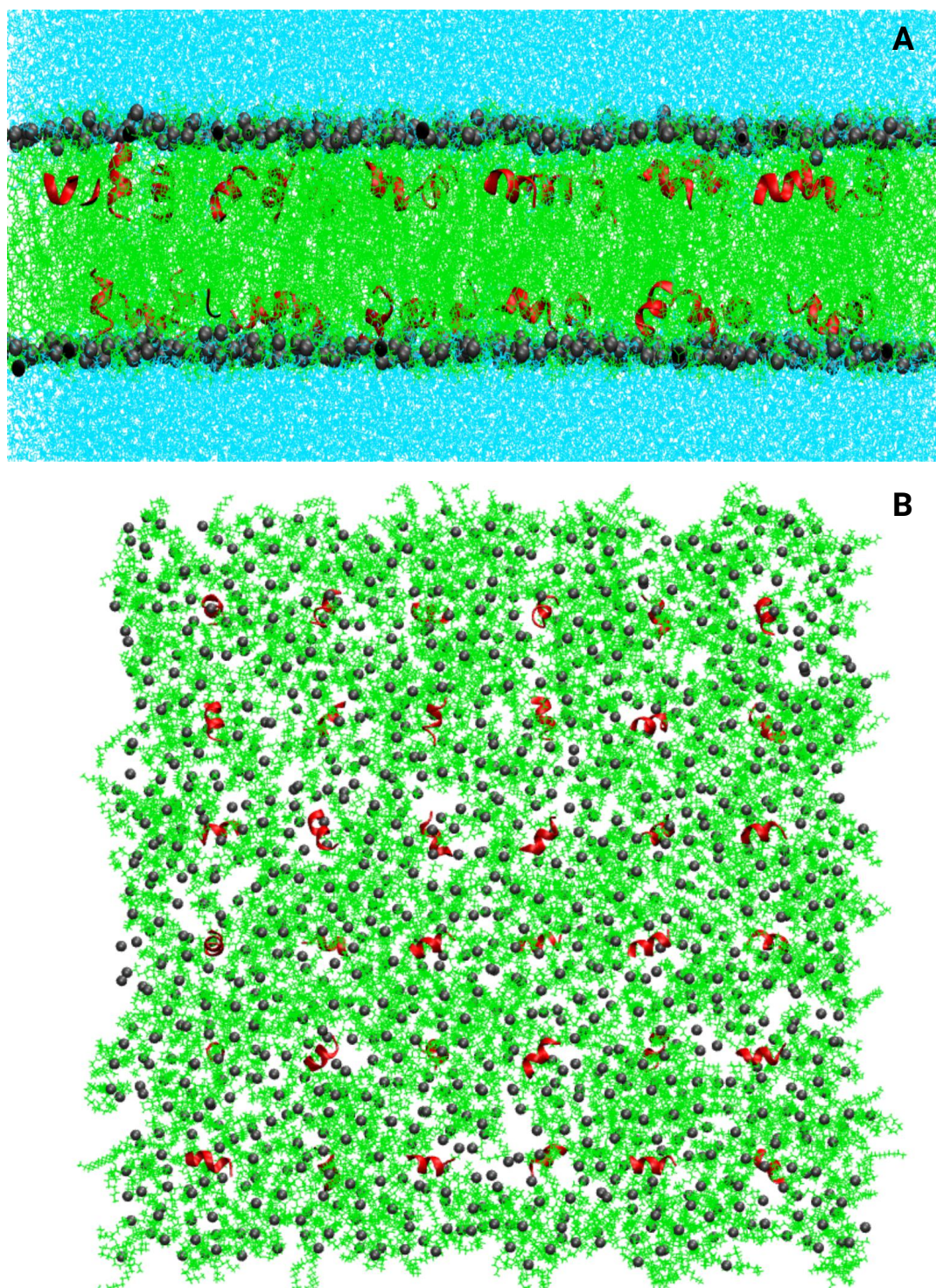


Figure 3.2 – Multiple peptide simulation system with 36 peptides having a peptide-to-lipid ratio of 0.031 after initial equilibration and prior to the production run: (A) side view and (B) top view at $T = 310$ K.

After about 150 ns of simulation, the two-peptide system appeared to settle into an ordered lipid phase, presumably the gel phase. To deal with this, the temperatures of all three systems were raised to 323 K. Energy minimization and energy equilibration steps on these three systems were carried out at 323 K before their production runs were started at 323 K. We kept running the multiple peptide system at 310 K to study the effects of temperature, since this system showed no signs of freezing. The simulation systems at $T = 323$ K at the ends of the production runs are shown in **Figure 3.3**.

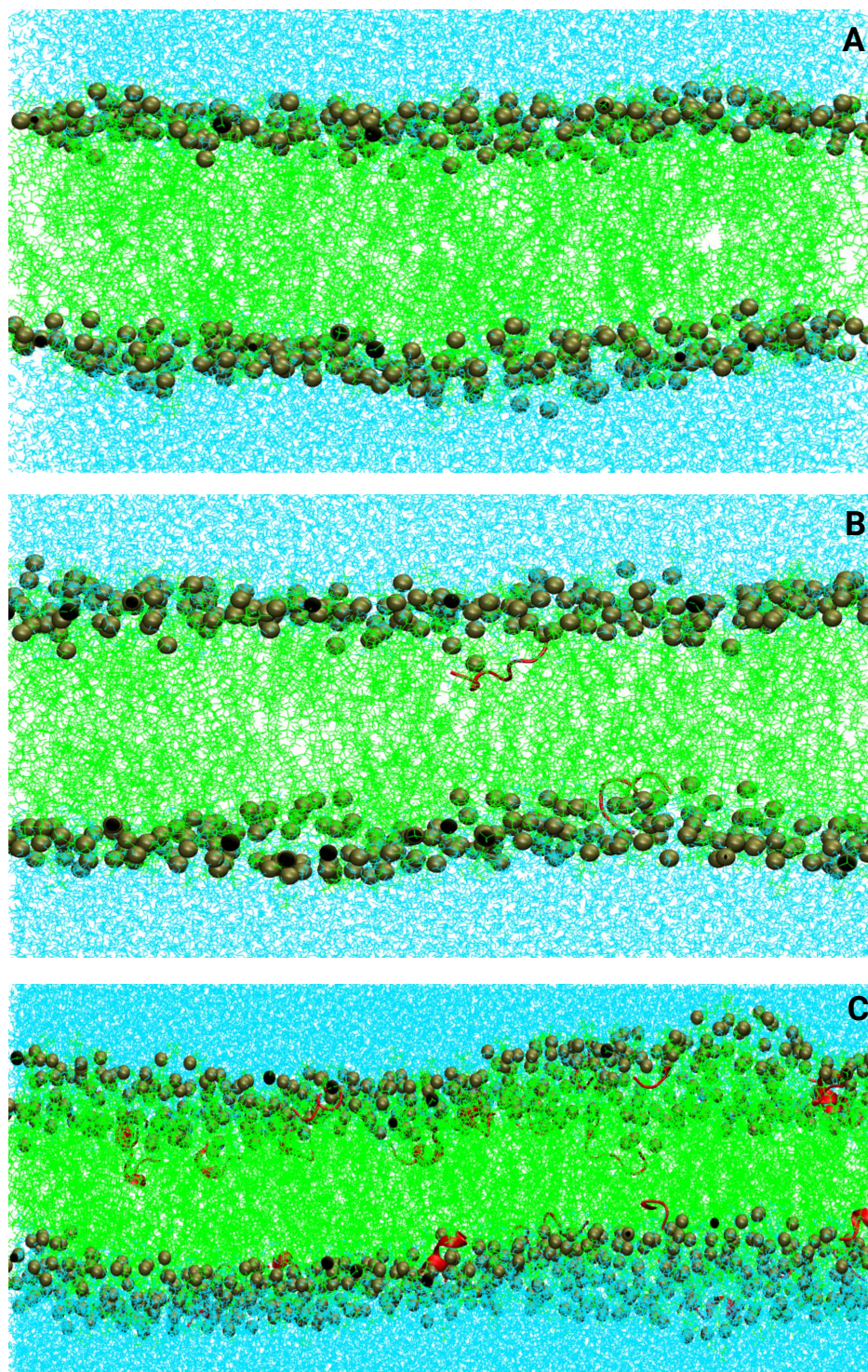


Figure 3.3 – Simulation systems (A) no peptide system after 1050 ns, (B) two peptide system after 1150 ns and (C) multiple peptide system after 450 ns, all at $T=323$ K.

3.2.2 Extraction of Order Parameter Profiles Using Membrainy Software

Membrainy is an easy-to-use Java software package, mainly developed for membrane analysis in conjunction with GROMACS [137]. It recognizes different input formats and force fields and efficiently executes multithreaded codes. Membrainy can read the GROMACS file formats tpr, trr, xtc, gro etc. and produces text files formatted for the Grace graphics software package [138]. Membrainy calculates the acyl chain CH_2 segment order parameters of both saturated and unsaturated lipids using the equation $S_{CD} = \langle \frac{1}{2}(3 \cos^2 \theta - 1) \rangle$ presented in the second chapter. Membrainy utilizes each C-H bond vector along the lipid acyl chain for order parameter calculations. It produces the order parameters of both *sn*-1 and *sn*-2 chains of each lipid in each leaflet. Membrainy plots $|S_{CD}|$ of each carbon atom along the lipid acyl chain for both all-atom and united-atom forcefields. By utilizing the C-H bond vectors, Membrainy obtains more accurate order parameter values compared to the GROMACS module *gmx order*. The *gmx order* module does not consider the C-H bond vector for calculating the order parameter, but rather reconstructs the order parameter from the $C_{j-1} - C_{j+1}$ vector. The order parameters of saturated chains calculated using Membrainy are comparable to those of *gmx order*. The two approaches are also comparable for unsaturated chains except around double bonds. This is the main reason why we use Membrainy for calculating order parameters, as POPG, one of the lipids in our bilayer, has an unsaturated chain.

3.2.3 Helicity Calculation

The assignment of secondary structural elements is a critical step in determining the three-dimensional structure of proteins. Numerous of these secondary structure assignment techniques include pattern identification of inter- C_α lengths, and analysis of bond angle, bond distances between successive C_α atoms, hydrogen bonding patterns, and backbone curvature [139]. Different approaches to identification of helicity provide results that can vary by up to 25% [140].

The assignments by crystallographers are based on consideration of hydrogen bonding using the Baker and Hubbard [141] definitions, based on the patterns of hydrogen bonding in combination with main-chain dihedral angles. Although there are various approaches, there are two very important properties of protein structure that play a major role in the structural element definition. They are patterns of hydrogen bonding and the backbone geometry expressed as main chain dihedral angles.

DSSP (Define Secondary Structure of Protein) by Kabsch and Sander [142] is a very commonly used automatic secondary structure assignment method. VMD (Visual Molecular Dynamics) [143] software uses the STRIDE algorithm [139] where the acronym stands for secondary SRTuctural IDentification.

We use the STRIDE plugin of VMD for helicity calculations. For secondary structure calculation, STRIDE relies on hydrogen bond energy and the dihedral angles associated with the peptide. ϕ and ψ are the angles of rotation around N- C_α and C- C_α bonds in a peptide. STRIDE applies a condition which depends on the hydrogen bond energy and the ϕ and ψ angles which needs to be satisfied for a residue to be considered as part of a helical structure [139]. If two consecutive hydrogen bonds between residue pairs ($j, j+4$)

and $(j+1, j+5)$ satisfy the STRIDE conditions, then the residues, $j+1, j+2, j+3$ and $j+4$ are identified as being in an α -helical structure. Additionally, helices are extended to edge residues j and $j+5$ if they have ϕ and ψ values consistent with helical structure. Likewise, if ϕ - ψ values are not favorable, a short segment can be identified as non-helical. This means that if the values of ϕ and ψ are not in the acceptable range, hydrogen bonding patterns are insufficient to label residues as part of helical segment.

3.3 Results

3.3.1 Energy Time Series

Time series of the potential energy for the three systems at 323 K, shown in the **Figure 3.4**, indicate that the three systems are equilibrated. The blue lines indicate the time range used for analysis for each system. For the no-peptide system, it is 50 ns to 1050 ns. For the two-peptide system, it is 250 ns to 1150ns. For the multiple peptide system it is 75 ns to 450 ns. We have calculated average order parameter profiles for these systems over their respective time ranges. The calculations of helicity, density and residue location from the multiple peptide system were done over the time range of 75 ns to 450 ns.

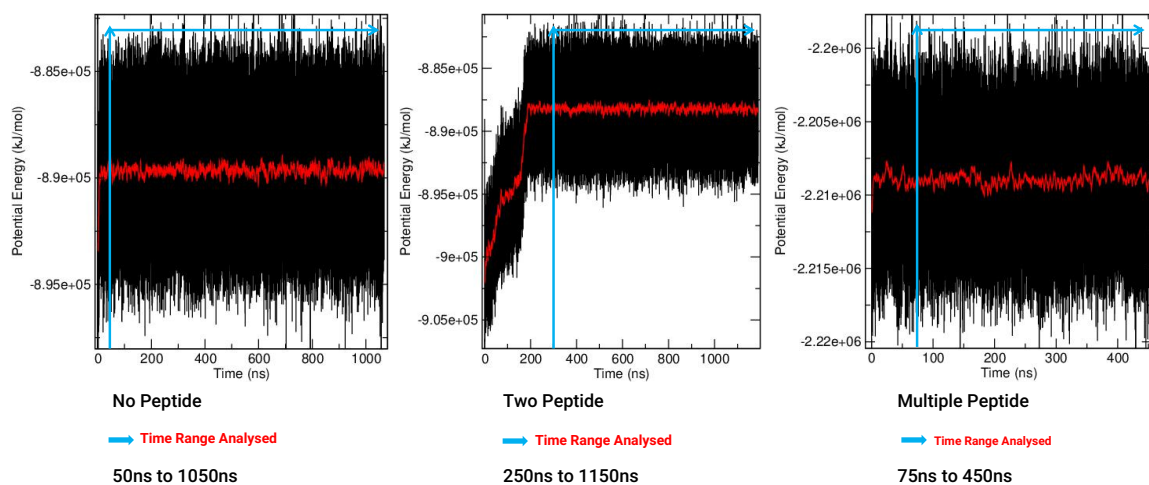


Figure 3.4 – Time evolution of potential energy of the no-peptide system (left), the two peptide system (middle) and the multiple-peptide system (right) at $T = 323$ K. The constant nature of the energy-time series to the right of blue bars shows that the systems have attained equilibrium. The black data points represent the complete data, while the red curve represents the running average over 1000 ps.

The initial rise in the energy seen in the time series for the two-peptide system ($T < 200$ ns) reflects thawing of the partially frozen starting configuration, which was taken from a simulation at 310 K, as noted above. The other two systems showed little (no-peptide) or no (multiple-peptide) freezing during simulations at 310 K. We note that the no-peptide system would be expected to freeze if the system were allowed to run longer. Refer to **Appendix B.1** for details about calculating the energy-time series.

3.3.2 Order Parameter Profile

Order parameter profiles are obtained using Membrainy over the steady-state time range and used for analysis of the equilibrium state. Using Membrainy we obtain the order pa-

parameter profile of each chain of each lipid component in the lipid bilayer. Refer to **Appendix B.2** for details. The order parameter profiles obtained for the three samples over the time range analysed is shown in **Figure 3.5**

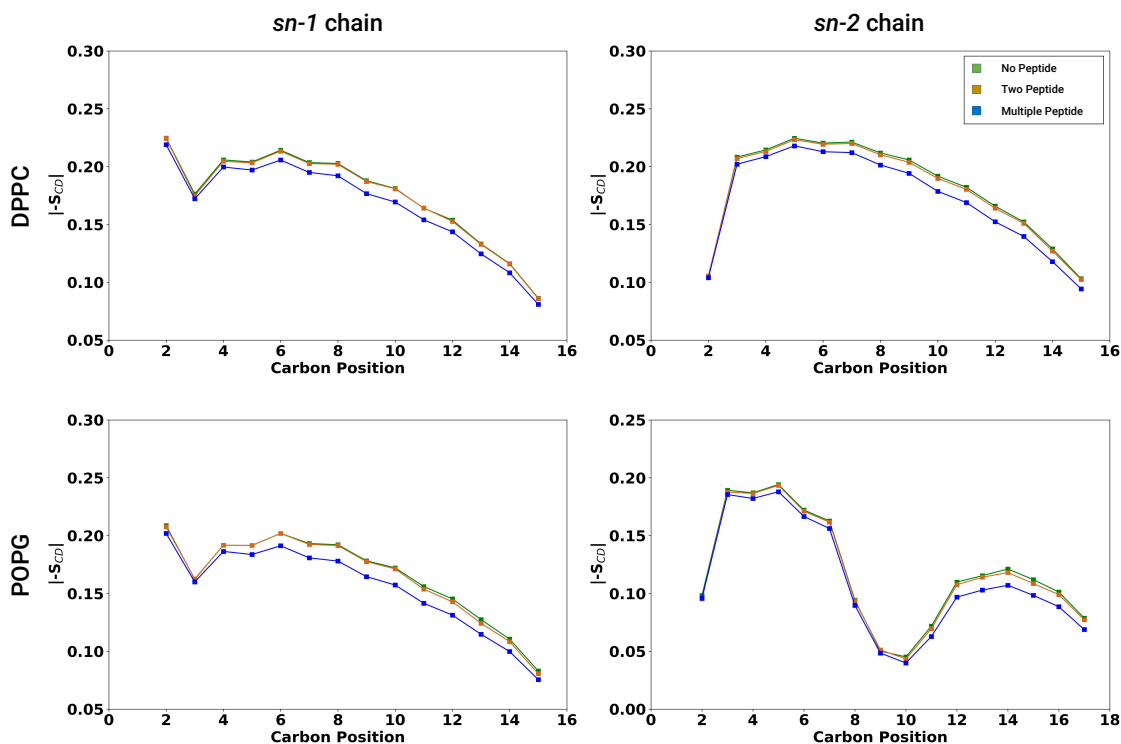


Figure 3.5 – Order parameter comparison of No peptide (olive), Two peptide (brown) and Multiple peptide (blue) systems. Order parameters of *sn*-1 and *sn*-2 chains of DPPC and POPG of the three systems at $T=323\text{K}$ are shown in figure. The uncertainties in order parameters are estimated to be ± 0.001 and that is comparable to the symbol size.

It is clear from the figure that the large concentration of peptide in the multiple-peptide system has an effect on the order parameter profile compared to the other two systems. It is also noticeable that the order parameter profile of the two-peptide system is below that of the no-peptide system, indicating that the presence of the peptide has an effect of reducing

the acyl chain orientational order of the lipid bilayer. This is contrary to what we obtained from the experimental order parameter profile, where we did not see any effect of peptide on the lipid bilayer.

In **Figure 3.6**, we plot DPPC order parameter profiles from simulations at 323 K (50 °C) and experiments at 319 K (46 °C), the closest point of comparison in terms of temperature. **Figure 3.6 A** and **3.6 B** show profiles for *sn*-1 and *sn*-2 chains, respectively, where peptide is absent. **Figure 3.6 C** and **3.6 D** likewise show separate chain comparisons, but for the case when peptide is present; for experiments, the peptide-to-lipid ratio (P:L) is 0.066, and for simulations P:L = 0.031, which is the closest point of comparison in terms of peptide concentration. The comparisons show that the experimental order parameter profiles at 46 °C are close to the simulated order parameter at 50 °C (323 K). The agreement between experimental and simulation data is remarkable in the case of systems with peptide (panels C and D). Although the agreement is not as close in the case of systems where the peptide is not present, they are still reasonably close.

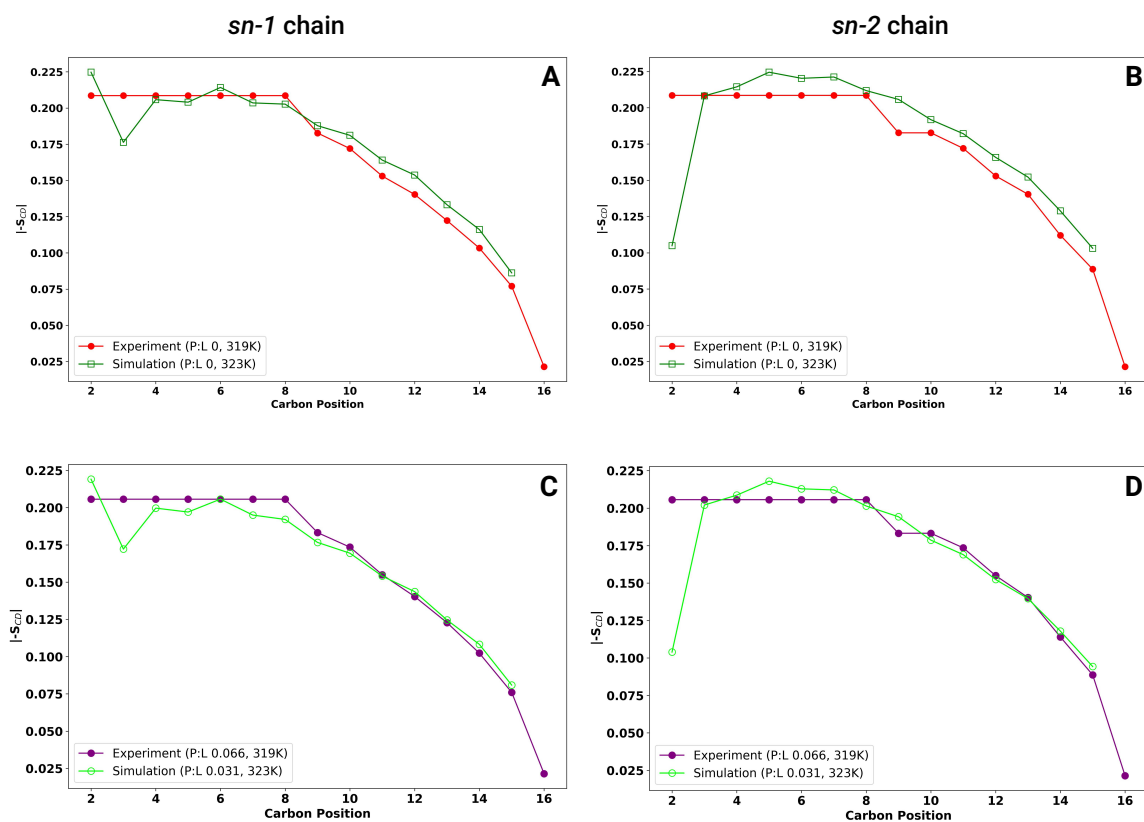


Figure 3.6 – Comparison of simulation S_{CD} at 323 K (50 °C) with experimental S_{CD} at 319 K (46 °C) for DPPC for (top) a lipid-only sample and for the no-peptide simulation system and (bottom) and for the sample with SP-B₁₋₉ having a peptide-to-lipid ratio of 0.066 and for the multiple peptide system with a peptide-to-lipid ratio of 0.031. Panels A and C show the order parameter profiles of *sn-1* chains and panel B and D show that of *sn-2* chain.

We also wanted to compare results from the multiple-peptide system that was left running at 310 K with the closest corresponding experimental observations. The multiple-peptide system that we kept running at lower temperature (310 K/ 37 °C) did not reach full equilibrium. The energy-time series for that system is shown in **Figure 3.7**.

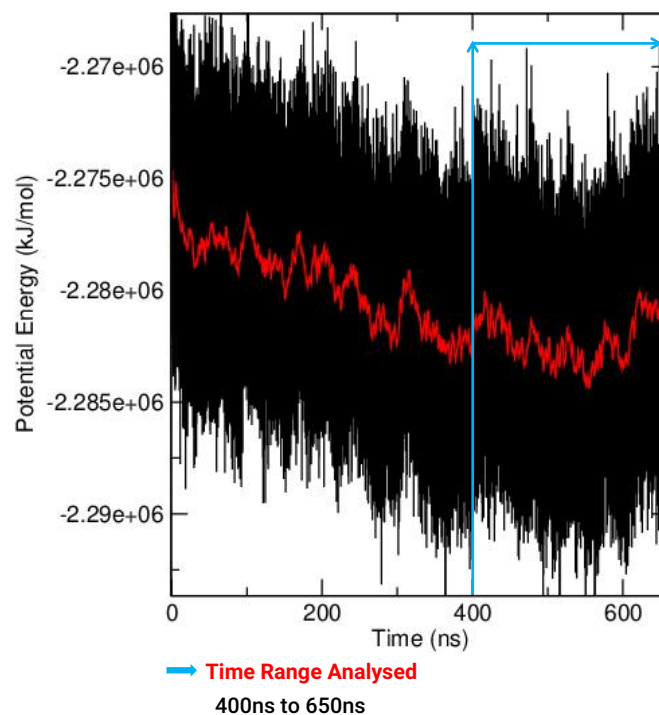


Figure 3.7 – Time evolution of the potential energy for the multiple peptide system at $T=310\text{K}$. The system is not yet equilibrated.

We compared the S_{CD} of the multiple peptide simulation system at the lower temperature ($310\text{ K}/37\text{ }^{\circ}\text{C}$) with the experimental sample containing SP-B₁₋₉ (P:L 0.066) at $37\text{ }^{\circ}\text{C}$. That comparison is shown in **Figure 3.8**. We used the time range of 400-650 ns in the simulation for the order parameter calculation. The energy time series is not yet equilibrated during this interval but the simulated S_{CD} profile is close to the experimental profile, indicating that the simulation agrees reasonably well with the experiments. The experiment-simulation agreement at lower temperature is closer to agreement at higher temperature shown in the bottom panels of the **Figure 3.6**. As it is hard to resolve the ^2H NMR spectral splittings closer to the headgroup, few carbon positions are assigned the same quadrupole

splitting and hence the same S_{CD} as mentioned in **Section 2.4**, resulting in a “plateau” in the S_{CD} curve. The straight line region at the beginning of the experimental S_{CD} represents this plateau region.

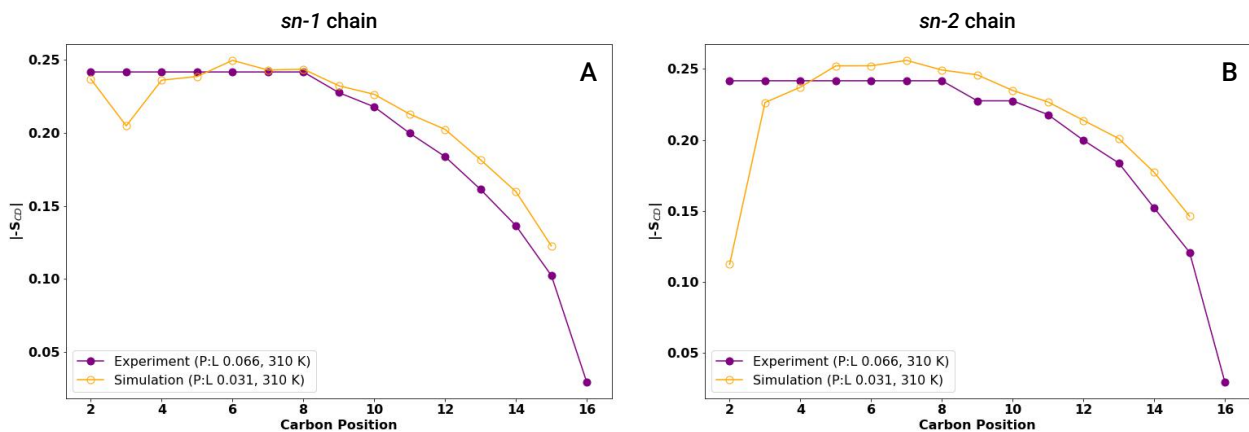


Figure 3.8 – Comparison of order parameter profiles of DPPC of multiple-peptide system having a peptide-to-lipid ratio of 0.031 at 310 K (37 ° C) with experimental S_{CD} at 310 K (37 ° C) of sample with SP-B₁₋₉ having a peptide-to-lipid ratio of 0.066. Panel A and B show the order parameter profile of *sn*-1 and *sn*-2 chains respectively.

3.3.3 Average Helicity of the Peptide

The average helicity of the peptides in the multiple-peptide system was computed to get information about their structure. We calculated the secondary structure using the STRIDE plugin of VMD. Then, we utilised Python to manipulate the secondary structure file extracted from VMD in order to calculate the helicity percentage. See **Appendix B.3** for details. Helicity percentage is the percentage of the helical structures over the time range analyzed.

We examined secondary structure labels that STRIDE uses to calculate secondary struc-

tures. They are C (coil), T (turn), G (3-10 helix), and H (α -helix). We have included both α -helix and 3-10 helix as helical in our calculations. The helicity percentage of each residue in each peptide in the multiple-peptide system was determined over the 3750 time frames of the equilibrated portion of the trajectory plotted as a function of residue in **Figure 3.9**. The helicity percentage of each residue varies with each peptide. For each residue, a range of helicity percentage value is observed. It is noticeable that calculated helicities for the first two residues (F and P) and the last residue (W) for all the peptides are zero, as we discuss below. The trend in variation of helicity percentage value for each residue seems to be similar for each individual peptide.

We took the average of helicity over the 36 peptides in the system to get the average helicity of each residue and plotted it as a function of time frame in **Figure 3.10**. Then we took the average of these over the time frame analysed and plotted it as a function of residue in **Figure 3.11**

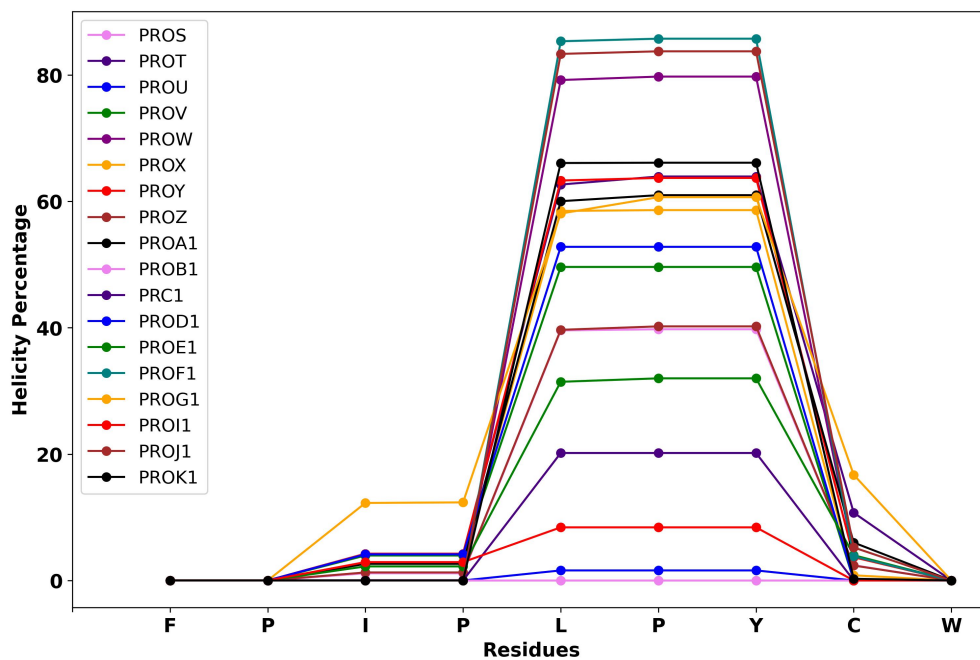
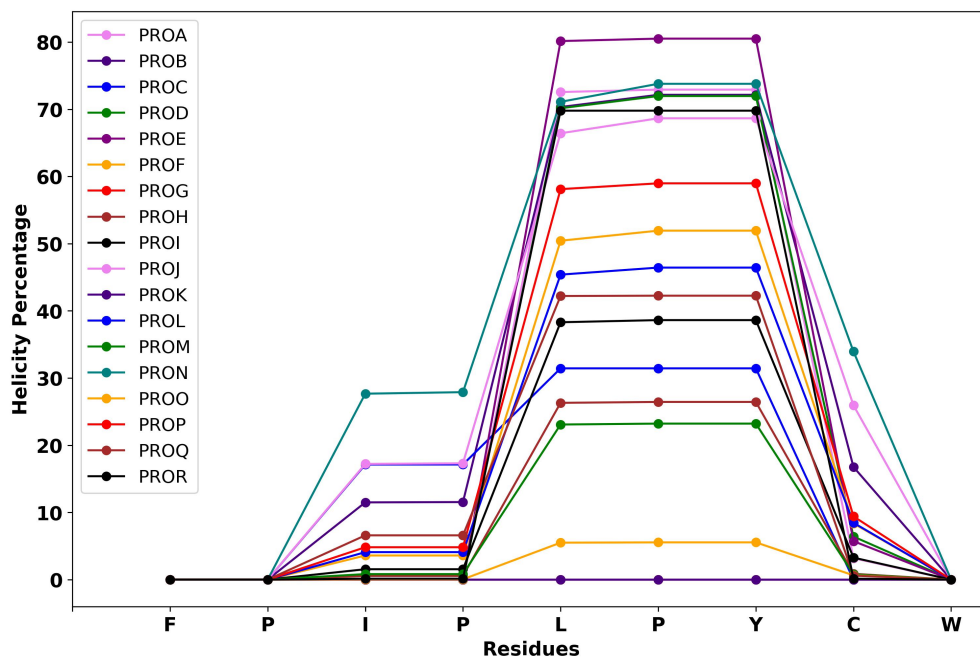


Figure 3.9 – Helicity of each residues of each peptide in the multiple peptide system averaged over 3750 time frames. The 36 peptides in the multiple peptide system are labelled as PROA, PROB, etc. so that each point is the average of 3750 helicities determined for that residue in a specific peptide.

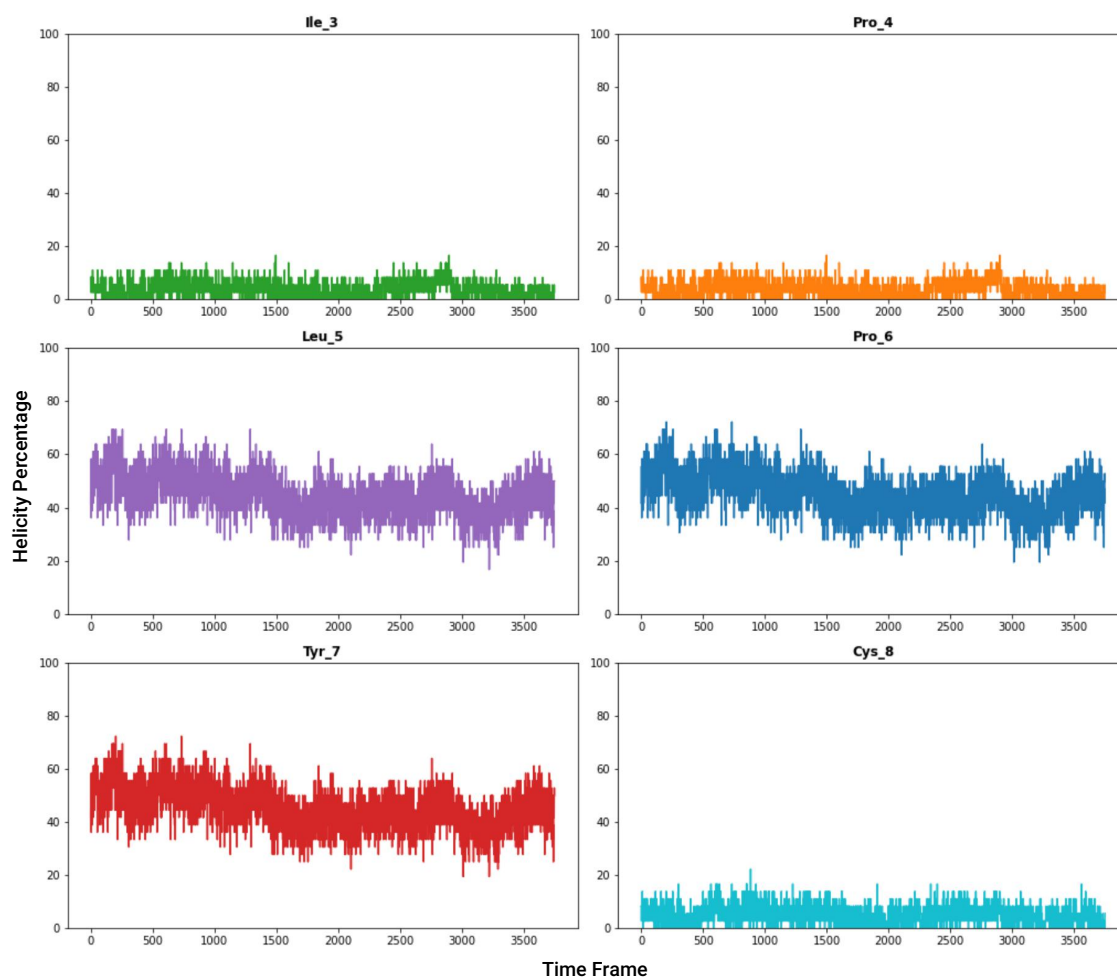


Figure 3.10 – Time evolution of percentage helicity of the six residues of the peptide with some helicity. The first, second and last residues (Phe_1, Pro_2 and Trp_9) were found to be always zero from **Figure 3.9**. Each point is an average over the 36 helicities for the indicated residue at a single time.

The helicity percentages calculated for residues Phe_1, Pro_2 and Trp_9 were found to be consistently zero for all the 36 peptides over the time range analysed. This is in account of how STRIDE works. For example, the proline is considered as a helix breaker since it cannot form a hydrogen bond [144]. In the amino-acid sequence of the peptide, FPIPLPYCW, the proline at position two cannot have a hydrogen bond with the proline at

position five. Hence, according to the condition for α -helical structure mentioned in the **Section 3.2.3**, both F and P at the beginning of the sequence cannot be considered as being part of the helical region. In the case of tryptophan (W) at position nine, it is not bonded with another residue at the end.

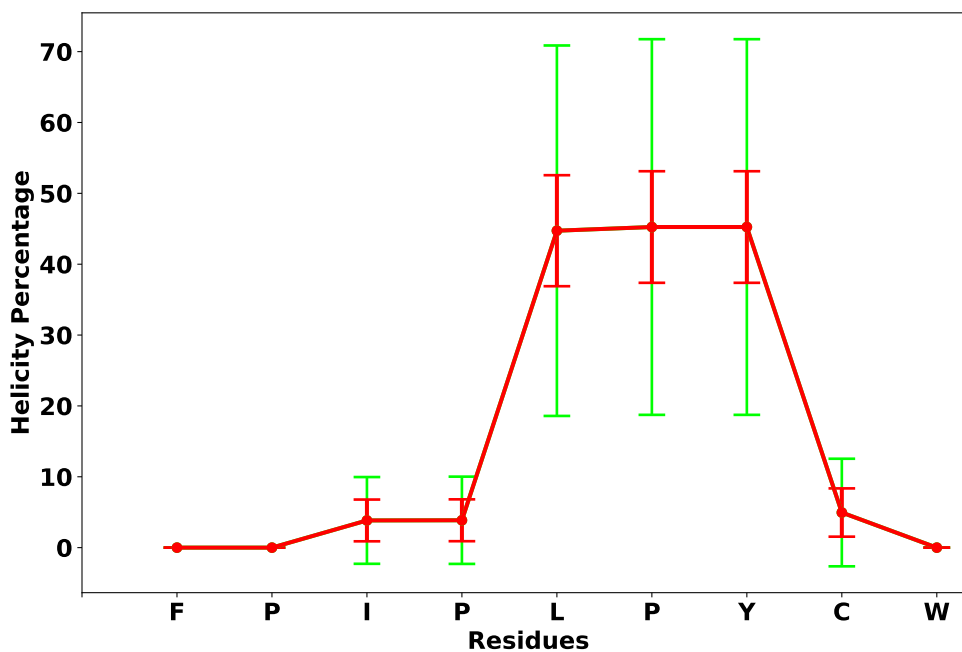


Figure 3.11 – Helicity of each residues of each peptide in the multiple peptide system averaged over 36 peptides and each time frame. The time series shown in **Figure 3.10** is averaged over each residue. The vertical green lines indicate the standard deviation obtained from 36 peptides in **Figure 3.9** and the red lines indicate the same obtained from the time-series shown in **Figure 3.10** . The residues at position 5, 6 and 7 have the potential for being part of a helical segment.

These figures show that the residues leucine, proline and tyrosine at peptide positions 5, 6, and 7 respectively have the potential of being helical. This is consistent with the helicity

calculated for the “open-in” configuration of full-length SP-B calculated using STRIDE by M.H. Khatami et al [145], even though their calculation used a different potential. These residues being helical is significant. If a peptide is not helical, its conformational flexibility might be better able to accommodate the packing of lipid chains around it. But the helical regions are compact and may create a volume from which the acyl chains are excluded. Due to this excluded volume helical regions might be more disruptive of the chain packing which could affect lipid chain orientational order.

3.3.4 Average Orientation of the Peptide

3.3.4.1 Average Density Profile

In order to get information about the average orientation of the peptide in the multiple peptide simulation bilayer, average density profiles of the C_{α} for each residue were calculated over the time range analysed. Details about this calculation can be found in **Appendix B.4**. Densities were calculated as a function of z , the coordinate normal to the bilayer. C_{α} is the central backbone atom of an amino acid. The hydrogen(-H), amino group (-NH₂), carboxylic acid (-COOH) and side chain (-R) specific to each amino acid are attached to this C_{α} . We averaged density as a function of the z coordinate for each residue over all the 36 peptides and plotted the result for each residue in **Figure 3.12**. The purple curve (highest peaks) represents the average density of phosphorus atoms on the lipid head groups. It is scaled a factor of 1/1000. Here each peak of each component corresponds to the upper and lower bilayer leaflets respectively.

The density profile shows that the peptide resides near the phospholipid head groups rather than near the bilayer center. The tryptophan residue of the peptide seems to be

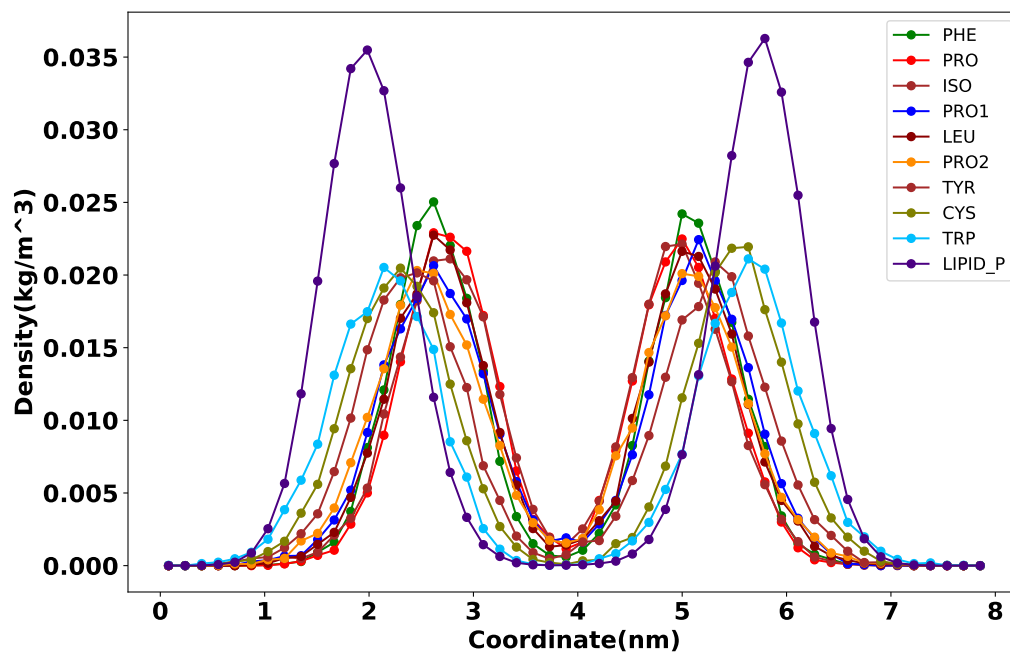


Figure 3.12 – Average density profile of C_{α} of each residues of the peptide averaged over the 36 peptides in the multiple peptide simulation. The purple curve represents the phosphorus of the lipid head groups and the remaining curves represent the nine residues of the peptide. The plot of phosphorus atoms of lipids is scaled by 1000.

closer to the bilayer surface compared to other residues. This is the expected behaviour as tryptophan is thought to anchor the peptide near the bilayer surface.

3.3.4.2 Average Depth of Peptide Residues

To get an estimate of the peptide's average orientation in the lipid bilayer, we computed the average depth of each peptide residue within the bilayer. We obtained the peak locations by fitting the C_{α} density curves with a double Gaussian function. Refer to **Appendix B.5**. Similarly, we determined the peak locations of the density profiles of each residue's C_{α} .

These are plotted against residue number in **Figure 3.13**.

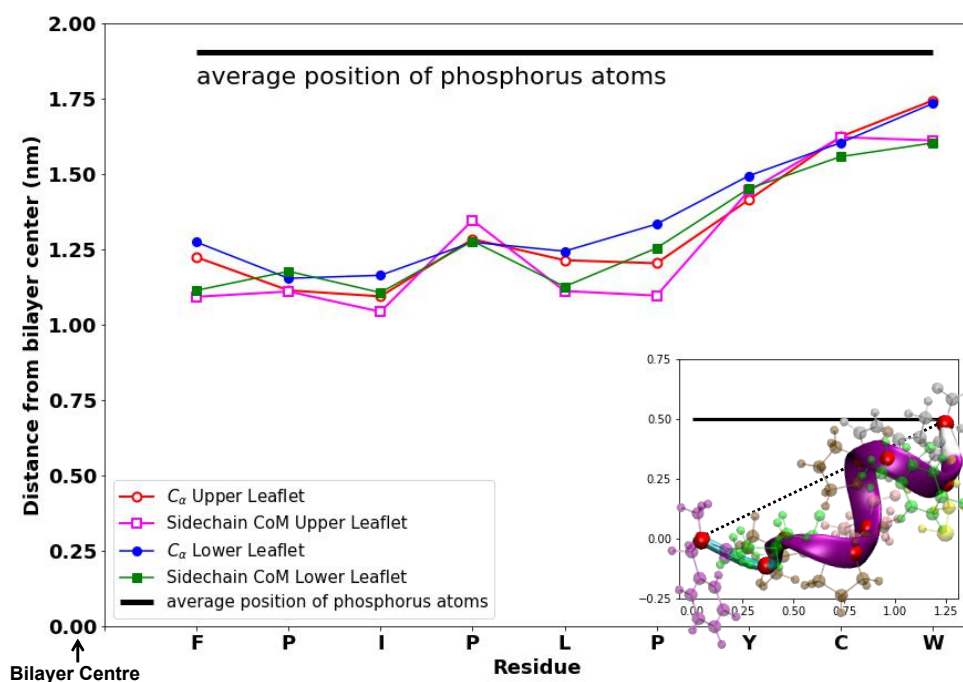


Figure 3.13 – Average distance of C_{α} in the upper (open red circle) and lower (closed blue circle), center of mass of side chains of C_{α} in the upper (open magenta square) and lower (closed green square) leaflet and the average position of phosphorus atoms from the bilayer center. Here zero on the y axis indicates the bilayer center. The peptide initially slopes into the bilayer and then lies almost parallel to the bilayer plane. The inset shows the orientation of a peptide in the bilayer. The red beads indicate the C_{α} of each residue. The C_{α} end-to-end distance of the peptide was found to be 1.35 nm.

The position of C_{α} indicates the position of the backbone at that residue. Residues with larger sidechains, like tryptophan (W), will have centres of mass substantially further from the corresponding C_{α} position, than smaller residues like proline (P). This difference is evident from the figure.

The tryptophan residues stay close to the bilayer surface. The peptide slopes into the

bilayer and last few residues are almost horizontal. This orientation of the peptide has significance as the peptide being aligned horizontal to the lipid bilayer occupies space near the headgroup of ends of lipid acyl chains which perturbs lipid packing. This reduces the average acyl chain orientational order of the lipid bilayer. The peptide orientation in the bilayer is showed as an inset in the figure.

In order to obtain information about more local interactions of peptides with the bilayer, we also calculated the average shortest distance from residue $C_{\alpha}s$ to the nearest phosphorus atoms. Details can be found in **Appendix B.6**. These averages over the time range analysed are shown in **Figure 3.14**.

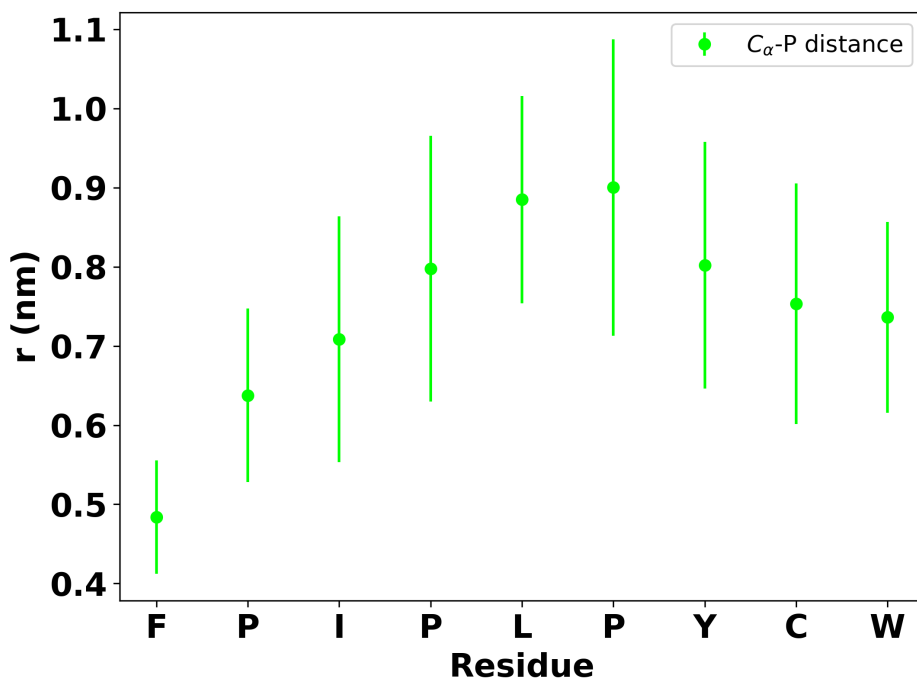


Figure 3.14 – Average shortest distance of C_{α} s of peptide residues from a P atom in the lipid bilayer. The residue phenylalanine at one end is closer to the phosphorus atoms compared to the tryptophan at the other end. Standard deviation is used for plotting the error bars.

We can see that the phenylalanine (F) at the N terminal end of the peptide is closer to its nearest phosphorus atom compared to the tryptophan (W) residue at the end. This distance can be compared to the average depth of the residues in the bilayer from the average phosphorus distance from **Figure 3.13**, according to which, for F, the average distance of C_{α} from the average level of phosphorus atoms is about 0.65 nm (1.9 nm-1.25nm), while that for W is about 0.15 nm (1.9 nm-1.75nm). The average shortest distance of F from the P atoms (0.49 nm) is smaller than the average depth of the C_{α} of the phenylalanine residues from the average P atom depth (0.65 nm). Since F is at the N-terminus of the protein, it's

backbone amide group carries a positive charge, and hence the residue must be pulling the phosphorus atoms and some water towards it, causing a dip on the leaflet surface. In the case of W, the average shortest distance from phosphorus atoms (0.75 nm) is bigger compared to the depth of the C_{α} of the residue (0.15 nm) from the P atoms. Hence, W must be pushing the phosphorus atoms away, presumably within the plane of headgroups. On one end (the W end), the peptide is pushing away the lipids, while on the other end (F end) the peptide is pulling the lipids towards it. This behavior might be pertinent to the lipid organization disruption that may be an aspect of SP-B function [146].

Chapter 4

Discussion

Surfactant replacement therapy using bovine or porcine lung extracts is being widely adopted and has shown improvements in the treatment of NRDS [147]. It is also used for acute lung injury (ALI) and ARDS [148]. The COVID-19 pandemic, which began in 2019, has resulted in widespread death around the world [149–151]. The majority of patients admitted to the hospitals are diagnosed with pneumonia, and many develop ARDS [152]. Many COVID clinical trials are evaluating surfactant replacement therapy for the treatment of ARDS [153–155]. The motive of lung surfactant studies is to reduce the use of surfactants derived from animals for surfactant therapies and to contribute to the development of fully functional synthetic surfactants. A proper understanding of the interactions of different components in lung surfactants is necessary for this purpose.

In this study, we explore how the insertion sequence of surfactant protein B (SP-B) interacts with models of lipid components. Hydrophobic lung surfactant protein, SP-B, plays a major role in decreasing the effort of breathing by lowering the surface tension, at the alveolar air-liquid interface, to a minimum [156]. SP-B, along with SP-C, is thought

to be involved in the replacement of the spent surfactant with recycled surface-active material from bilayer reservoirs [157]. For the surface-active material to be transferred from the bilayer reservoirs to the interface, there has to be some reorganization of the bilayer taking place. Many studies have been conducted over the years to investigate the effect of hydrophobic surfactant protein on the lipid bilayer [85–90, 158]. These studies were aimed at contributing to understanding of the interaction between SP-B and lung surfactant lipids, that facilitates the function of SP-B. A study by Sharifahmadian et al. [85] using different fragments of SP-B showed that a SP-B fragment with the insertion sequence showed more effect on the ^2H NMR splittings of deuterated lipid components, and thus more effect on acyl chain order of the lipid bilayer (composed of a combination of zwitterionic and anionic lipid) than that of the SP-B fragment without the insertion sequence. Farver et al. [86] in a different study found that low concentrations of SP-B fragment 1-25 (SP-B_{1–25}) had significant effect on the ^2H NMR spectra and hence on the order parameter profile of deuterated lipids in the model lipid mixtures. In previous studies involving ^2H NMR experiments with SP-B_{8–25} [87] and both SP-B_{59–80} [88] and SP-B_{63–78} [89] (the SP-B C-terminus), the peptides were found to have little effect on lipid chain order in the model bilayers. These apparent differences between the effects of SP-B with and without the insertion sequence motivated us to look at the insertion sequence more closely, and at interactions with lipids that might contribute to a possible role in bilayer reorganization.

To explore the interaction between SP-B insertion sequence that might contribute to the bilayer reorganization of the lipid bilayer that is expected to be required for the re-spreading of the surfactant materials, we first used solid-state ^2H NMR for investigating the effect of the SP-B fragment, SP-B_{1–9} on model lipid bilayer composed of a combination of zwitterionic and anionic lipid in a 7:3 ratio: DPPC-*d*₆₂/POPG (7:3). We examined

the effect of SP-B₁₋₉ concentration on the model lipid bilayers, primarily focussing on the acyl chain orientational order. Secondly, we used the GROMACS molecular dynamics simulation package to explore the conformation, location, and the interaction of the peptide in a simulated lipid bilayer composed of DPPC and POPG in a 7:3 ratio.

The first moment and order parameter profiles obtained (**Figure 2.13** and **2.15** respectively) from the ²H NMR experiments did not show a significant effect on DPPC-*d*₆₂ acyl chain order at higher concentrations of peptide compared to a sample with only lipids.

Figure 4.1 shows a superposition of the dePaked spectra first presented in **Figure 2.14**.

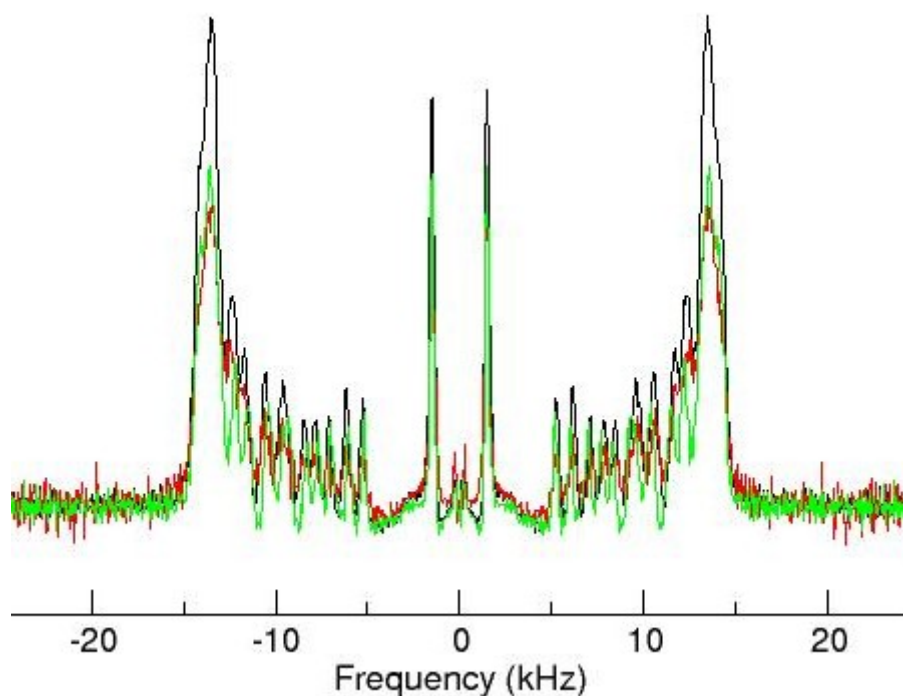


Figure 4.1 – Overlap of dePaked spectra of the samples (Green) DPPC-*d*₆₂/POPG, (Red) DPPC-*d*₆₂/POPG + SP-B₁₋₉ (P:L 0.066) and (Black) DPPC-*d*₆₂/POPG + SP-B₁₋₉ (P:L 0.098) at $T = 40$ °C. The doublets almost align for the three samples, indicating that there is not much difference in the quadrupolar splitting and thereby the acyl chain orientational order.

The comparison at $T = 40$ °C clearly shows that the peptide is not inducing any effect on the acyl chain orientational order. This may indicate that the peptide interacts with the bilayer in a way that does not significantly perturb lipid orientational order or it may indicate that the peptide is not uniformly distributed through the bilayer. Peptide aggregation might result in a peptide lipid interaction being independent of concentration. Given these possibilities it is difficult to draw any conclusion from the NMR experiments. Separating these possibilities is something that might require further investigation, possibly using a modified peptide with a lesser tendency to aggregate.

The order parameter profile comparison from the GROMACS molecular dynamic simulations of model lipid bilayers with and without the insertion sequence peptide present, shown in **Figure 3.5**, suggests a slightly different interpretation. We found that the lipid acyl chain orientational order in the simulated bilayer decreases slightly with increasing peptide concentration. The peptide-to-lipid ratios of the two peptide-containing samples used for ^2H NMR studies were about two times (0.066) and three times (0.098) the peptide-to-lipid ratio of the multiple peptide system (0.031) in the simulations. Hence as noted above the finding of a peptide-concentration-dependent effect on lipid acyl chain order in simulations and the absence of this effect in the experiment raises the possibility of peptide aggregation in the NMR samples which needs to be investigated further.

From the simulations, we also looked at the conformation and location of the peptide in the bilayer. The helicity plots in **Figures 3.9, 3.10, and 3.11** were obtained from the secondary structure calculated using the STRIDE plugin of VMD. From these calculations, we found that the residues at peptide positions 5, 6, and 7 (i.e. proline, leucine, and tyrosine) have the highest average probability of being part of a helical region, about 45% compared to other residues. The first two residues (F and P) and the last residue (W) were

found to be consistently zero over the time range analyzed. The residues L, P and Y at positions 5, 6, and 7 respectively thus have the potential for being in a helical structure. Helical peptide regions that do not extend to the bilayer center might have some potential to disrupt the bilayer more than flexible non-helical sections since they can result in lipid chains being excluded from a compact volume at a specific depth in the bilayer. The need for lipid chains to pack differently at depths in the bilayer with and without peptide present could affect the acyl chain orientational order of the membrane. In a different simulation study of full length SP-B, by M.H. Khatami et al. [145], the helicity calculation for the open-in configuration of SP-B, done using STRIDE, also showed that residues L, P and Y at positions 5, 6 and 7 respectively tended to be helical even though this study was done with a different force field.

The plots of the average C_{α} depth and the average shortest distance from a C_{α} to the nearest neighboring phosphorus atoms can tell us about the orientation of the peptide and this can give insight into how it might contribute to disrupting the bilayer. The average end-to-end distance of the peptide was found to be 1.35 nm, from which the angle at which the peptide slopes into the bilayer was calculated. The peptide slopes into the bilayer at an angle of about 22° measured from the bilayer surface. Instead of going vertically down into the bilayer, the peptide slopes in and takes an almost horizontal orientation in the bilayer. This behavior may, in part, reflect positive charge on the phenylalanine at the N-terminus. A vertical orientation of the peptide in the bilayer might be expected to perturb the bilayer less, but a more horizontal orientation can take up space near the headgroup ends of the acyl chains and increase lipid separation. This can cause a lowering of the acyl chain order. It is also noticeable from **Figures 3.12** and **3.13** that the peptide is lying in the bilayer near the headgroups, and not penetrating closer to the bilayer center. The lowering of the lipid

acyl chain order near to the bilayer surface by the insertion sequence might contribute to the role of SP-B in the recruitment and respreading of the surfactant layer as some reorganization of the lipid bilayer has to happen for surface active material to be transferred from surfactant reservoirs to the interface.

Many previous works have done comparisons of experimental order parameter profiles with simulation order parameter profiles. The assignment scheme introduced in Petrache et al [99] is the best scheme available at the moment assigning order parameters to the *sn*-1 and *sn*-2 chains of a disaturated phospholipid like DPPC-*d*₆₂. A few studies have compared their experimental order parameter profiles obtained using the assignment scheme from Petrache et al. to simulation results, and they are in very good agreement [159–162]. In our work, we have used the CHARMM36 force field and TIP3P water model for our simulation and used a binary lipid mixture for the model lipid bilayer. The comparison of order parameter profiles from experiment and simulation at temperatures 319 K (46° C) and 323 K (50° C) (**Figure 3.6**) showed good agreement. The comparison at the lower temperatures (310 K/37 °C) is also very close, given that the simulation at that temperature was still not quite equilibrated.

Chapter 5

Conclusion

In summary, solid-state deuterium NMR spectroscopy and GROMACS molecular dynamics simulations have been employed for investigating how high concentrations of the insertion sequence of the lung surfactant protein B perturbs the dynamics and phase behavior of model lipid bilayer comprising a mixture of zwitterionic (DPPC) and anionic (POPG) lipids in a 7:3 ratio. From the ^2H NMR experiments, the peptide does not seem to perturb the acyl chain order of the lipid bilayer, while the order parameter profiles from the molecular dynamics simulations showed a lowering of the acyl chain order with high peptide concentrations. Peptide aggregation in the ^2H NMR samples could be the reason for the lack of effect in the experiments, which needs to be explored further in the future.

Average conformation of the peptide showed the helicity probability of the three amino acids residues at peptide positions 5, 6, 7 to be about 45%. Since helical regions on a mostly horizontal peptide might disrupt the bilayer more as they take up space non-uniformly as a function of depth in the bilayer, the observation that a portion of the peptide has a tendency to form small helical structures might account for its ability to perturb bilayer orientational

order. The average location and orientation of the peptide in the bilayer showed that the peptide stays closer to the bilayer surface, taking up a nearly horizontal orientation in the lipid bilayer. This observation indicates that the insertion sequence does not penetrate deep into the bilayer, but instead, stays and perturbs the bilayer near the bilayer surface. This behavior of the insertion sequence may be important to the role of full-length SP-B in the adsorption and respreading of the phospholipids from the surfactant reservoir, necessary for the surface tension reduction at the alveolar air-liquid interface. Experimental and simulated order parameter profiles were found to be in good agreement.

The absence of peptide-induced bilayer perturbation shown by the ^2H NMR results suggests the possibility of peptide aggregation in the NMR samples. This is evident from the remarkably close ^2H NMR order parameter profiles of samples with only lipids and the samples with two different concentrations of peptide. Aggregation might have limited the ability of the peptide to perturb a significant fraction of lipids in the NMR sample model lipid bilayers. On the other hand, the simulation results provide some encouragement to further explore the role of the insertion sequence in bilayer reorganization. The lowering of the acyl chain orientation order with increasing peptide concentration indicates that the insertion sequence does have a concentration-dependent effect on the lipid bilayer, and hence might need to be retained in synthetic surfactants.

Bibliography

- [1] L. Knudsen and M. Ochs. The Micromechanics of Lung Alveoli: Structure and Function of Surfactant and Tissue Components. *Histochemistry and Cell Biology*, 150(6):661–676, 2018.
- [2] M. Haddad and S. Sharma. *Physiology, Lung [Updated 2021 Jul 22]*. In: StatPearls [Internet]. Treasure Island (FL): StatPearls Publishing;2021 Jan-. Available from: <https://www.ncbi.nlm.nih.gov/books/NBK545177/>.
- [3] R. H. Notter. *Lung Surfactants: Basic Science and Clinical Applications*. CRC Press, 2000.
- [4] S. V. Khanorkar. *Insights in Physiology*. JP Medical Ltd, 2011.
- [5] J. A. Whitsett, S. E. Wert, and T. E. Weaver. Alveolar Surfactant Homeostasis and the Pathogenesis of Pulmonary Disease. *Annual Review of Medicine*, 61:105–119, 2010.
- [6] W. Bernhard. Lung surfactant: Function and Composition in the Context of Development and Respiratory Physiology. *Annals of Anatomy-Anatomischer Anzeiger*, 208:146–150, 2016.

- [7] M. Hiles, A.-M. Culpan, C. Watts, T. Munyombwe, and S. Wolstenhulme. Neonatal Respiratory Distress Syndrome: Chest X-Ray or Lung Ultrasound? A Systematic Review. *Ultrasound*, 25(2):80–91, 2017.
- [8] M. Filoche, C.-F. Tai, and J. B. Grotberg. Three-Dimensional Model of Surfactant Replacement Therapy. *Proceedings of the National Academy of Sciences*, 112(30):9287–9292, 2015.
- [9] S.-P. Luh and C.-H. Chiang. Acute Lung Injury/Acute Respiratory Distress Syndrome (ALI/ARDS): the Mechanism, Present Strategies and Future Perspectives of Therapies. *Journal of Zhejiang University Science B*, 8(1):60–69, 2007.
- [10] A. Kornecki and R. N. Singh. Acute Respiratory Distress Syndrome. In *Kendig's Disorders of the Respiratory Tract in Children*, pages 606–614. Elsevier, 2019.
- [11] B. Robertson and H. L. Halliday. Principles of Surfactant Replacement. *Biochimica et Biophysica Acta (BBA)-Molecular Basis of Disease*, 1408(2-3):346–361, 1998.
- [12] E. Parra and J. Pérez-Gil. Composition, Structure and Mechanical Properties Define Performance of Pulmonary Surfactant Membranes and Films. *Chemistry and Physics of Lipids*, 185:153–175, 2015.
- [13] J. Goerke. Pulmonary Surfactant: Functions and Molecular Composition. *Biochimica et Biophysica Acta (BBA)-Molecular Basis of Disease*, 1408(2-3):79–89, 1998.
- [14] S. Matalon, J.M. Hickman-Davis, and J.R. Wright. SURFACTANT— Surfactant Protein A (SP-A). 2006.

- [15] T. E. Weaver, W. M. Hull, G. F. Ross, and J. A. Whitsett. Intracellular and Oligomeric Forms of Surfactant-Associated Apolipoproteins(s) A in the Rat. *Biochimica et Biophysica Acta (BBA)-Protein Structure and Molecular Enzymology*, 827(3):260–267, 1985.
- [16] U. Kishore, T. J. Greenhough, P. Waters, A. K. Shrive, R. Ghai, M. F. Kamran, A. López Bernal, K. B. M. Reid, T. Madan, and T. Chakraborty. Surfactant Proteins SP-A and SP-D: Structure, Function and Receptors. *Molecular Immunology*, 43(9):1293–1315, 2006.
- [17] Y. Suzuki, Y. Fujita, and K. Kogishi. Reconstitution of Tubular Myelin from Synthetic Lipids and Proteins Associated with Pig Pulmonary Surfactant. *American Review of Respiratory Disease*, 140(1):75–81, 1989.
- [18] J. C. Clark, S. E. Wert, C. J. Bachurski, M. T. Stahlman, B. R. Stripp, T. E. Weaver, and J. A. Whitsett. Targeted Disruption of the Surfactant Protein B Gene Disrupts Surfactant Homeostasis, Causing Respiratory Failure in Newborn Mice. *Proceedings of the National Academy of Sciences*, 92(17):7794–7798, 1995.
- [19] T. R. Korfhagen, M. D. Bruno, G. F. Ross, K. M. Huelsman, M. Ikegami, A. H. Jobe, S. E. Wert, B. R. Stripp, R. E. Morris, S. W. Glasser, C. J. Bachurski, H. S. Iwamoto, and J. A. Whitsett. Altered surfactant function and structure in sp-a gene targeted mice. *Proceedings of the National Academy of Sciences*, 93(18):9594–9599, 1996.
- [20] S. Hawgood, B. J. Benson, J. Schilling, D. Damm, J. A. Clements, and R. T. White. Nucleotide and Amino Acid Sequences of Pulmonary Surfactant Protein SP 18 and

Evidence for Cooperation Between SP 18 and SP 28-36 in Surfactant Lipid Adsorption. *Proceedings of the National Academy of Sciences*, 84(1):66–70, 1987.

- [21] A. R. Venkitaraman, S. B. Hall, J. A. Whitsett, and R. H. Notter. Enhancement of Biophysical Activity of Lung Surfactant Extracts and Phospholipid-Apoprotein Mixtures by Surfactant Protein A. *Chemistry and Physics of Lipids*, 56(2-3):185–193, 1990.
- [22] A. M. Cockshutt, J. Weitz, and F. Possmayer. Pulmonary Surfactant-Associated Protein A Enhances the Surface Activity of Lipid Extract Surfactant and Reverses Inhibition by Blood Proteins In-Vitro. *Biochemistry*, 29(36):8424–8429, 1990.
- [23] K. O. Yukitake, C. L. Brown, M. A. Schlueter, J. A. Clements, and S. Hawgood. Surfactant Apoprotein A Modifies the Inhibitory Effect of Plasma Proteins on Surfactant Activity In-Vivo. *Pediatric research*, 37(1):21–25, 1995.
- [24] D. S. Strayer, E. Herting, B. Sun, and B. Robertson. Antibody to Surfactant Protein A Increases Sensitivity of Pulmonary Surfactant to Inactivation by Fibrinogen In-Vivo. *American Journal of Respiratory and Critical Care Medicine*, 153(3):1116–1122, 1996.
- [25] A. D. Horowitz, B. Moussavian, E. D. Han, J. E. Baatz, and J. A. Whitsett. Distinct Effects of SP-A and SP-B on Endocytosis of SP-C by Pulmonary Epithelial Cells. *American Journal of Physiology-Lung Cellular and Molecular Physiology*, 273(1):L159–L171, 1997.
- [26] Y. Kuroki, M. Shiratori, Y. Ogasawara, A. Hattori, W. Tsunazawa, T. Honma, and T. Akino. Interaction of Phospholipid Liposomes with Plasma Membrane Isolated

from Alveolar Type II Cells: Effect of Pulmonary Surfactant Protein A. *Biochimica et Biophysica Acta (BBA)-Biomembranes*, 1281(1):53–59, 1996.

- [27] L. G. Dobbs, J. R. Wright, S. Hawgood, R. Gonzalez, K. Venstrom, and J. Nellenbogen. Pulmonary Surfactant and its Components Inhibit Secretion of Phosphatidylcholine from Cultured Rat Alveolar Type II Cells. *Proceedings of the National Academy of Sciences*, 84(4):1010–1014, 1987.
- [28] R. B. Sim, H. Clark, M. R. Hajela, and K. R. Mayilyan. Collectins and Host Defence. In *Innate Immunity to Pulmonary Infection. Novartis Foundation Symposium*, volume 279, pages 170–186, 2007.
- [29] R. Arroyo, A. Martin-Gonzalez, M. Echaide, A. Jain, W. H. Brondyk, J. Rosenbaum, F. Moreno-Herrero, and J. Perez-Gil. Supramolecular Assembly of Human Pulmonary Surfactant Protein SP-D. *Journal of Molecular Biology*, 430(10):1495–1509, 2018.
- [30] S. Zaltash, M. Palmblad, T. Curstedt, J. Johansson, and B. Persson. Pulmonary Surfactant Protein B: A Structural Model and a Functional Analogue. *Biochimica et Biophysica Acta (BBA)-Biomembranes*, 1466(1-2):179–186, 2000.
- [31] J. Johansson. Structure and Properties of Surfactant Protein C. *Biochimica et Biophysica Acta (BBA) - Molecular Basis of Disease*, 1408(2):161–172, 1998.
- [32] J. Johansson, T. Szyperski, T. Curstedt, and K. Wuethrich. The NMR Structure of the Pulmonary Surfactant-Associated Polypeptide SP-C in an Apolar Solvent Contains a Valyl-Rich. α -Helix. *Biochemistry*, 33(19):6015–6023, 1994.

- [33] T. Curstedt, J. Johansson, P. Persson, A. Eklund, B. Robertson, B. Löwenadler, and H. Jörnvall. Hydrophobic Surfactant-Associated Polypeptides: SP-C is a Lipopeptide with Two Palmitoylated Cysteine Residues, whereas SP-B Lacks Covalently Linked Fatty Acyl Groups. *Proceedings of the National Academy of Sciences*, 87(8):2985–2989, 1990.
- [34] A. Gonzalez-Horta, D. Andreu, M. R. Morrow, and J. Perez-Gil. Effects of Palmitoylation on Dynamics and Phospholipid-Bilayer-Perturbing Properties of the N-Terminal Segment of Pulmonary Surfactant Protein SP-C as Shown by ^2H -NMR. *Biophysical Journal*, 95(5):2308–2317, 2008.
- [35] N. Roldan, E. Goormaghtigh, J. Pérez-Gil, and B. Garcia-Alvarez. Palmitoylation as a Key Factor to Modulate SP-C-Lipid Interactions in Lung Surfactant Membrane Multilayers. *Biochimica et Biophysica Acta (BBA)-Biomembranes*, 1848(1):184–191, 2015.
- [36] M. A. Oosterlaken-Dijksterhuis, H. P. Haagsman, L. M. G. Van Golde, and R. A. Demel. Characterization of Lipid Insertion into Monomolecular Layers Mediated by Lung Surfactant Proteins SP-B and SP-C. *Biochemistry*, 30(45):10965–10971, 1991.
- [37] S. G. Taneva and K. M. W. Keough. Dynamic Surface Properties of Pulmonary Surfactant Proteins SP-B and SP-C and Their Mixtures with Dipalmitoylphosphatidylcholine. *Biochemistry*, 33(49):14660–14670, 1994.

- [38] J. Pérez-Gil. Structure of Pulmonary Surfactant Membranes and Films: The Role of Proteins and Lipid-Protein Interactions. *Biochimica et Biophysica acta (BBA)-Biomembranes*, 1778(7-8):1676–1695, 2008.
- [39] J. C. Clark, S. E. Wert, C. J. Bachurski, M. T. Stahlman, B. R. Stripp, T. E. Weaver, and J. A. Whitsett. Targeted Disruption of the Surfactant Protein B Gene Disrupts Surfactant Homeostasis, Causing Respiratory Failure in Newborn Mice. *Proceedings of the National Academy of Sciences*, 92(17):7794–7798, 1995.
- [40] L. M. Noguee, D. E. DeMello, L. P. Dehner, and H. R. Colten. Deficiency of Pulmonary Surfactant Protein B in Congenital Alveolar Proteinosis. *New England Journal of Medicine*, 328(6):406–410, 1993.
- [41] E. Parra, A. Alcaraz, A. Cruz, V. M. Aguilera, and J. Pérez-Gil. Hydrophobic Pulmonary Surfactant Proteins SP-B and SP-C Induce Pore Formation in Planar Lipid Membranes: Evidence for Proteolipid Pores. *Biophysical Journal*, 104(1):146–155, 2013.
- [42] J. C. Clark, S. E. Wert, C. J. Bachurski, M. T. Stahlman, B. R. Stripp, T. E. Weaver, and J. A. Whitsett. Targeted Disruption of the Surfactant Protein B Gene Disrupts Surfactant Homeostasis, Causing Respiratory Failure in Newborn Mice. *Proceedings of the National Academy of Sciences*, 92(17):7794–7798, 1995.
- [43] C. D. Foster, P. X. Zhang, L. W. Gonzales, and S. H. Guttentag. In Vitro Surfactant Protein B Deficiency Inhibits Lamellar Body Formation. *American Journal of Respiratory Cell and Molecular Biology*, 29(2):259–266, 2003.

- [44] S. Krol, M. Ross, M. Sieber, S. Künneke, H.-J. Galla, and A. Janshoff. Formation of Three-Dimensional Protein-Lipid Aggregates in Monolayer Films Induced by Surfactant Protein B. *Biophysical Journal*, 79(2):904–918, 2000.
- [45] K. Rodriguez-Capote, K. Nag, S. Schürch, and F. Possmayer. Surfactant Protein Interactions with Neutral and Acidic Phospholipid Films. *American Journal of Physiology-Lung Cellular and Molecular Physiology*, 281(1):L231–L242, 2001.
- [46] D. Schürch, O. L. Ospina, A. Cruz, and J. Pérez-Gil. Combined and Independent Action of Proteins SP-B and SP-C in the Surface Behavior and Mechanical Stability of Pulmonary Surfactant Films. *Biophysical Journal*, 99(10):3290–3299, 2010.
- [47] M. A. Ryan, X. Qi, A. G. Serrano, M. Ikegami, J. Perez-Gil, J. Johansson, and T. E. Weaver. Mapping and Analysis of the Lytic and Fusogenic Domains of Surfactant Protein B. *Biochemistry*, 44(3):861–872, 2005.
- [48] J. Johansson, T. Curstedt, and H. Jörnvall. Surfactant Protein B: Disulfide Bridges, Structural Properties and Kringle Similarities. *Biochemistry*, 30(28):6917–6921, 1991.
- [49] M. Andersson, T. Curstedt, H. Jörnvall, and J. Johansson. An Amphipathic Helical Motif Common to Tumourolytic Polypeptide NK-Lysin and Pulmonary Surfactant Polypeptide SP-B. *FEBS Letters*, 362(3):328–332, 1995.
- [50] J. Pérez-Gil, A. Cruz, and C. Casals. Solubility of Hydrophobic Surfactant Proteins in Organic Solvent/Water Mixtures. Structural Studies on SP-B and SP-C in Aqueous Organic Solvents and Lipids. *Biochimica et Biophysica Acta (BBA)-Lipids and Lipid Metabolism*, 1168(3):261–270, 1993.

- [51] G. Vandenbussche, A. Clercx, M. Clercx, T. Curstedt, J. Johansson, H. Jörnvall, and J. M. Ruyschaert. Secondary Structure and Orientation of the Surfactant Protein SP-B in a Lipid Environment. A Fourier Transform Infrared Spectroscopy Study. *Biochemistry*, 31(38):9169–9176, 1992.
- [52] B. Olmeda, B. García-Álvarez, and J. Pérez-Gil. Structure-Function Correlations of Pulmonary Surfactant Protein SP-B and the Saposin-Like Family of Proteins. *European Biophysics Journal*, 42(2-3):209–222, 2013.
- [53] F. J. Walther, A. J. Waring, J. M. Hernandez-Juviel, L. M. Gordon, Zhengdong Wang, Chun-Ling Jung, Piotr Ruchala, Andrew P Clark, W. M. Smith, S. Sharma, and R. H. Notter. Critical Structural and Functional Roles for the N-Terminal Insertion Sequence in Surfactant Protein B Analogs. *PLoS One*, 5(1):e8672, 2010.
- [54] S. L. Frey, L. Pocivavsek, A. J. Waring, F. J. Walther, J. M. Hernandez-Juviel, P. Ruchala, and K. Y. C. Lee. Functional Importance of the NH₂-Terminal Insertion Sequence of Lung Surfactant Protein B. *American Journal of Physiology-Lung Cellular and Molecular Physiology*, 298(3):L335–L347, 2010.
- [55] A. G. Serrano, A. Cruz, K. Rodríguez-Capote, F. Possmayer, and J. Pérez-Gil. Intrinsic Structural and Functional Determinants within the Amino Acid Sequence of Mature Pulmonary Surfactant Protein SP-B. *Biochemistry*, 44(1):417–430, 2005.
- [56] W. C. Wimley and S. H. White. Experimentally Determined Hydrophobicity Scale for Proteins at Membrane Interfaces. *Nature Structural Biology*, 3(10):842–848, 1996.

- [57] A. Cruz, C. Casals, I. Plasencia, D. Marsh, and J. Perez-Gil. Depth Profiles of Pulmonary Surfactant Protein B in Phosphatidylcholine Bilayers, Studied by Fluorescence and Electron Spin Resonance Spectroscopy. *Biochemistry*, 37(26):9488–9496, 1998.
- [58] Y. Wang, K. M. K. Rao, and E. Demchuk. Topographical Organization of The N-Terminal Segment of Lung Pulmonary Surfactant Protein B (SP-B1-25) in Phospholipid Bilayers. *Biochemistry*, 42(14):4015–4027, 2003.
- [59] E. Parra and J. Pérez-Gil. Composition, Structure and Mechanical Properties Define Performance of Pulmonary Surfactant Membranes and Films. *Chemistry and Physics of Lipids*, 185:153–175, 2015.
- [60] S.-H. Yu and F. Possmayer. Dipalmitoylphosphatidylcholine and Cholesterol in Monolayers Spread from Adsorbed Films of Pulmonary Surfactant. *Journal of Lipid Research*, 42(9):1421–1429, 2001.
- [61] D. Y. Takamoto, M. M. Lipp, A. Von Nahmen, K. Y. C. Lee, A. J. Waring, and J. A. Zasadzinski. Interaction of Lung Surfactant Proteins with Anionic Phospholipids. *Biophysical Journal*, 81(1):153–169, 2001.
- [62] S. Leekumjorn and A. K. Sum. Molecular Studies of the Gel to Liquid-Crystalline Phase Transition for Fully Hydrated DPPC and DPPE Bilayers. *Biochimica et Biophysica Acta (BBA)-Biomembranes*, 1768(2):354–365, 2007.
- [63] E. J. A. Veldhuizen, J. J. Batenburg, L. M. G. van Golde, and H. P. Haagsman. The Role of Surfactant Proteins in DPPC Enrichment of Surface Films. *Biophysical Journal*, 79(6):3164–3171, 2000.

- [64] R. V. Diemel, M. M. E. Snel, A. J. Waring, F. J. Walther, L. M. G. van Golde, G. Putz, H. P. Haagsman, and J. J. Batenburg. Multilayer Formation upon Compression of Surfactant Monolayers Depends on Protein Concentration as well as Lipid Composition: An Atomic Force Microscopy Study. *Journal of Biological Chemistry*, 277(24):21179–21188, 2002.
- [65] G. Mao, J. Desai, C. R. Flach, and R. Mendelsohn. Structural Characterization of the Monolayer- Multilayer Transition in a Pulmonary Surfactant Model: IR Studies of Films Transferred at Continuously Varying Surface Pressures. *Langmuir*, 24(5):2025–2034, 2008.
- [66] B. Pastrana-Rios, C. R. Flach, J. W. Brauner, A. J. Mautone, and R. Mendelsohn. A Direct Test of the “Squeeze-Out” Hypothesis of Lung Surfactant Function. External Reflection FTIR at the Air/Water Interface. *Biochemistry*, 33(17):5121–5127, 1994.
- [67] H. Bachofen, U. Gerber, P. Gehr, M. Amrein, and S. Schürch. Structures of Pulmonary Surfactant Films Adsorbed to an Air-Liquid Interface In-vitro. *Biochimica et Biophysica Acta (BBA)-Biomembranes*, 1720(1-2):59–72, 2005.
- [68] D. Follows, F. Tiberg, R. K. Thomas, and M. Larsson. Multilayers at the Surface of Solutions of Exogenous Lung Surfactant: Direct Observation by Neutron Reflection. *Biochimica et Biophysica Acta (BBA)-Biomembranes*, 1768(2):228–235, 2007.
- [69] S. Schürch, R. Qanbar, H. Bachofen, and F. Possmayer. The Surface-Associated Surfactant Reservoir in the Alveolar Lining. *Neonatology*, 67(Suppl. 1):61–76, 1995.

- [70] J. Pérez-Gil, K. Nag, S. Taneva, and K. M. Keough. Pulmonary Surfactant Protein SP-C Causes Packing Rearrangements of Dipalmitoylphosphatidylcholine in Spread Monolayers. *Biophysical Journal*, 63(1):197–204, 1992.
- [71] A. von Nahmen, A. Post, H.-J. Galla, and M. Sieber. The Phase Behavior of Lipid Monolayers Containing Pulmonary Surfactant Protein C Studied by Fluorescence Light Microscopy. *European Biophysics Journal*, 26(5):359–369, 1997.
- [72] A. Von Nahmen, M. Schenk, M. Sieber, and M. Amrein. The Structure of a Model Pulmonary Surfactant as Revealed by Scanning Force Microscopy. *Biophysical Journal*, 72(1):463–469, 1997.
- [73] E. J. Cabré, J. Malmström, D. Sutherland, J. Perez-Gil, and D. E. Otzen. Surfactant Protein SP-B Strongly Modifies Surface Collapse of Phospholipid Vesicles: Insights from a Quartz Crystal Microbalance with Dissipation. *Biophysical Journal*, 97(3):768–776, 2009.
- [74] A. Cruz, C. Casals, K. M. W. Keough, and J. Pérez-Gil. Different Modes of Interaction of Pulmonary Surfactant Protein SP-B in Phosphatidylcholine Bilayers. *Biochemical Journal*, 327(1):133–138, 1997.
- [75] R. Chang, S. Nir, and F. R. Poulain. Analysis of Binding and Membrane Destabilization of Phospholipid Membranes by Surfactant Apoprotein B. *Biochimica et Biophysica Acta (BBA)-Biomembranes*, 1371(2):254–264, 1998.
- [76] A. Cruz, L.-A. Worthman, A. G. Serrano, C. Casals, K. M. W. Keough, and J. Perez-Gil. Microstructure and Dynamic Surface Properties of Surfactant Protein SP-

- B/Dipalmitoylphosphatidylcholine Interfacial Films Spread from Lipid-Protein Bilayers. *European Biophysics Journal*, 29(3):204–213, 2000.
- [77] X. Bi, C. R. Flach, J. Pérez-Gil, I. Plasencia, D. Andreu, E. Oliveira, and R. Mendelsohn. Secondary Structure and Lipid Interactions of the N-Terminal Segment of Pulmonary Surfactant SP-C in Langmuir Films: IR Reflection-Absorption Spectroscopy and Surface Pressure Studies. *Biochemistry*, 41(26):8385–8395, 2002.
- [78] I. P. Artemenko, D. Zhao, D. B. Hales, K. H. Hales, and C. R. Jefcoate. Mitochondrial Processing of Newly Synthesized Steroidogenic Acute Regulatory Protein (StAR), But Not Total StAR, Mediates Cholesterol Transfer to Cytochrome P450 Side Chain Cleavage Enzyme in Adrenal Cells. *Journal of Biological Chemistry*, 276(49):46583–46596, 2001.
- [79] A. Almlén, G. Stichtenoth, B. Linderholm, M. Haegerstrand-Bjorkman, B. Robertsson, J. Johansson, and T. Curstedt. Surfactant Proteins B and C are Both Necessary for Alveolar Stability at End Expiration in Premature Rabbits with Respiratory Distress Syndrome. *Journal of Applied Physiology*, 104(4):1101–1108, 2008.
- [80] J. Pérez-Gil. Structure of Pulmonary Surfactant Membranes and Films: The Role of Proteins and Lipid-Protein Interactions. *Biochimica et Biophysica Acta (BBA)-Biomembranes*, 1778(7-8):1676–1695, 2008.
- [81] A. Chakraborty, E. Hui, A. J. Waring, and P. Dhar. Combined Effect of Synthetic Protein, Mini-B, and Cholesterol on a Model Lung Surfactant Mixture at the Air-Water Interface. *Biochimica et Biophysica Acta (BBA)-Biomembranes*, 1858(4):904–912, 2016.

- [82] O. Braide-Moncoeur, N. T. Tran, and J. R. Long. Peptide-Based Synthetic Pulmonary Surfactant for the Treatment of Respiratory Distress Disorders. *Current Opinion in Chemical Biology*, 32:22–28, 2016.
- [83] A. M. Czyzewski, L. M. McCaig, M. T. Dohm, L. A. Broering, L.-J. Yao, N. J. Brown, M. K. Didwania, J. S. Lin, J. F. Lewis, R. Veldhuizen, and A. E. Barron. Effective In Vivo Treatment of Acute Lung Injury with Helical, Amphipathic Peptoid Mimics of Pulmonary Surfactant Proteins. *Scientific Reports*, 8(1):1–9, 2018.
- [84] K. R. Melton, L. L. Nessler, M. Ikegami, J. W. Tichelaar, J. C. Clark, J. A. Whitsett, and T. E. Weaver. SP-B Deficiency Causes Respiratory Failure in Adult Mice. *American Journal of Physiology-Lung Cellular and Molecular Physiology*, 285(3):L543–L549, 2003.
- [85] M. Sharifahmadian, M. Sarker, D. Palleboina, A. J. Waring, F. J. Walther, M. R. Morrow, and V. Booth. Role of the N-Terminal Seven Residues of Surfactant Protein B (SP-B). *Plos One*, 8(9):e72821, 2013.
- [86] R. S. Farver, F. D. Mills, V. C. Antharam, J. N. Chebukati, G. E. Fanucci, and J. R. Long. Lipid Polymorphism Induced by Surfactant Peptide SP-B1-25. *Biophysical Journal*, 99(6):1773–1782, 2010.
- [87] B. Russell-Schulz, V. Booth, and M. R. Morrow. Perturbation of DPPC/POPG Bilayers by the N-Terminal Helix of Lung Surfactant Protein SP-B: a ^2H NMR Study. *European Biophysics Journal*, 38(5):613–624, 2009.
- [88] V. C. Antharam, R. S. Farver, A. Kuznetsova, K. H. Sippel, F. D. Mills, D. W. Elliott, E. Sternin, and J. R. Long. Interactions of the C-Terminus of Lung Surfactant

- Protein B with Lipid Bilayers are Modulated by Acyl Chain Saturation. *Biochimica et Biophysica Acta (BBA)-Biomembranes*, 1778(11):2544–2554, 2008.
- [89] T.-C. Yang, M. McDonald, M. R. Morrow, and V. Booth. The Effect of a C-Terminal Peptide of Surfactant Protein B (SP-B) on Oriented Lipid Bilayers, Characterized by Solid-State ^2H - and ^3P -NMR. *Biophysical Journal*, 96(9):3762–3771, 2009.
- [90] A. S. Dico, J. Hancock, M. R. Morrow, J. Stewart, S. Harris, and K. M. W. Keough. Pulmonary Surfactant Protein SP-B Interacts Similarly with Dipalmitoylphosphatidylglycerol and Dipalmitoylphosphatidylcholine in Phosphatidylcholine/Phosphatidylglycerol Mixtures. *Biochemistry*, 36(14):4172–4177, 1997.
- [91] E. E. Burnell and C. A. De Lange. *NMR of Ordered Liquids*. Springer Science & Business Media, 2013.
- [92] J. H. Davis. The Description of Membrane Lipid Conformation, Order and Dynamics by ^2H -NMR. *Biochimica et Biophysica Acta (BBA)-Reviews on Biomembranes*, 737(1):117–171, 1983.
- [93] D. M. Brink and G. R. Satchler. *Theory of Angular Momentum*, 1968.
- [94] L. J. Burnett and B. H. Muller. Deuteron Quadrupole Coupling Constants in Three Solid Deuterated Paraffin Hydrocarbons: C₂D₆, C₄D₁₀, C₆D₁₄. *The Journal of Chemical Physics*, 55(12):5829–5831, 1971.
- [95] D. H. Jones, K. R. Barber, C. W. M. Grant, and R. S. Hodges. Pilin C-Terminal Peptide Binds Asialo-GM1 in Liposomes: A ^2H -NMR Study. *Protein Science*, 6(11):2459–2461, 1997.

- [96] M. Bloom, J. H. Davis, and A. L. Mackay. Direct Determination of the Oriented Sample NMR Spectrum from the Powder Spectrum for Systems with Local Axial Symmetry. *Chemical Physics Letters*, 80(1):198–202, 1981.
- [97] E. Sternin, M. Bloom, and A. L. Mackay. DePakeing of NMR spectra. *Journal of Magnetic Resonance (1969)*, 55(2):274–282, 1983.
- [98] M. A. McCabe and S. R. Wassail. Rapid Deconvolution of NMR Powder Spectra by Weighted Fast Fourier Transformation. *Solid State Nuclear Magnetic Resonance*, 10(1-2):53–61, 1997.
- [99] H. I. Petrache, S. W. Dodd, and M. F. Brown. Area Per Lipid and Acyl Length Distributions in Fluid Phosphatidylcholines Determined by ^2H NMR spectroscopy. *Biophysical Journal*, 79(6):3172–3192, 2000.
- [100] J. H. Davis, K. R. Jeffrey, M. Bloom, M. I. Valic, and T. P. Higgs. Quadrupolar Echo Deuteron Magnetic Resonance Spectroscopy in Ordered Hydrocarbon Chains. *Chemical Physics Letters*, 42(2):390–394, 1976.
- [101] N. O. Petersen, P. A. Kroon, M. Kainosho, and S. I. Chan. Thermal Phase Transitions in Deuterated Lecithin Bilayers. *Chemistry and Physics of Lipids*, 14(4):343–349, 1975.
- [102] J. H. Davis. Deuterium Magnetic Resonance Study of the Gel and Liquid Crystalline Phases of Dipalmitoyl Phosphatidylcholine. *Biophysical Journal*, 27(3):339–358, 1979.

- [103] M. B. Sankaram and T. E. Thompson. Deuterium Magnetic Resonance Study of Phase Equilibria and Membrane Thickness in Binary Phospholipid Mixed Bilayers. *Biochemistry*, 31(35):8258–8268, 1992.
- [104] M. Sarker, J. Rose, M. McDonald, M. R. Morrow, and V. Booth. Modifications to Surfactant Protein B Structure and Lipid Interactions Under Respiratory Distress Conditions: Consequences of Tryptophan Oxidation. *Biochemistry*, 50(1):25–36, 2011.
- [105] V. Booth, A. J. Waring, F. J. Walther, and K. M. W. Keough. NMR Structures of the C-Terminal Segment of Surfactant Protein B in Detergent Micelles and Hexafluoro-2-propanol. *Biochemistry*, 43(48):15187–15194, 2004.
- [106] M. R. Morrow, J. Perez-Gil, G. Simatos, C. Boland, J. Stewart, D. Absolom, V. Sarin, and K.M.W. Keough. Pulmonary Surfactant-Associated Protein SP-B has Little Effect on Acyl Chains in Dipalmitoylphosphatidylcholine Dispersions. *Biochemistry*, 32(16):4397–4402, 1993.
- [107] B. Leimkuhler and C. Matthews. *Molecular Dynamics*. Springer, 2016.
- [108] L. Verlet. Computer “Experiments” on Classical Fluids. I. Thermodynamical Properties of Lennard-Jones Molecules. *Physical Review*, 159(1):98, 1967.
- [109] L. Verlet. Computer “Experiments” on Classical Fluids. II. Equilibrium Correlation Functions. *Physical Review*, 165(1):201, 1968.
- [110] A. R. Leach. *Molecular Modelling: Principles and Applications*. Pearson Education, 2001.

- [111] K. P. Jensen and W. L. Jorgensen. Halide, Ammonium, and Alkali Metal Ion Parameters for Modeling Aqueous Solutions. *Journal of Chemical Theory and Computation*, 2(6):1499–1509, 2006.
- [112] W. L. Jorgensen and J. Tirado-Rives. The OPLS [Optimized Potentials for Liquid Simulations] Potential Functions for Proteins, Energy Minimizations for Crystals of Cyclic Peptides and Crambin. *Journal of the American Chemical Society*, 110(6):1657–1666, 1988.
- [113] E. Harder, W. Damm, J. Maple, C. Wu, M. Reboul, J. Y. Xiang, L. Wang, D. Lupyan, M. K. Dahlgren, J. L. Knight, J. W. Kaus, D. S. Cerutti, G. Krilov, W. L. Jorgensen, R. Abel, and R. A. Friesner. OPLS3: A Force Field Providing Broad Coverage of Drug-Like Small Molecules and Proteins. *Journal of Chemical Theory and Computation*, 12(1):281–296, 2016.
- [114] K. Lindorff-Larsen, S. Piana, K. Palmo, P. Maragakis, J. L. Klepeis, R. O. Dror, and D. E. Shaw. Improved Side-Chain Torsion Potentials for the Amber FF99SB Protein Force Field. *Proteins: Structure, Function, and Bioinformatics*, 78, 8, 1950-1958. 2010.
- [115] J. A. Maier, C. Martinez, K. Kasavajhala, L. Wickstrom, K. E. Hauser, and C. Simmerling. FF14SB: Improving the Accuracy of Protein Side Chain and Backbone Parameters from FF99SB. *Journal of Chemical Theory and Computation*, 11(8):3696–3713, 2015.
- [116] V. Hornak, R. Abel, A. Okur, B. Strockbine, A. Roitberg, and C. Simmerling. Comparison of Multiple Amber Force Fields and Development of Improved Pro-

- tein Backbone Parameters. *Proteins: Structure, Function, and Bioinformatics*, 65(3):712–725, 2006.
- [117] S. Piana, K. Lindorff-Larsen, and D. E. Shaw. How Robust are Protein Folding Simulations with Respect to Force Field Parameterization? *Biophysical Journal*, 100(9):L47–L49, 2011.
- [118] A. D. MacKerell Jr, D. Bashford, M. L. D. R. Bellott, R. L. Dunbrack Jr, J. D. Evanseck, M. J. Field, S. Fischer, J. Gao, H. Guo, S. Ha, D. Joseph-McCarthy, L. Kuchnir, K. Kuczera, F. T. Lau, C. Mattos, S. Michnick, T. Ngo, D. T. Nguyen, B. Prodhom, W. E. Reiher, B. Roux, M. Schlenkrich, J. C. Smith, R. Stote, J. Straub, M. Watanabe, J. Wiórkiewicz-Kuczera, D. Yin, and M. Karplus. All-Atom Empirical Potential for Molecular Modeling and Dynamics Studies of Proteins. *The Journal of Physical Chemistry B*, 102(18):3586–3616, 1998.
- [119] A. D. Mackerell Jr, M. Feig, and C. L. Brooks III. Extending the Treatment of Backbone Energetics in Protein Force Fields: Limitations of Gas-Phase Quantum Mechanics in Reproducing Protein Conformational Distributions in Molecular Dynamics Simulations. *Journal of Computational Chemistry*, 25(11):1400–1415, 2004.
- [120] J. B. Klauda, R. M. Venable, J. A. Freites, J. W. O’Connor, D. J. Tobias, C. Mondragon-Ramirez, I. Vorobyov, Alexander D. MacKerell Jr, and R. W. Pastor. Update of the CHARMM All-Atom Additive Force Field for Lipids: Validation on Six Lipid Types. *The Journal of Physical Chemistry B*, 114(23):7830–7843, 2010.

- [121] J. Huang and A. D. MacKerell Jr. CHARMM36 All-Atom Additive Protein Force Field: Validation Based on Comparison to NMR Data. *Journal of Computational Chemistry*, 34(25):2135–2145, 2013.
- [122] A. V. Onufriev and S. Izadi. Water Models for Biomolecular Simulations. *Wiley Interdisciplinary Reviews: Computational Molecular Science*, 8(2):e1347, 2018.
- [123] J. D. Bernal and R. H. Fowler. A Theory of Water and Ionic Solution, with Particular Reference to Hydrogen and Hydroxyl Ions. *The Journal of Chemical Physics*, 1(8):515–548, 1933.
- [124] W. L. Jorgensen, J. Chandrasekhar, J. D. Madura, R. W. Impey, and M. L. Klein. Comparison of Simple Potential Functions for Simulating Liquid Water. *The Journal of Chemical Physics*, 79(2):926–935, 1983.
- [125] F. Sajadi and C. N. Rowley. Simulations of Lipid Bilayers Using the CHARMM36 Force Field with the TIP3P-FB and TIP4P-FB Water Models. *PeerJ*, 6:e5472, 2018.
- [126] S. Nosé. A Molecular Dynamics Method for Simulations in the Canonical Ensemble. *Molecular Physics*, 52(2):255–268, 1984.
- [127] W. G. Hoover. Canonical Dynamics: Equilibrium Phase-Space Distributions. *Physical Review A*, 31(3):1695, 1985.
- [128] M. Parrinello and A. Rahman. Polymorphic Transitions in Single Crystals: A New Molecular Dynamics Method. *Journal of Applied Physics*, 52(12):7182–7190, 1981.

- [129] C. Kutzner, D. Van Der Spoel, M. Fechner, E. Lindahl, U. W. Schmitt, B. L. De Groot, and H. Grubmüller. Speeding Up Parallel GROMACS on High-Latency Networks. *Journal of Computational Chemistry*, 28(12):2075–2084, 2007.
- [130] H. J. C. Berendsen, B. Hess, E. Lindahl, D. Van Der Spoel, A. E. Mark, and G. Groenhof. GROMACS: Fast, Flexible, and Free. *J. Comput. Chem*, 26(16):1701–1718, 2005.
- [131] J. B. Klauda, R. M. Venable, A. D. MacKerell Jr, and R. W. Pastor. Considerations for Lipid Force Field Development. *Current Topics in Membranes*, 60:1–48, 2008.
- [132] R. W. Pastor and A. D. MacKerell Jr. Development of the CHARMM Force Field for Lipids. *The Journal of Physical Chemistry Letters*, 2(13):1526–1532, 2011.
- [133] N. Guex and M. C. Peitsch. SWISS-MODEL and the Swiss-Pdb Viewer: An Environment for Comparative Protein Modeling. *Electrophoresis*, 18(15):2714–2723, 1997.
- [134] Protein Data Bank: The Single Global Archive for 3D Macromolecular Structure Data. *Nucleic Acids Research*, 47(D1):D520–D528, 2019.
- [135] S. Jo, T. Kim, V. G. Iyer, and W. Im. CHARMM-GUI: A Web-Based Graphical User Interface for CHARMM. *Journal of Computational Chemistry*, 29(11):1859–1865, 2008.
- [136] S. Baldwin. Compute Canada: Advancing Computational Research. In *Journal of Physics: Conference Series*, volume 341, page 012001. IOP Publishing, 2012.

- [137] M. Carr and C. E. MacPhee. Membrainy: A ‘Smart’, Unified Membrane Analysis Tool. *Source Code for Biology and Medicine*, 10(1):1–10, 2015.
- [138] [<http://plasma gate.weizmann.ac.il/Grace/>]. Grace 2D Plotting Tool.
- [139] D. Frishman and P. Argos. Knowledge-Based Protein Secondary Structure Assignment. *Proteins: Structure, Function, and Bioinformatics*, 23(4):566–579, 1995.
- [140] N. Colloc’h, C. Etchebest, E. Thoreau, B. Henrissat, and J.-P. Mornon. Comparison of Three Algorithms for the Assignment of Secondary Structure in Proteins: The Advantages of a Consensus Assignment. *Protein Engineering, Design and Selection*, 6(4):377–382, 1993.
- [141] E. N. Baker and R. E. Hubbard. Hydrogen Bonding in Globular Proteins. *Progress in Biophysics and Molecular Biology*, 44(2):97–179, 1984.
- [142] W. Kabsch and C. Sander. Dictionary of Protein Secondary Structure: Pattern Recognition of Hydrogen-Bonded and Geometrical Features. *Biopolymers: Original Research on Biomolecules*, 22(12):2577–2637, 1983.
- [143] W. Humphrey, A. Dalke, and K. Schulten. VMD: Visual Molecular Dynamics. *Journal of Molecular Graphics*, 14(1):33–38, 1996.
- [144] J. S. Richardson. The Anatomy and Taxonomy of Protein Structure. *Advances in Protein Chemistry*, 34:167–339, 1981.
- [145] M. H. Khatami, I. Saika-Voivod, and V. Booth. All-Atom Molecular Dynamics Simulations of Lung Surfactant Protein B: Structural Features of SP-B Pro-

- mote Lipid Reorganization. *Biochimica et Biophysica Acta (BBA)-Biomembranes*, 1858(12):3082–3092, 2016.
- [146] J. Pérez-Gil. Lipid-Protein Interactions of Hydrophobic Proteins SP-B and SP-C in Lung Surfactant Assembly and Dynamics. *Pediatric Pathology & Molecular Medicine*, 20(6):445–469, 2001.
- [147] G. K. Suresh and R. F. Soll. Overview of Surfactant Replacement Trials. *Journal of Perinatology*, 25(2):S40–S44, 2005.
- [148] P. R. Chess, J. N. Finkelstein, and B. A. Holm. Surfactant Replacement Therapy in Lung Injury. In *Lung Injury*, pages 645–692. CRC Press, 2005.
- [149] World Health Organization (2020). Coronavirus Disease 2019 (COVID-19): Situation Report 46. World Health Organization. <https://apps.who.int/iris/handle/10665/331443>.
- [150] F. Wu, S. Zhao, B. Yu, Y.-M. Chen, W. Wang, Z.-G. Song, Y. Hu, Z.-W. Tao, J.-H. Tian, Y.-Y. Pei, M. L. Yuan, Y.-L. Zhang, F.-H. Dai, Y. Liu, Q.-M. Wang, J.-J. Zheng, L. Xu, E. C. Holmes, and Y.-Z. Zhang. A New Coronavirus Associated with Human Respiratory Disease in China. *Nature*, 579(7798):265–269, 2020.
- [151] P. Zhou, X.-L. Yang, X.-G. Wang, B. Hu, L. Zhang, W. Zhang, H.-R. Si, Y. Zhu, B. Li, C.-L. Huang, H.-D. Chen, J. Chen, Y. Luo, H. Guo, R.-D. Jiang, M.-Q. Liu, Y. Chen, X.-R. Shen, X. Wang, X.-S. Zheng, K. Zhao, Q.-J. Chen, F. Deng, L.-L. Liu, B. Yan, F.-X. Zhan, Y.-Y. Wang, G.-F. Xiao, and Z.-L. Shi. A Pneumonia Outbreak Associated with a New Coronavirus of Probable Bat Origin. *Nature*, 579(7798):270–273, 2020.

- [152] W.-j. Guan, Z.-y. Ni, Y. Hu, W.-h. Liang, C.-q. Ou, J.-x. He, L. Liu, H. Shan, C.-l. Lei, D. S. C. Hui, B. Du, L.-j. Li, G. Zeng, K.-Y. Yuen, R.-c. Chen, C.-l. Tang, T. Wang, P.-y. Chen, J. Xiang, S.-y. Li, J.-l. Wang, Z.-j. Liang, Y.-x. Peng, L. Wei, Y. Liu, Y.-h. Hu, P. Peng, J.-m. Wang, J.-y. Liu, Z. Chen, G. Li, Z.-j. Zheng, S.-q. Qiu, J. Luo, C.-j. Ye, S.-y. Zhu, and N.-s. Zhong. Clinical Characteristics of Coronavirus Disease 2019 in China. *New England Journal of Medicine*, 382(18):1708–1720, 2020.
- [153] S. Piva, R. M. DiBlasi, A. E. Slee, A. H. Jobe, A. M. Roccaro, M. Filippini, N. Latronico, M. Bertoni, J. C. Marshall, and M. A. Portman. Surfactant Therapy for COVID-19 Related ARDS: a Retrospective Case-Control Pilot Study. *Respiratory Research*, 22(1):1–8, 2021.
- [154] M. Heching, S. Lev, D. Shitenberg, D. Dicker, and M. R. Kramer. Surfactant for the Treatment of ARDS in a Patient With COVID-19. *Chest*, 2021.
- [155] R. A. W. Veldhuizen, Y. Y. Zuo, N. O. Petersen, J. F. Lewis, and F. Possmayer. The COVID-19 Pandemic: A Target for Surfactant Therapy? *Expert Review of Respiratory Medicine*, 15(5):597–608, 2021.
- [156] C. G. Cochrane and S. D. Revak. Pulmonary Surfactant Protein B (SP-B): Structure-Function Relationships. *Science*, 254(5031):566–568, 1991.
- [157] J. Perez-Gil and T. E. Weaver. Pulmonary Surfactant Pathophysiology: Current Models and Open Questions. *Physiology*, 25(3):132–141, 2010.

- [158] D. Palleboina, A. J. Waring, R. H. Notter, V. Booth, and M. Morrow. Effects of the Lung Surfactant Protein B Construct Mini-B on Lipid Bilayer Order and Topography. *European Biophysics Journal*, 41(9):755–767, 2012.
- [159] C. Faulkner, D. Santos-Carballal, D. F. Plant, and N. H. de Leeuw. Atomistic Molecular Dynamics Simulations of Propofol and Fentanyl in Phosphatidylcholine Lipid Bilayers. *ACS omega*, 5(24):14340–14353, 2020.
- [160] S. Erimban and S. Daschakraborty. Compatibility of Advanced Water Models with a United Atom Model of Lipid in Lipid Bilayer Simulation. *The Journal of Chemical Physics*, 151(6):065104, 2019.
- [161] C. T. Boughter, V. Monje-Galvan, W. Im, and J. B. Klauda. Influence of Cholesterol on Phospholipid Bilayer Structure and Dynamics. *The Journal of Physical Chemistry B*, 120(45):11761–11772, 2016.
- [162] I. Marzuoli, C. Margreitter, and F. Fraternali. Lipid Head Group Parameterization for GROMOS 54A8: A Consistent Approach with Protein Force Field Description. *Journal of Chemical Theory and Computation*, 15(10):5175–5193, 2019.

Appendix A

System Setup

A.1 Making a PDB File From the Amino Acid Sequence of the Peptide.

To make a PDB file from the Amino acid sequence of the peptide, make a text document using the text editor and enter the following:

```
> Peptide
```

FPIPLPYCW and saved this file as txt file. Here FPIPLPYCW is the amino acid sequence of the peptide. Open this txt file using Swiss PDB viewer and save it as a pdb file. Now we have the PDB file of the peptide.

I followed the steps in [GROMACS Tutorial](#) for much of the computational part. The tutorial can be found here: <http://www.mdtutorials.com/gmx/> . Refer to [GROMACS Commands](#) to see how to execute them.

To generate the topology from the PDB file executed [pdb2gmx](#).

-ignh flag ignores the H atoms in the PDB file.

-ter flag assigns charge states to both N and C termini

In this step select the desired force field and water model. Here we can also select the termination of the peptide.

For adjusting the peptide orientation, use [gmx editconf](#)

If the system contains multiple peptides, make sure to label each of them differently. This can be done by editing the PDB file.

A.1.1 Building Membrane-Lipid Bilayer System Using CHARMM GUI Membrane Builder

Opened the [CHARMM GUI membrane builder](#). I used the membrane with a protein option. Imported the pdb file with properly oriented peptide (need to convert the gro file to pdb file as CHARMM GUI only take pdb file as input file).

In the orientation option, I used PDB orientation and Translate molecule along the Z-axis option for positioning option. I had to translate -32 angstroms to align the peptides on the leaflets. In the System size determination option, I chose Heterogeneous lipids,

Rectangular box type, Length of Z based on water thickness, Length of XY based on Ratio of lipid components. Chose length of X and Y initial guess as 128

DPPC 7:7 and POPG 3:3 (Ratio- upper leaflet to lower leaflet)

I chose the Replacement method in the system building option, Include ions (add neutralizing ions) in the component building option, and chose Distance in the Ion replacement method.

I used the charmm36 force field.

Input generation option: Gromacs

Equilibration options: Generate grid information for PME FFT automatically. NPT ensemble. Temperature: 310.15K

A.1.2 Energy Minimization, Energy Equilibration and Production

Run

For energy minimization and equilibration steps, we need to use the commands `gmx grompp` and `gmx mdrun`.

The necessary files needed for these steps can be found in the output folder from CHARMM GUI.

The 'topol.top' file contains the information of the system such as force field and components. An example is shown below:

```
;;  
;; Generated by CHARMM-GUI FF-Converter  
;;  
;; Correspondance:  
;; jul316@lehigh.edu or wonpil@lehigh.edu  
;;  
;; The main GROMACS topology file  
;;  
  
; Include forcefield parameters  
#include "toppar/forcefield.itp"  
#include "toppar/PROA.itp"
```

```
#include "toppar/POPG.itp"
#include "toppar/DPPC.itp"
#include "toppar/POT.itp"
#include "toppar/TIP3.itp"
```

```
[ system ]
```

```
; Name
```

```
Title
```

```
[ molecules ]
```

```
; Compound      #mols
PROA              36
POPG              348
DPPC              812
POT               348
TIP3              54519
```

An example of the .mdp file used for the production run after the energy minimization and equilibration steps is shown below:

```
integrator        = md
dt                = 0.002
nsteps            = 5000000000
nstxout           = 500000
nstvout           = 0
```

```

nsthout          = 0
nstcalcenergy    = 1000
nstenergy        = 1000
nstlog           = 1000
nstxout-compressed = 50000
compressed-x-precision = 10000
compressed-x-grps = Protein POPG DPPC
energygrps       = Protein POPG DPPC POT TIP3
;
cutoff-scheme    = Verlet
nstlist          = 20
rlist            = 1.2
coulombtype      = pme
rcoulomb         = 1.2
vdwtype          = Cut-off
vdw-modifier     = Force-switch
rvdw_switch      = 1.0
rvdw             = 1.2
;
tcoupl           = Nose-Hoover
tc_grps          = SYSTEM
tau_t            = 1.0
ref_t            = 323
;

```

```

pcoupl          = Parrinello-Rahman
pcoupltype      = semiisotropic
tau_p          = 5.0
compressibility = 4.5e-5 4.5e-5
ref_p          = 1.0 1.0
;
constraints     = h-bonds
constraint_algorithm = LINCS
continuation    = yes
;
nstcomm        = 100
comm_mode      = linear
comm_grps     = SYSTEM
;
refcoord_scaling = com

```

A.1.3 Running in the Cluster

We ran our production runs in the Compute Canada [Graham](#) HPC cluster. The information about [job scheduling](#) can be found in [Compute Canada documentation](#). An example of the job script file (.sh) we used for production run is shown below.

```

#!/bin/bash

#SBATCH --nodes=1           # number of nodes
#SBATCH --gres=gpu:2       # request 2 GPUs per node (Graham)

```

```
#SBATCH --ntasks-per-node=4      # request 4 MPI tasks per node
#SBATCH --cpus-per-task=8        # 8 OpenMP threads per MPI process
#SBATCH --mem-per-cpu=1024M
#SBATCH --time=0-24:00           # time limit (D-HH:MM)
#SBATCH --mail-user=giveyouremailid@mun.ca
#SBATCH --mail-type=BEGIN
#SBATCH --mail-type=END
#SBATCH --mail-type=FAIL

module purge

module load gcc/7.3.0  cuda/10.0.130  openmpi/3.1.2  gromacs/2020.2

export OMP_NUM_THREADS="${SLURM_CPUS_PER_TASK:-1}"

# Production run using GPU

mpirun -x gmx_mpi mdrun -v -deffnm step7_1 -maxh 23.5 -cpt 60
```

Appendix B

Trajectory Analysis

B.1 Energy-Time Series

Energy-time series can be obtained using [gmx energy](#) command. Need to supply the .edr file from the production run. The output file can be opened using [Grace software](#).

Example:

```
gmx energy -f step_7_1.edr -o energy.xvg
```

B.2 Order Parameter Profiles

The order parameter profiles were calculated using [Membrainy software](#) as [gmx order](#) has some issues in calculating the order parameters of saturated lipids. First need to make a .gro file using .trr and .tpr files from the production run. I used [gmx trjconv](#) for this conversion. An example of calling these commands is given below:

```
gmx trjconv -f step7_1.trr -s step7_1.tpr -pbc mol -b 1000 -e 450000  
-o 1-450ns.gro
```

For obtaining order parameter using membrainy:

```
java -jar Membrainy.jar -f 1-450ns.gro -s 1-450ns.gro -order
```

B.3 Helicity Calculation

For calculating the secondary structure of a peptide, we need to make a .gro file of that peptide and load it in [VMD software](#). Then **Extensions** → **Analysis** → **Timeline** → **Calculate** → **Cal.Sec.Struct** The structure codes can be found in the **Help** tab in the same window. If the system has multiple peptides we can load the .gro files of each.

For isolating each peptide, we need to make the index files of each peptide. The command [gmx make_ndx](#) can be used for making the index files. Note: There's another way of automating this using VMD scripting. I haven't explored it very much.

Calculating the Helicity percentage from the secondary structure file over the time range analysed can get tedious. An example of the python script I used for calculating helicity percentage at a single time frame for two peptides is given below. Might be helpful in the calculation of helicity percentage over multiple time frames.

```
T1=0
```

```
T2=338
```

```
import pandas as pd
```

```
import numpy as np
```

```

import matplotlib.pyplot as plt

import itertools

from itertools import count

pd.set_option('mode.chained_assignment', None)

pd.set_option('chained_assignment', None)

data = pd.read_csv("secondary.txt", header = None)

headerName=["Sec_structure"]

headerName=["Sec_structure"]

data.columns=headerName

A=data[9:]

A['Residue_Number']=A['Sec_structure'].str.split().str[-5]

A['Time_frame']=A['Sec_structure'].str.split().str[-2]

A['Secondary_structure']=A['Sec_structure'].str.split().str[-1]

A['Peptide_label']=A['Sec_structure'].str.split().str[-4]

B= A.drop(columns='Sec_structure')

Aa = B[B['Peptide_label'] == 'A' ].reset_index()

Aa1=Aa.drop(columns='index')

Bb = B[B['Peptide_label'] == 'B' ].reset_index()

Bb1=Bb.drop(columns='index')

```

```
# Processing PROA
```

```
Aa1.loc[Aa1['Secondary_structure'] == 'C', 'value'] = '0'  
Aa1.loc[Aa1['Secondary_structure'] == 'T', 'value'] = '0'  
Aa1.loc[Aa1['Secondary_structure'] == 'G', 'value'] = '1'  
Aa1.loc[Aa1['Secondary_structure'] == 'H', 'value'] = '1'
```

```
#Processing of PROB
```

```
Bb1.loc[Bb1['Secondary_structure'] == 'C', 'value'] = '0'  
Bb1.loc[Bb1['Secondary_structure'] == 'T', 'value'] = '0'  
Bb1.loc[Bb1['Secondary_structure'] == 'G', 'value'] = '1'  
Bb1.loc[Bb1['Secondary_structure'] == 'H', 'value'] = '1'
```

```
#PROA
```

```
resnm = 10
```

```
rdata=[]
```

```
for i in itertools.count(1,1):
```

```
    if i == resnm:
```

```
        break
```

```
    Reel = Aa1[Aa1['Residue_Number'] == str(i)].iloc[T1:T2].reset_index()['value']
```

```
    rdata.append((i, Reel))
```

```
proa=pd.DataFrame(rdata, columns=('resnm', 'val'))
```

```
#PROB
```

```
resnm1 = 10
```

```
rdata1=[]
```

```
for i in itertools.count(1,1):
```

```
    if i == resnm:
```

```
        break
```

```
    Ree2 = Bb1[Bb1['Residue_Number'] == str(i)].iloc[T1:T2].reset_index()['value']
```

```
    rdata1.append((i, Ree2))
```

```
prob=pd.DataFrame(rdata1, columns=('resnm', 'val'))
```

```
prob
```

```
#Plotting
```

```
plt.figure(figsize=(12,8))
```

```
x1=proa['resnm']
```

```
y1=proa['val']
```

```
x2=prob['resnm']
```

```
y2=prob['val']
```

```
plt.plot(x1,y1,color='red')
```

```
plt.plot(x2,y2,color='green')
```

```
plt.title('Helicity of Peptides')
```

```
plt.xlabel('Time(ns)')
```

```
plt.ylabel('Helicity Percentage')
```

```
plt.legend(['PROA', 'PROB'])
```

```
plt.savefig('helicity.png')
```

B.4 Density Profile

The Gromacs module `gmx density` can calculate the density. An example of executing the command is shown below:

```
gmx density -s step7_1.tpr -f step7_1.trr -n proa_density.ndx  
-b 75000 -e 450000 -o density_proa.xvg -d Z
```

where `proa_density.ndx` is the index file of the peptide.

B.5 Depth Profile

For calculating orientation of the peptide in the bilayer, we used a double Gaussian function on the density profile curves of each peptide and obtained the peaks. An example of calculation for one residue is shown below (got the double gaussian part from Stack Overflow):

```
import numpy as np  
import pandas as pd  
import itertools  
from itertools import count  
from pylab import *  
from scipy.optimize import curve_fit  
pd.set_option('mode.chained_assignment', None)
```

```

pd.set_option('chained_assignment',None)

data1 = pd.read_csv('phe_allframes.csv')
headerName=["z"]
data1.columns=headerName

a=data1['z']

#phe plot
data=a
y,x,_=hist(data,50,alpha=.3,label='data')

x=(x[1:]+x[:-1])/2 # for len(x)==len(y)

def gauss(x,mu,sigma,A):
    return A*exp(-(x-mu)**2/2/sigma**2)

def bimodal(x,mu1,sigma1,A1,mu2,sigma2,A2):
    return gauss(x,mu1,sigma1,A1)+gauss(x,mu2,sigma2,A2)

expected=(2.8,.2,2000,4.9,.2,2000)
params,cov=curve_fit(bimodal,x,y,expected)
sigma=sqrt(diag(cov))
plot(x,bimodal(x,*params),color='red',lw=3,label='model')
legend()

```

```

print(params, '\n', sigma)

params_b=pd.DataFrame(data={'params':params, 'sigma':sigma},
index=bimodal.__code__.co_varnames[1:])

params_b

```

B.6 Shortest Distance Calculation

For calculating the shortest distance of each residue of each peptide from the phosphorus atoms, we can use `gmx rdf`. We need to make the index files of each peptide with the index of phosphorus atoms in it. The following bash script is for calculating the rdf over the time range passed for one peptide.

```

>rdf_a.txt

for ((i=75000;i<450000;i+=100))
do
a=$((i))
b=$((i+1))
gmx rdf -f step7_1.xtc -s step7_1.tpr -o proa_rdf.xvg -b $a -e $b ...
-ref c_alpha -sel P -n proa_c_alpha_lipid.ndx

awk '{if (NR>25&& $2>0){print $1;exit}}' proa_rdf.xvg >> rdf_a.txt

rm proa_rdf.xvg

done

```